DYNAMICS OF THE THERMOSPHERE OVER MAWSON, ANTARCTICA

by

P. Wardill B.Sc(Hons.)

A thesis presented for the degree of

DOCTOR OF PHILOSOPHY

in the

UNIVERSITY OF ADELAIDE

(Mawson Institute for Antarctic Research)

March 1988

Contents

ABSTRACT

A scanning Fabry-Perot spectrometer at Mawson, Antarctica (invariant latitude: 70°S) was used to measure Doppler shift and broadening of the OI λ630nm emission in the night airglow and aurora. Analysis of these measurements yielded estimates of neutral thermospheric temperatures and wind velocities in the altitude range 200-300km. Measurements were obtained over 60 nights during the austral winter and equinoxes of 1983.

The diurnal behaviour of the observed wind velocity was found to follow the pattern of ion convection within the polar thermosphere, thus confirming the view that ion drag is the principal source of momentum for the neutral thermosphere at high geomagnetic latitudes. The wind speed and temperature were both observed to increase during geomagnetically disturbed conditions.

Further examination of the wind data revealed a strong dependence on the Y-component of the interplanetary magnetic field as measured by the IMP-8 spacecraft. This dependence was consistent with changes in the relative sizes of the dawn and dusk ion convection cells. A comparison of the observed winds with the predictions of a thermospheric general circulation model yielded good agreement in wind direction although the model wind speeds were generally larger than those observed.

Observations on several nights were devoted to the study of the vertical component of the wind velocity. This showed a large, rapid and complex response to energy input associated with auroral

substorms. Upward motions of ~100ms^{-1} were observed during periods of large geomagnetic disturbance. Oscillatory motions of amplitude >20ms^{-1} were observed during both quiet and disturbed conditions and were consistent with the presence of thermospheric gravity waves.

The presence of large divergences in the horizontal wind field was noted and was tentatively ascribed to the dissipation of thermospheric gravity waves generated in the vicinity of the auroral electrojet.

DECLARATION

To the best of the author's knowledge, this thesis contains no material previously published or written by another person except where due reference is made in the text. It contains no material which has been submitted or accepted for the award of any other degree or diploma in any university.

P. Wardill

ACKNOWLEDGEMENTS

The work described in this thesis was carried out using the equipment and facilities of the Mawson Institute for Antarctic Research, University of Adelaide. I wish to thank Dr F. Jacka, Director of the Mawson Institute, for supervising the project and for providing guidance and encouragement throughout.

I am indebted to Mr Don Creighton of the Mawson Institute, whose intensive training equipped me with the knowledge to tackle the inevitable electronic problems that arose during the course of a year's work in the Antarctic.

I also extend my thanks to all the staff and students of the Mawson Institute for their encouragement and support. Special thanks go to Norman Jones who collaborated in the development of the data analysis software and provided valuable comments and input at all stages of the project.

I gratefully acknowledge the logistical support and hospitality extended by the Antarctic Division and wish to thank all of the Mawson 1983 wintering party for sharing a unique and unforgettable experience.

Sincere thanks go to the following individuals and organisations for providing supplementary data used in the interpretation of my results:

- Dr G. Burns, Antarctic Division, for providing all-sky camera records from Mawson.
- The Director, Bureau of Mineral Resources, for providing magnetograms from Mawson.

- The Director, World Data Centre-A for Rockets and Satellites, Goddard Space Flight Centre, for providing interplanetary magnetic field data.

- Dr D. Rees, University College, London, for providing output from a thermospheric general circulation model.

Finally, I thank my wife Susan, for her patience and understanding.

Chapter 1

INTRODUCTION

The thermosphere is that region of the atmosphere above approximately 100km altitude, within which the temperature increases as a function of height. The structure and dynamics of the thermosphere are of great interest since the region is coupled to, and is influenced by, many other components of the sun-earth system. In particular, the thermosphere is directly coupled to the solar wind at high geomagnetic latitudes. The coupling occurs via momentum transfer from ions convected by the high-latitude electric field which is in turn produced by the interaction of the solar wind and the geomagnetic field. In addition, solar wind particles may directly enter the thermosphere to produce heating, ionisation and auroral displays at high latitudes. The consequences of these high-latitude processes are often global in their extent.

The aims of this thesis are :

(i) to identify the principle mechanisms responsible for driving the thermospheric circulation at high latitudes.

(ii) to identify the mechanisms responsible for perturbations to the basic circulation.

The thesis presents the results of observations of the thermospheric temperature and wind velocity made from within the southern auroral zone. Observations were carried out at the Australian National Antarctic Research Expedition's station at Mawson (67.6^{o}S, 62.9^{o}E) over 60 nights during the austral winter and equinoxes of

1983. Thermospheric temperature and wind velocity were inferred from measurements of the Doppler shift and broadening of the OI λ630nm emission, produced in the airglow and aurora, within the altitude range 200-300km. The measurements were made using a separation-scanned Fabry-Perot spectrometer, designed and constructed at the Mawson Institute for Antarctic Research.

The structure of the thesis is as follows: Chapter 2 provides a theoretical background to the work and presents a review of the relevant literature. The structure of the thermosphere is discussed and is related to the incident photon and particle fluxes. The ionosphere and magnetosphere are then introduced and their relationship to the neutral thermosphere is explored. Finally, the dynamics of the thermosphere are discussed in the light of recent observations. Particular emphasis is placed on the high-latitude thermosphere and the role of high-latitude electric fields.

Chapter 3 deals with the remote sensing of thermospheric properties via optical techniques. Emphasis is placed upon high spectral resolution studies of the λ630nm emission of atomic oxygen. The difficulties of applying these techniques during daytime are discussed.

In Chapter 4 the theory of the single etalon Fabry-Perot spectrometer is presented. The instrument used in this study is described in detail in Chapter 5 and the data analysis technique in Chapter 6.

The results of the project are presented in Chapter 7. The diurnal variations of thermospheric wind velocity and temperature, as observed from Mawson, are discussed and the observed wind is related to the ion-drag mechanism of momentum transfer. This mechanism is identified

as the primary momentum source for the high-latitude thermosphere. The variations of wind velocity and temperature are investigated as functions of magnetic local time and of geomagnetic activity.

A subsequent section is devoted to the influence of the y-component of the interplanetary magnetic field upon thermospheric circulation. This component affects the geometry of the high-latitude electric field and is found to have a significant influence upon circulation. The results are compared with the predictions of a thermospheric circulation model and found to agree qualitatively.

A further two sections present the results of measurements of the vertical component of the wind velocity and its possible relationship to large observed gradients in the horizontal components. The conclusions of the project are summarised in Chapter 8.

Chapter 2

STRUCTURE AND DYNAMICS OF THE THERMOSPHERE

2.1 Introduction

This chapter traces the development of our current understanding of thermospheric dynamics. Section 2.2 describes the effects of solar radiation on the earth's upper atmosphere and introduces the energy and momentum sources which drive the thermospheric circulation. This section also describes the ionosphere and magnetosphere, to which the thermosphere is coupled via the mechanism of ion drag. In section 2.3 the field of thermospheric dynamics is reviewed from the early 1970s to the present. The importance of high-latitude processes is emphasised and the study of the high-latitude thermosphere is treated separately. Finally, in section 2.4, a summary is given and the future direction of thermospheric research is discussed.

2.2 Solar Radiation and the Earth's Upper Atmosphere

2.2.1 Photon and Particle Radiation

The sun emits electromagnetic radiation over a broad spectral range extending from gamma rays to radio waves. Radiation is transmitted by the earth's atmosphere within the visible region of the spectrum (~400-800nm) and parts of the radio region. Radiation at other wavelengths is absorbed within the atmosphere and serves as the primary energy source for most atmospheric processes.

Within the visible region the solar spectrum resembles that of a black body at a temperature of ~6000K. The greater part of the energy is emitted in the range 200-1200nm and originates within the photosphere (the visible solar disc). The energy flux within this range, measured in the vicinity of the earth's orbit, is $\sim 1.2 \times 10^{3}$ W.m^{-2} (Ratcliffe 1972). At wavelengths below 100nm (the X-ray and ultraviolet range) radiation is emitted principally by the corona and chromosphere at temperatures of the order of 10^{6}K. The flux within this range is $\sim 3 \times 10^{-3}$ W.m^{-2} (Hinteregger 1970,1976) and is almost totally absorbed within the thermosphere. The X-ray and ultraviolet (XUV) flux varies with the 11-year cycle of solar activity and on shorter time scales, causing corresponding variation of upper atmospheric properties.

The sun also emits energy in the form of charged particles which constitute a highly conducting plasma known as the solar wind. This plasma originates within the solar corona which is composed chiefly of protons and electrons. The coronal temperature as a function of radial distance r, decreases less rapidly than 1/r causing the coronal plasma to be accelerated outward at velocities of the order of 10^{6} ms^{-1}. The interaction of the solar wind with the earth's magnetic field leads to distortion and confinement of the field as discussed in section 2.2.4.

The energy flux of the solar wind, measured at the earth's orbit is $\sim 10^{-4}$W.m^{-2} (Ratcliffe 1972). Solar wind particles and energy are deposited in the earth's atmosphere at high latitudes via a complicated mechanism to be discussed further in section 2.2.4. The effects of this high-latitude energy source are often detected globally.

The solar wind is subject to sudden enhancements in particle flux and energy which are associated with other solar disturbances and whose frequency of occurrence follows the 11-year solar activity cycle.

2.2.2 Thermal Structure and Composition of the Thermosphere.

The concentrations of various atmospheric gases as functions of height are shown in Figure 2.1 for conditions of moderate solar activity (CIRA 1965). At heights greater than ~100km the atmospheric constituents are in diffusive equilibrium and are distributed with different scale heights. In the region ~200-700km the main constituent is atomic oxygen, resulting from the photodissociation of O_2 by radiation in the Schumann-Runge continuum (135-175nm). The molecular species O_2 and N_2 are present in significant quantities below ~500km with concentrations falling off rapidly with increasing altitude as a result of their relatively large masses. Molecular nitrogen has no important dissociation continuum in the ultraviolet and hence atomic nitrogen is not present in significant quantities.

At heights in excess of ~1000km, atomic hydrogen and helium are the major constituents. At these heights the gas density is so low that the neutral particles follow ballistic trajectories and may escape from the earth's gravitational field providing their vertical component of velocity exceeds the escape velocity (~11km.s^{-1}). The rms velocities of hydrogen and helium for typical thermospheric temperatures are a few kilometers per second and significant numbers of particles may therefore escape. The region of the atmosphere where escape occurs is called the exosphere; its lower boundary (the exobase) may be taken to be that height at which the gas mean free path equals one scale height.

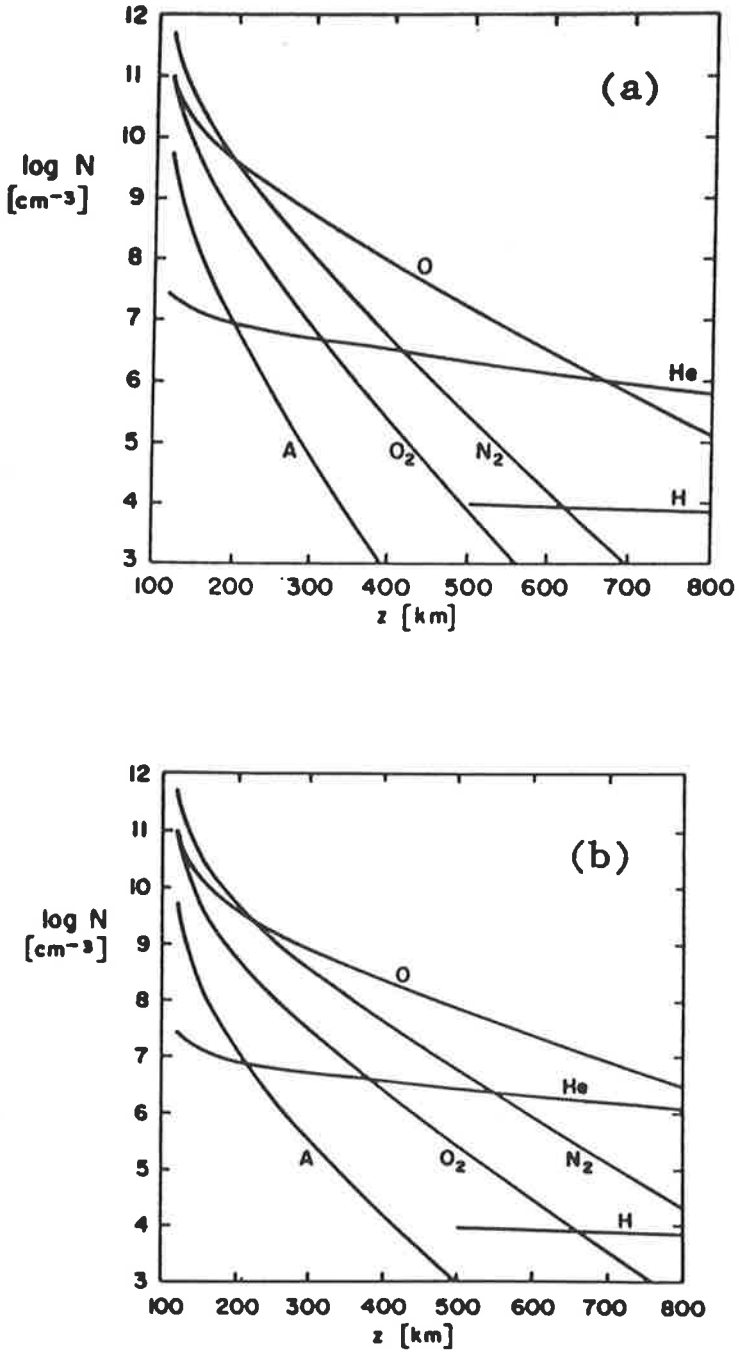

Figure 2.1 (a) Number densities of the principal neutral species as functions of height for moderate solar activity at 0400 local time (CIRA 1965).
(b) as above but for 1400 local time.

Figure 2.2 shows the atmospheric temperature as a function of height. Energy in the XUV region of the spectrum is absorbed above 100km and causes photoionisation of O_2 (λ<103nm), of O (λ<91nm), of N (λ<85nm) and of N_2 (λ<80nm). This energy heats the thermosphere and maintains the thermospheric temperature gradient down which heat is conducted to lower levels. The thermospheric temperature becomes independent of height above ~300km; the asymptotic value is the exospheric temperature. The thermospheric temperature gradient and exospheric temperature undergo considerable variation as the XUV flux changes with solar activity.

2.2.3 The Ionosphere

Photoionisation of atmospheric gases by XUV radiation causes the formation of a tenuous yet important plasma in the upper atmosphere. The region where ionisation is significant is called the ionosphere and is illustrated in Figure 2.3 which shows the electron number density as a function of height and illustrates the ionospheric regions, designated D,E and F.

The *production* of electrons maximises at ~110km and a local maximum in electron concentration (the E-layer) is always observed near this height during the day. Above the E-layer the electron concentration increases to its maximum value of $\sim 10^{12} m^{-3}$ at ~250km (the F2 peak). A small peak or point of inflection (the F1 layer or ledge) is often observed between the E-layer and the F2 peak when the solar zenith angle is small.

Chapman (1931), in a classic paper, has considered the effect of monochromatic ionising radiation incident on a horizontally stratified atmosphere with constant scale height. Under these conditions the production of electrons as a function of height follows a fairly

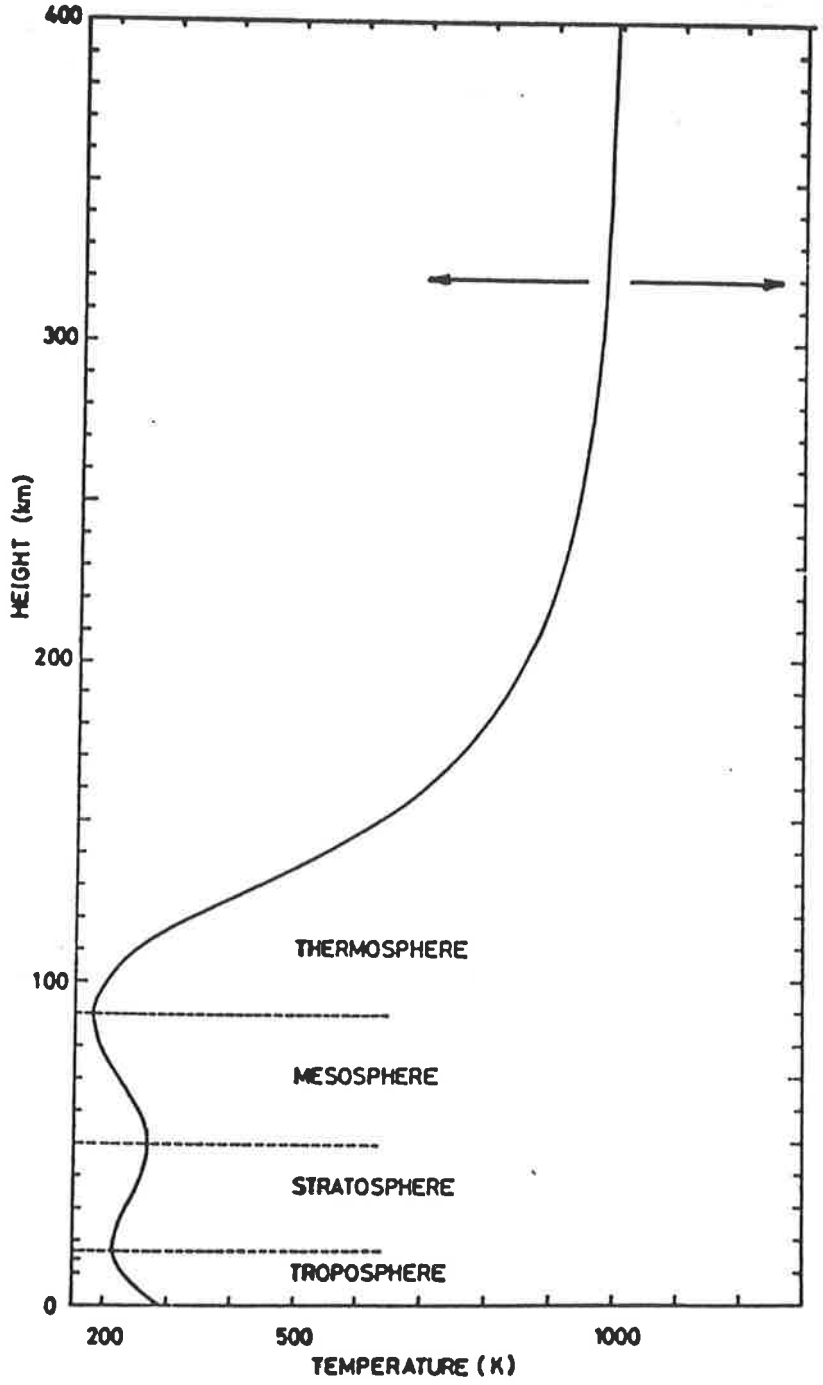

Figure 2.2 Atmospheric temperature as a function of height (CIRA 1972). The exospheric temperature may vary by several hundred degrees as indicated by the arrows.

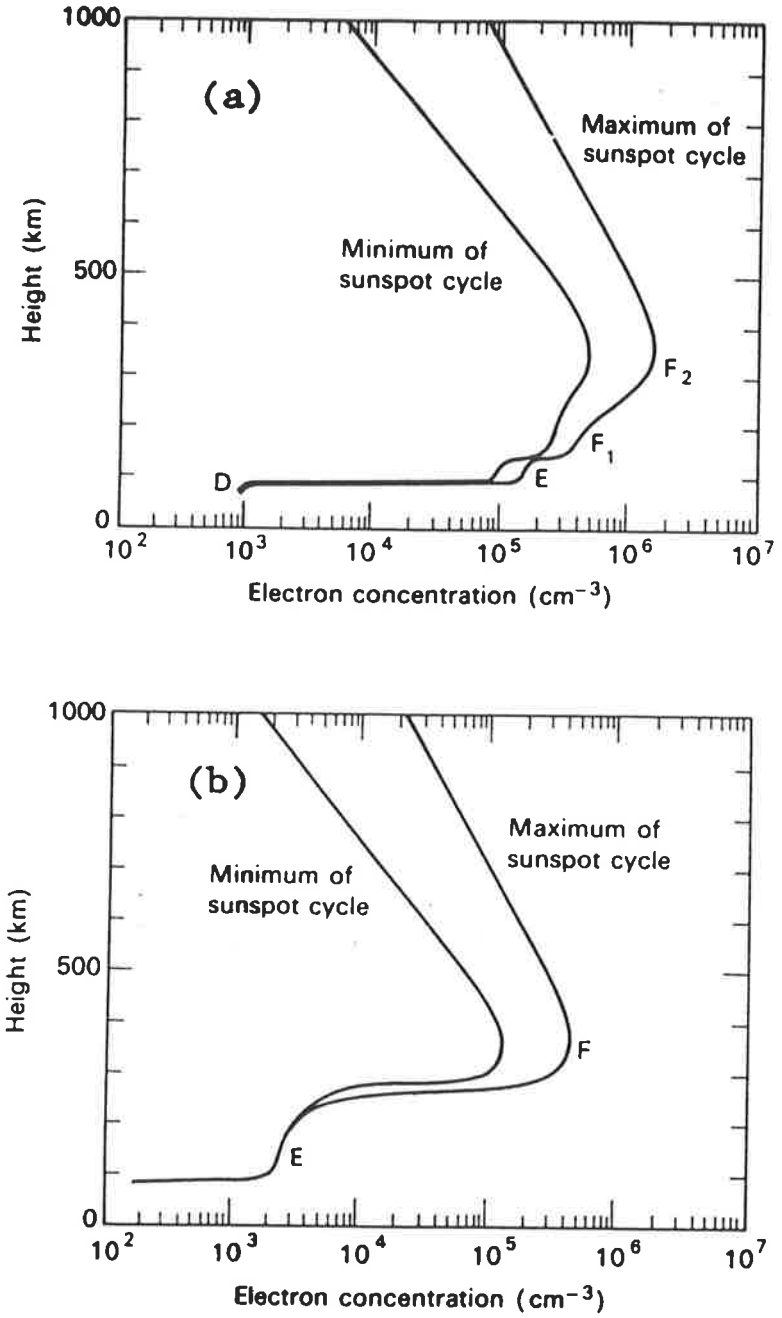

Figure 2.3 (a) Electron number density as a function of height for two extremes of the solar cycle during daytime (McEwan and Phillips 1975).

(b) as above but for nighttime.

simple relationship with the magnitude and height of the production peak related to the angle of incidence of the radiation. In the real ionosphere the situation is more complex; the ionisation products are removed by processes including recombination and electron attachment and the final distribution of ionisation differs from that of electron production.

The distribution of the ionospheric plasma is further modified by mechanical and electromagnetic forces. In the F region, the ion gyro-frequency exceeds the ion collision frequency and horizontal motion of the neutral atmosphere may result in vertical movement of the F2 peak along the geomagnetic field lines. Furthermore, an imposed electric field $\underline{E}$, leads to motion of the plasma across the field lines in the direction of $\underline{E} \times \underline{B}$.

The positive ions are tightly coupled to the neutral thermosphere via momentum transfer in ion-neutral collisions. This process is known as ion-drag and generally acts as a retarding force on the neutral atmosphere at middle and low latitudes. At high latitudes however, the ionospheric plasma is rapidly convected by electric fields of magnetospheric origin. The ion drag then acts as a driving rather than a retarding force and is of primary importance in the dynamics of the polar thermosphere.

2.2.4 The Magnetosphere

The earth's magnetic field approximates that of a dipole within geocentric distances of a few earth radii (R_e). At greater distances the field is distorted by its interaction with the highly-conducting and supersonic solar wind (Figure 2.4). Upstream (sunwards) of the earth the geomagnetic field is compressed and a shock-front is formed at ~$15R_e$, roughly in accordance with the predictions of classical

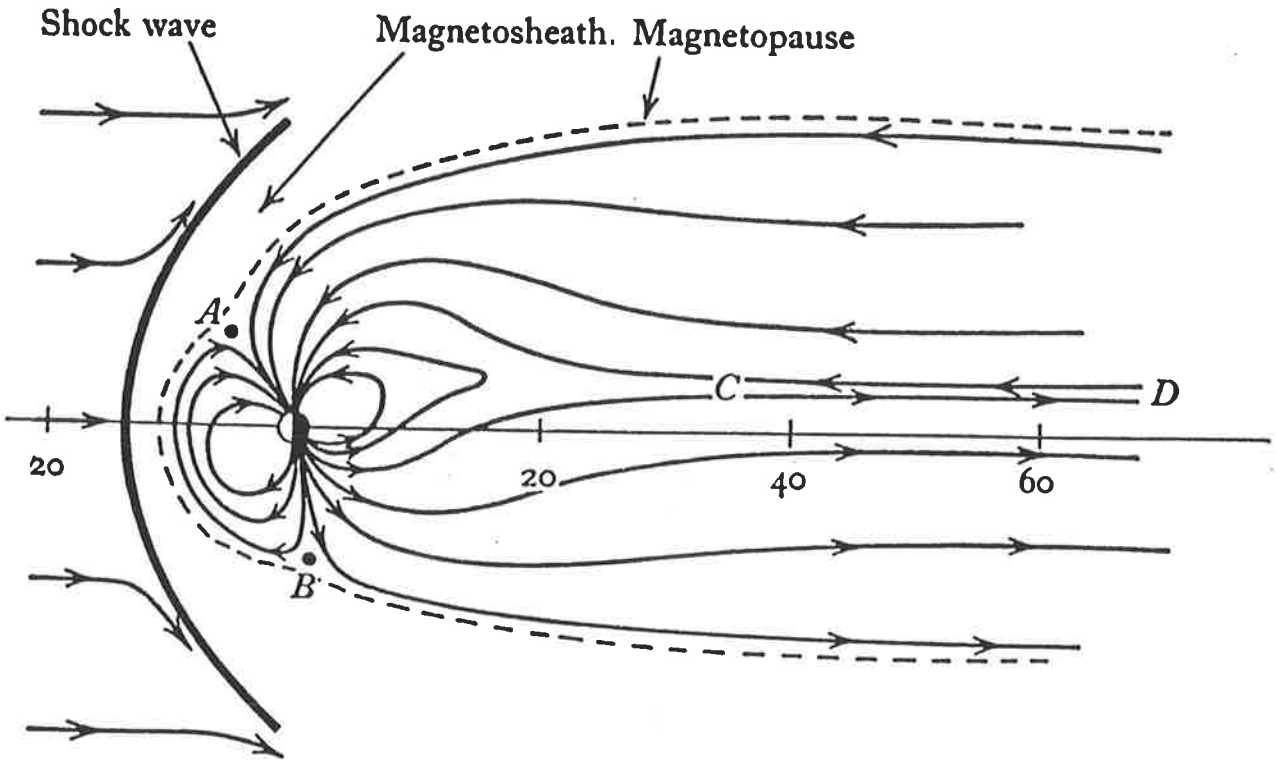

Figure 2.4 Schematic diagram of the earth's magnetosphere. The solar wind, incident from the left, distorts the geomagnetic field. The dashed line represents the magnetopause, inside which the geomagnetic field is confined. Neutral points form at A and B, and a neutral sheet at CD. Geocentric distances are indicated in units of earth radii, along the sun-earth line (Ratcliffe 1972).

fluid mechanics. Downstream the field is stretched out to form the magnetotail, with a diameter of 40-60R_e and a length in excess of 1000R_e. The geomagnetic field is thus largely confined to a region called the magnetosphere, bounded by the magnetopause, around which the solar wind flows. The confinement of the geomagnetic field is not complete; in current models of magnetic field topology, field lines from the earth's polar regions merge with the interplanetary magnetic field (IMF) to produce an 'open' magnetosphere as first proposed by Dungey (1961).

The region between the shock-front and the magnetopause is called the magnetosheath. Upon crossing the shock-front the solar wind is decelerated to subsonic velocity and the plasma within the magnetosheath is thus hotter and denser than the solar wind. Magnetosheath plasma may enter the magnetosphere in two ways: first, in the vicinity of the north and south polar cusps (labelled A and B in Figure 2.4) where the magnetic field strength is very small, magnetosheath particles may directly penetrate the dayside atmosphere at high geomagnetic latitudes. The second mechanism involves the concept of magnetic field line merging and reconnection as described by Dungey (1963). Figure 2.5 illustrates the process for the case when the IMF has a southward component (IMF $B_z<0$). Magnetic field lines carried with the solar wind merge with the geomagnetic field on the dayside and are swept back to the magnetotail. Plasma moving with the field lines is injected into the plasma sheet at the neutral line, where the field lines reconnect. Plasma sheet particles are then convected earthward by the $\underline{E} \times \underline{B}$ drift. The efficiency of the merging process is critically dependent on the sign of the north-south component of the IMF; when this component is northward ($B_z>0$) merging and plasma injection are greatly diminished.

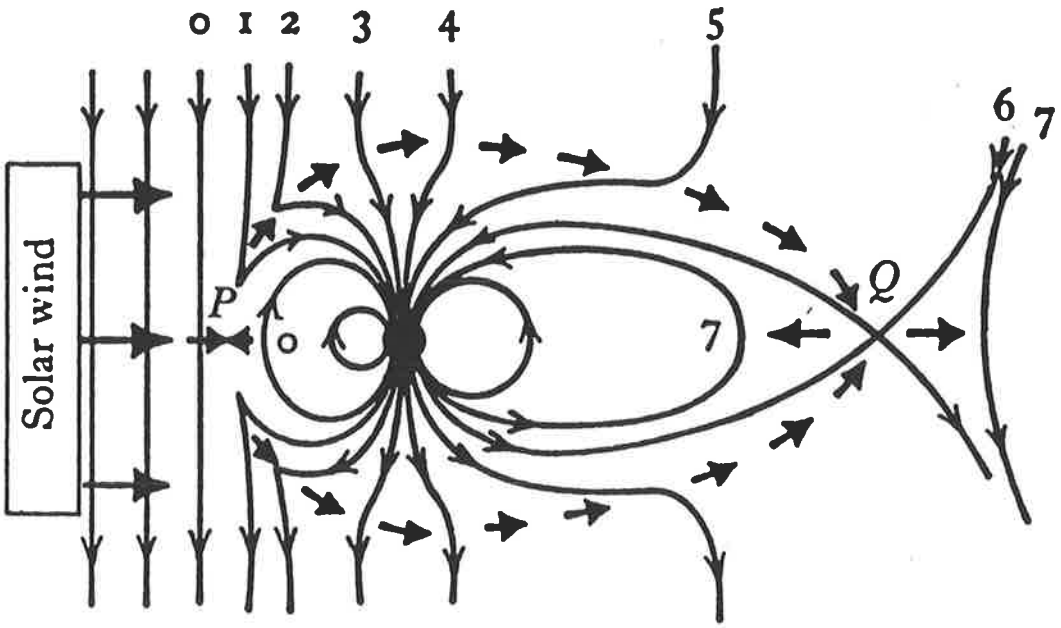

Figure 2.5 Magnetic merging when the z-component of the interplanetary magnetic field is negative. The IMF merges with the geomagnetic field lines on the dayside at P. Field lines are swept antisunward by the solar wind, taking, in succession, the positions 0,1,2 ... and reconnecting at Q. The flow of plasma is represented by the small, heavy arrows (Ratcliffe 1972).

In the merging process, field lines originating in the earth's polar regions are connected to the IMF. The action of the solar wind in flowing through this field constitutes a magnetohydrodynamic generator and establishes large scale electric fields in the magnetotail which are 'mapped' down the near-equipotential geomagnetic field lines into the earth's ionosphere. These electric fields drive a large scale plasma circulation in the polar regions which in turn drives the neutral atmosphere via the ion drag mechanism.

The magnetosphere contains a large quantity of stored energy. From time to time part of this energy is released in a complex process known as a magnetospheric substorm. Understanding of substorms has progressed considerably in the past few decades (Akasofu 1977) and it is now apparent that a sudden reversal of IMF B_z from northward to southward may trigger a series of substorms, each lasting 1-2 hours. During a substorm the magnetospheric structure is rearranged and energy is deposited in the polar atmosphere via electric currents and precipitating particles. This results in intense auroral displays and major perturbations of atmospheric structure and circulation which are often detected globally.

Extensive studies have revealed that in each hemisphere, visible auroras occur most frequently around a roughly annular region known as the auroral oval (Feldstein 1964). Figure 2.6 shows the oval for three levels of geomagnetic activity. In each case the oval encircles the geomagnetic pole and is displaced several degrees toward the nightside. To a first approximation the oval is fixed with respect to the sunward direction and therefore maps onto different regions of the earth's surface at different universal times. The region swept out by the broad midnight sector is often called the auroral zone.

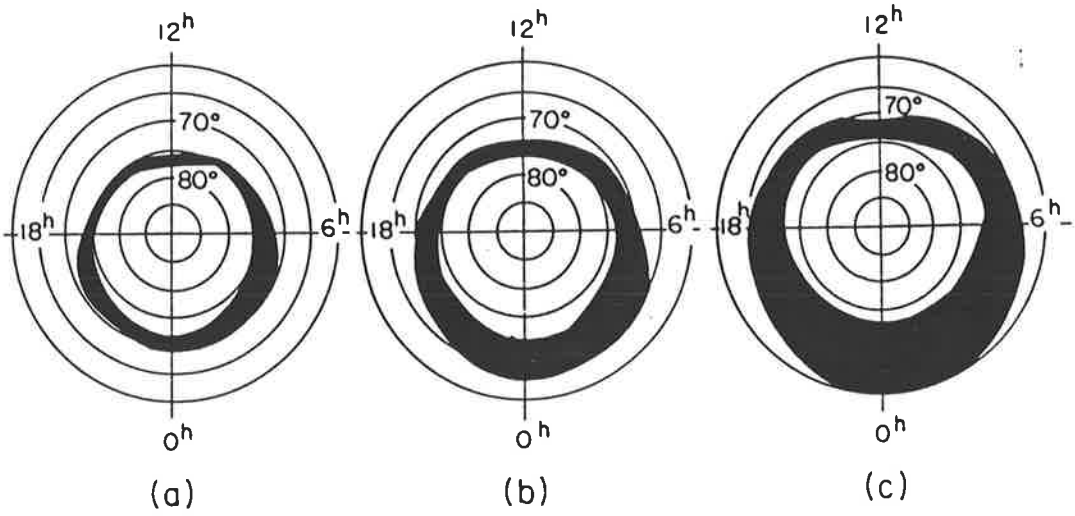

Figure 2.6 The auroral oval in geomagnetic coordinates for three levels of the magnetic disturbance index Q after Starkov and Feldstein (1968). The oval is here defined as the region where the probability of occurrence of discrete zenith aurora is greater than 60%. (a), (b) and (c) are for Q equal to 0, 3 and 7 respectively. The mean oval is similar to (b).

The geometry of the oval is related to the structure of the magnetosphere. Magnetic field lines originating within the oval extend into the distant magnetotail before returning to their conjugate points while field lines originating poleward of the oval are connected to the IMF. The region poleward of the oval is known as the polar cap.

2.3 Dynamics of the Neutral Thermosphere

2.3.1 Review of Early Work

Observations of thermospheric dynamics were very sparse during the 1960s and the early 1970s. A substantial body of thermospheric density data was nevertheless available from measurements of the orbital decay of artificial satellites. These results were summarised by the empirical models of Jacchia (1965,1971) which used the hydrostatic equation and the ideal gas law to calculate vertical distributions of density and composition for various assumed temperature profiles. The model also specified the variation of these quantities with latitude, local time and geomagnetic activity.

The density measurements indicated a diurnal pressure 'bulge' located near the subsolar point and early modelling efforts were concerned with the circulation driven by this system. The pressure gradients from Jacchia's model provided the basis for further calculations which derived the global thermospheric wind system by solving the Navier-Stokes equations (Geisler 1967; Kohl and King 1967). In these calculations it was necessary to include the interaction of the ionosphere with the neutral atmosphere since, at F-layer heights, the ionospheric plasma exerts a strong drag on neutral motions perpendicular to the geomagnetic field.

The calculations showed that the equinoctial circulation was basically a flow from the warm dayside to the cooler nightside with velocities of the order of $100ms^{-1}$. The diurnal variation of ionisation, and hence of ion drag, introduces an asymmetry into the flow; the equatorward nighttime winds are stronger than the poleward daytime winds and the zonally averaged meridional wind is therefore equatorward. Results of these and other earlier studies have been reviewed by several authors (Rishbeth 1972; Dickinson and Rishbeth 1973; Dickinson 1975).

Few opportunities were available at this time for experimental checking of model predictions and most of the techniques used routinely today were still in their infancy. Kent (1970) has reviewed the techniques then available for the measurement of ion and neutral motions; these included radar measurement of meteor trails, incoherent scatter radar and chemical release experiments. The application of Fabry-Perot spectrometers to the measurement of thermospheric winds and temperatures (Chapter 3) was still under development although a number of pioneering studies had been made (Armstrong 1969; Hays and Roble 1971; Nagy et al. 1974). Global scale measurements of thermospheric wind and temperature were not possible until the launch of the Atmosphere Explorer-C spacecraft in 1973.

Theoretical work progressed throughout the 1970s in spite of the dearth of observations. An improved model developed at the United States National Centre for Atmospheric Research (NCAR) resulted in a series of papers which examined the basic state of the thermosphere as a function of season and solar cycle (Dickinson et al. 1975,1977; Roble et al. 1977). The model was two-dimensional and calculated the zonally averaged wind and the temperature perturbation as functions of height and latitude by solving the equations of momentum, energy and

continuity. Background composition and temperature were specified by the empirical model of Hedin et al. (1974) which is based on mass spectrometer data from the OGO-6 spacecraft. The model of Ching and Chiu (1973) was used to specify electron density. These data were then used to evaluate the zonal-mean ion drag for input to the dynamics calculations.

The first published results from the NCAR model were from a simulation of the thermosphere under equinox conditions (Dickinson et al. 1975). Three forcing terms were included in the calculations: solar UV and EUV heating, a momentum source due to the correlation of diurnal variations in neutral winds and ion drag, and a high-latitude heat source associated with Joule heating due to auroral current systems (Cole 1962).

When solar heating alone was considered, the model predicted zonal-mean meridional winds of $\sim 10 ms^{-1}$ in the poleward direction. Incoherent scatter radar observations from the midlatitude sites of Millstone Hill ($42^{o}N$) and St Santin ($45^{o}N$) had, however, revealed equatorward winds of $\sim 20 ms^{-1}$ (Roble et al. 1974; Amayenc 1974). Inclusion of the momentum source due to correlation of winds and ion drag reduced but did not reverse the poleward flow predicted by the model.

Mayr and Volland (1971,1972) had previously shown that solar heating alone could not produce the observed semiannual variations in the thermosphere and a high latitude heat source had been subsequently invoked by Russell and McPherron (1973) and by Murayama (1974). The model winds were brought into agreement with observations by including a high-latitude, hemispherically symmetric heat source, the magnitude of which was adjusted to $\sim 1.2 \times 10^{11} W$.

In a subsequent paper the NCAR model was used to investigate thermospheric circulation and temperature structure under solstice conditions (Dickinson et al. 1977). Observations from Millstone Hill (Roble et al. 1977) indicated a zonal-mean meridional wind of ~45ms^{-1} directed from the summer to the winter hemisphere and zonal-mean zonal winds of ~15ms^{-1} which were eastward in winter and westward in summer. The forcing terms included in the calculations were the same as in the previous study. With the high-latitude heat source initially assumed to be symmetric, reasonable agreement was obtained between model and observed winds but the calculated pole-to-pole temperature difference was considerably less than the empirical OGO-6 value. Better agreement was obtained by introducing an asymmetric source of total magnitude ~2 x 10^{11}W, with the heating in the summer hemisphere approximately 2.5 times that in the winter hemisphere. This increased the pole-to-pole temperature difference to 300K, in accordance with observation. Furthermore, the meridional flow was increased in the summer and reduced in the winter hemisphere such that the calculated summer to winter flow was reversed at F-layer heights, at a latitude of 50-60^{o} in the winter hemisphere.

The development of improved models was accompanied by important progress in experimental techniques. Several groups were active in the field of optical remote sensing and the photoelectric Fabry-Perot spectrometer (FPS) was developed into a powerful instrument for the observation of nighttime thermospheric winds and temperatures (Chapter 3).

Hernandez and Roble (1976) reported FPS measurements from Fritz Peak (40^{o}N) during geomagnetically quiet periods. The observed winds were reasonably well represented by three-dimensional model calculations during equinoctial and winter months although the

observed temperatures were 100-200K higher than those predicted by the OGO-6 model. In a later paper the authors reported the effects on the thermosphere of four geomagnetic storms (Hernandez and Roble 1976). The observations revealed large enhancements of the equatorward nighttime winds with measured velocities up to 640ms^{-1} for conditions of K_p=9, while the zonal winds developed a westward component relative to their values during geomagnetically quiet periods. These results confirmed and extended the findings of several previous studies which had shown enhanced neutral winds at F-region heights at both middle and high latitudes (Smith 1968; Hays and Roble 1971; Meriwether et al. 1973). The wind measurements were, however, very poorly represented by the semiempirical model which had previously been successful in predicting quiet-time behaviour. In particular, the model prediction of eastward (antisunward) winds in the evening hours was frequently contradicted by observations of westward winds of 100-200ms^{-1}.

For some time it had been realised that ions, moving in response to electric fields of magnetospheric origin, could transfer significant momentum to the neutral atmosphere at high latitudes (Cole 1971; Fedder and Banks 1972; Meriwether et al. 1973; Heaps and Megill 1975). During intense geomagnetic activity the high-latitude electric field pattern expands equatorward and can influence the circulation at midlatitude. In particular, the ion drag momentum source drives a sunward flow which is westward in the evening and eastward in the morning, in contrast to that due to solar heating alone. The calculations were repeated with a representation of the convection electric field included and substantially better agreement with observations was obtained, suggesting that ion drag forcing is indeed significant at midlatitudes during geomagnetic storms.

With a large data base established, the authors proceeded to study the monthly variation of thermospheric wind and temperature during solar minimum (Hernandez and Roble 1977). Substantial variability was noted on time scales ranging from hours to days. This was attributed to thermospheric waves generated at high latitudes by substorm phenomena. Such waves had been studied theoretically by several workers (eg Testud 1970; Richmond and Matsushita 1975; Richmond 1978,1979) who concluded that the thermosphere has a large and complex response to substorm-related heating, and that thermospheric gravity waves generated in the auroral zone may propagate globally.

The theoretical conclusions were confirmed by midlatitude observations of wavelike disturbances in the meridional wind which were associated with large geomagnetic storms (Hernandez and Roble 1978). The amplitude of these disturbances ranged from 200-300ms^{-1}. The authors made model calculations which considered the thermospheric response to a single impulsive heating event superimposed upon the background flow. These calculations indicated major perturbations in meridional and zonal components of 500ms^{-1} and 200ms^{-1} respectively, which propagated equatorwards with a wave velocity of 740ms^{-1}.

The work described above showed the importance of high-latitude energy and momentum sources in determining the global thermospheric circulation at F-layer heights. With the development of improved instrumentation and more realistic models, the field of high-latitude thermospheric dynamics expanded rapidly during the 1980s. Before discussing this field we must first consider the ion drag momentum source in more detail.

2.3.2 High-Latitude Electric Fields and Plasma Convection

Previous sections have referred to the electric field pattern (or convection pattern) which is responsible for large-scale circulation of the ionospheric plasma and the neutral atmosphere at high latitudes. This section concerns the morphology of the field and its dependence on the interplanetary magnetic field.

Figure 2.7 shows an idealised version of the distribution of ionospheric equipotentials over the auroral regions. The ionospheric plasma is accelerated in the direction of $\underline{E} \times \underline{B}$ to give a flow pattern whose streamlines are approximately parallel to the equipotentials in the direction indicated by the arrows. The pattern consists of a pair of oppositely directed circulation cells, with antisunward flow across the polar cap and sunward return flow in the morning and evening sectors of the auroral ovals.

Ions convected in this manner are impeded by collisions with the neutral particles and their momentum is transferred to the neutral atmosphere. The electrons however, move freely in the direction of $\underline{E} \times \underline{B}$ since, above ~100km, the electron gyro-frequency exceeds the collision frequency. The electrons constitute a current which maximises at a height of ~110km around the auroral oval. A westward current flows in the morning sector of the oval and an eastward current in the evening sector. These currents are the auroral electrojets.

It must be emphasised that Figure 2.7 is a highly idealised representation of the convection pattern. The real pattern undergoes large variations on time scales of minutes and shows significant departures from the figure, although the two-cell character is generally maintained. More realistic models have been inferred from measurements of electric fields by the OGO-6 and Dynamics Explorer-2

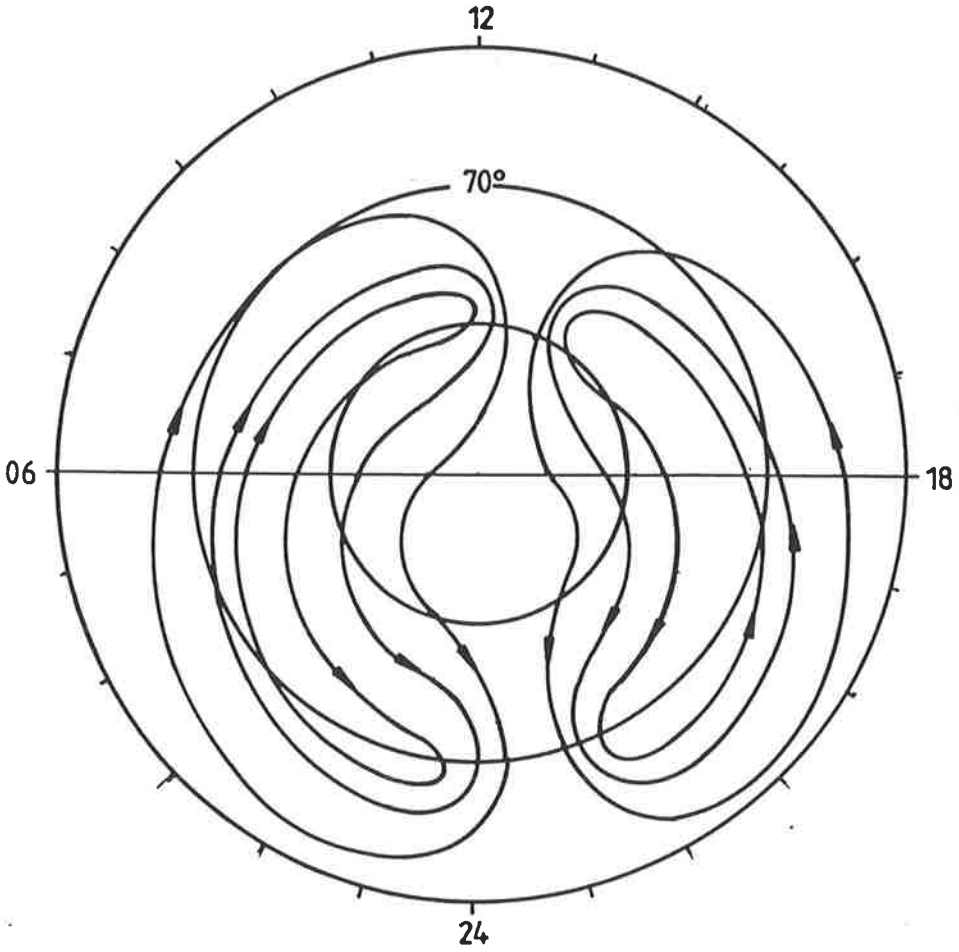

Figure 2.7 Figure 1. Idealised representation of the high-latitude ion convection pattern viewed from above the southern polar cap._The curves represent equipotentials; plasma is convected roughly parallel to these in the direction indicated by the arrows. Coordinates are invariant latitude and magnetic local time. Adapted from Heelis et al.(1982).

spacecraft and of ion drift velocities from Atmosphere Explorer-C. The need for improved field models has become particularly acute with recent advances in thermospheric circulation modelling.

Early studies established that the convection pattern responded to changes in the IMF and could be characterised most of the time by a small number of representative 'signatures'. In an analysis of OGO-6 data obtained from dawn-dusk crossings, Heppner (1972) identified two common signatures which were related to the y-component (in solar ecliptic coordinates) of the IMF (IMF B_y). The effect of IMF B_y was to change the relative sizes of the dawn and dusk convection cells, such that for IMF $B_y<0$ the northern hemisphere dawn cell and the southern hemisphere dusk cell were enlarged, while for IMF $B_y>0$ the northern dusk and southern dawn cells were enlarged.

These 'sun-aligned' models, in which the polar cap flow was precisely antisunward, were subsequently revised (Heppner 1977) to accommodate electric field measurements near the midnight region (Maynard 1974). An analytical representation by Volland (1978) permitted the use of the revised patterns in the evaluation of ion drag momentum forcing by thermospheric general circulation models (TGCMs).

Vastly improved coverage of electric field and ion drift measurements was made possible by Dynamics Explorer-2, launched in 1981. This led to further modification of convection models as reported by Heppner and Maynard (1983,1986). The field models presented in the former paper have been widely used in thermospheric circulation modelling and are illustrated in Figure 2.8.

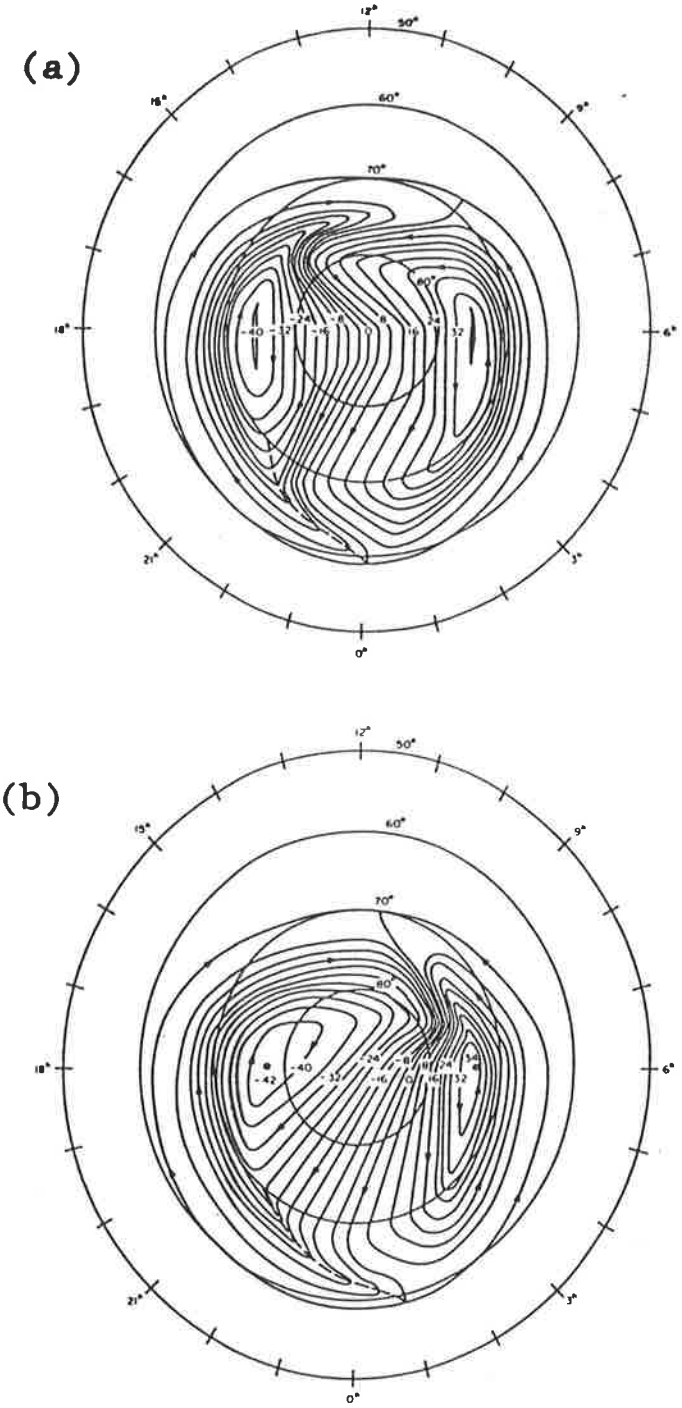

Figure 2.8 Ion convection patterns due to Heppner and Maynard (1983).

(a) The A-2 model, applied to the northern hemisphere with IMF B_y negative and to the southern hemisphere with IMF B_y positive.

(b) The B-2 model, applied to the northern hemisphere with IMF B_y positive and to the southern hemisphere with IMF B_y negative.

Departures from these models were observed most often when the IMF z-component was positive. In particular, regions of sunward convection were occasionally observed within the polar cap. Several authors have attempted to describe polar cap sunward convection in terms of three or four-cell models (Burke et al. 1979; Potemra et al. 1984; Reiff and Burch 1985). Such models have difficulty in explaining convective continuity on the nightside and are rejected by Heppner and Maynard who favour an explanation involving distortion of the polar cap flow within a two-cell model.

2.3.3 The High-Latitude Thermosphere

Observations in the early 1970s had pointed to the importance of ion drag in controlling neutral winds in the high-latitude thermosphere (Rees 1971,1973; Meriwether 1973). However, a detailed picture of high-latitude circulation did not emerge until the next decade when Heppner and Miller (1982) reported wind measurements from 39 chemical release experiments, conducted at auroral and polar cap sites, in the period 1967-1979. The wind vectors above 160km were better ordered when presented in geomagnetic coordinates (invariant latitude and magnetic local time) and agreed substantially with the two-cell patterns of ion convection due to Heppner (1977). Figure 2.9 shows the observed vectors superimposed on Heppner's convection patterns. The best agreement was obtained by shifting the vectors two hours earlier in time, this being the time constant for the response of the neutral thermosphere to changes in ion drag forcing. The authors stressed the importance of geomagnetic coordinates in the presentation of high-latitude wind systems and pointed out that the successful modelling of these systems depends critically on the realistic representation of high-latitude electric fields.

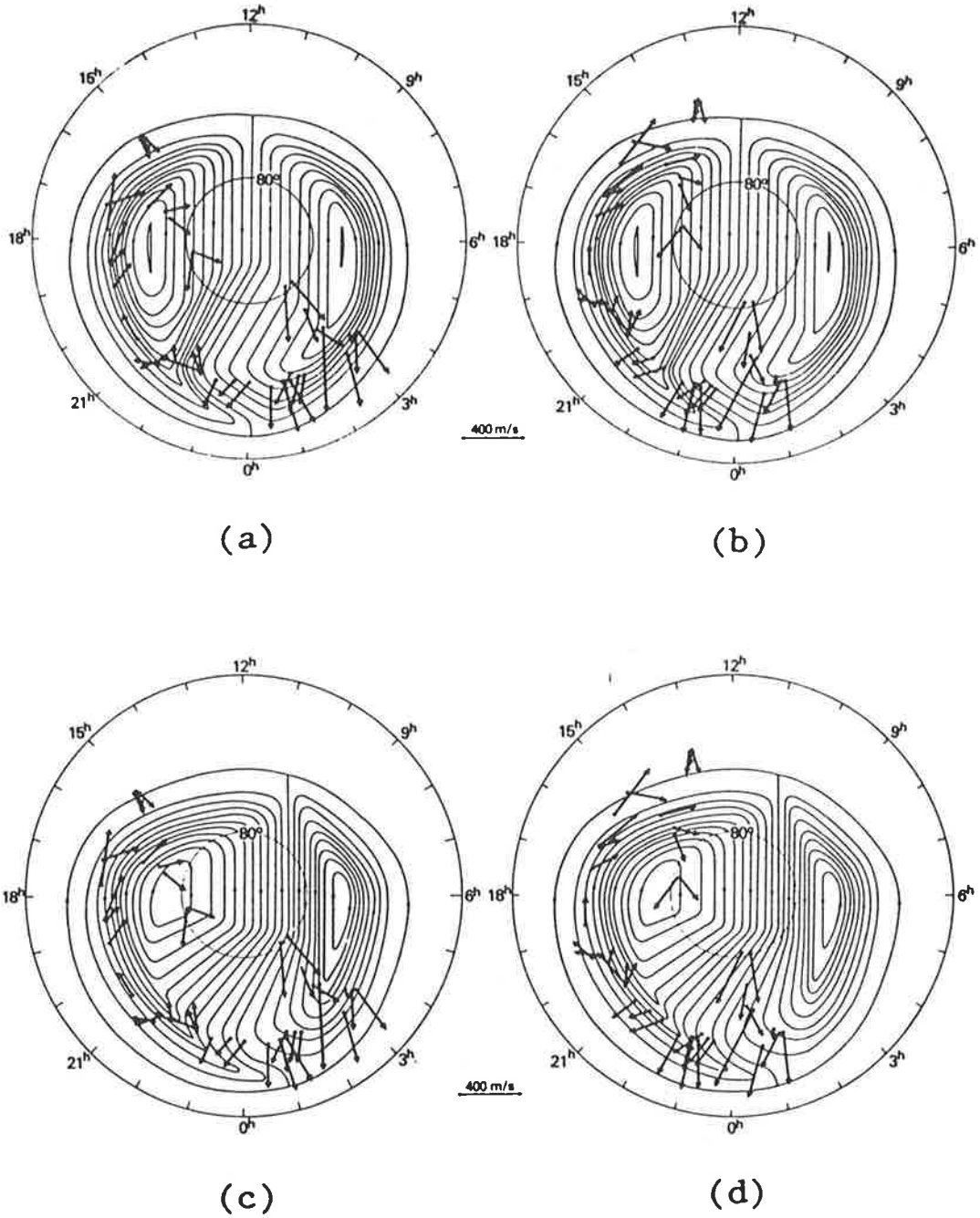

Figure 2.9 Wind vectors of Heppner and Miller (1982) superimposed on model convection patterns due to Heppner (1977). The coordinates are invariant latitude and magnetic local time.

(a) Wind vectors superimposed on the model A pattern, applied to the northern hemisphere when IMF $B_y<0$.

(b) As in (a) but with vectors shifted two hours earlier.

(c) Wind vectors superimposed on the model B pattern, applied to the northern hemisphere when IMF $B_y>0$.

(d) As in (c) but with vectors shifted two hours earlier.

Understanding of the high-latitude thermosphere increased rapidly during the 1980s. This was largely due to (a) the development of more-sophisticated thermospheric general circulation models (TGCMs) and (b) the vastly improved observational coverage provided by the Dynamics Explorer-2 (DE-2) spacecraft. Of the models, two have been prominent in recent years; these are the NCAR model described by Dickinson et al. (1981) and the University College, London (UCL) model of Fuller-Rowell and Rees (1980). Both models yield three-dimensional, time-dependent solutions to the basic atmospheric equations and can specify wind velocity, temperature and composition on a grid of a few degrees spacing and at a number of pressure levels from ~100 to ~500km altitude. Model inputs include solar UV and EUV heating, high-latitude energy and momentum sources and representations of the ionosphere and the high-latitude electric field. Both models have undergone numerous improvements since first reported.

The models have been used to investigate both the steady state of the thermosphere and its response to geomagnetic and other perturbations, with particular emphasis on high-latitude processes. Early studies established that ion drag drives a high-latitude wind system which resembles the two-cell pattern of ion convection (Rees et al. 1980, Roble et al. 1982). The universal time dependence of the circulation was ascribed to the separation of geographic and geomagnetic poles. Simulation of geomagnetic substorms was achieved by using time-varying electric fields and electron density; this resulted in the production of large amplitude waves which propagated outward from the auroral zones (Fuller-Rowell and Rees 1981).

The development of advanced TGCM's coincided with significant improvements in ground-based and satellite-borne instruments. Novel approaches such as the TESS concept (Hernandez et al. 1981) and the

use of imaging photon detectors led to an order of magnitude increase in the sensitivity of Fabry-Perot interferometers, allowing wind measurements to be made with a time resolution of a few minutes.

One of the most important experimental developments was the DE-2 satellite, launched into polar orbit in 1981 (Hoffmann and Schmerling 1981). The spacecraft was equipped to measure neutral winds and temperatures at an altitude of ~300km, using a Fabry-Perot spectrometer (Hays et al. 1981) and the wind and temperature spectrometer described by Spencer et al. (1981). Additional instruments provided auroral images and measurements of ion drift and electric fields. The DE-2 observations complemented ground-based programs by providing extended geographic coverage at a fixed local time, thus allowing universal and local time effects to be separated.

The first results from DE-2 were reported by Killeen et al. (1982,1983) and by Hays et al. (1984). These papers considered a data set consisting of many polar passes which covered the full range of universal times. The results indicated that the wind system above 60^{o} latitude was controlled by ion drag forcing, in agreement with the findings of Heppner and Miller (1982) and the TGCM predictions. The observed winds showed a strong universal time dependence due to the separation of geographic and geomagnetic poles.

In the paper of Hays et al. (1984) the DE-2 observations were compared with the predictions of the NCAR and UCL models, which were run using input conditions appropriate to the time of the observations. Examples of the experimental results and model predictions are shown in Figure 2.10. Both models predicted the observed winds reasonably well but failed to describe adequately the thermodynamics of the region.

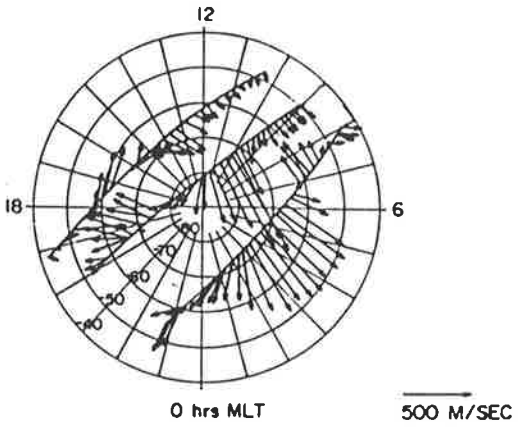

(a)

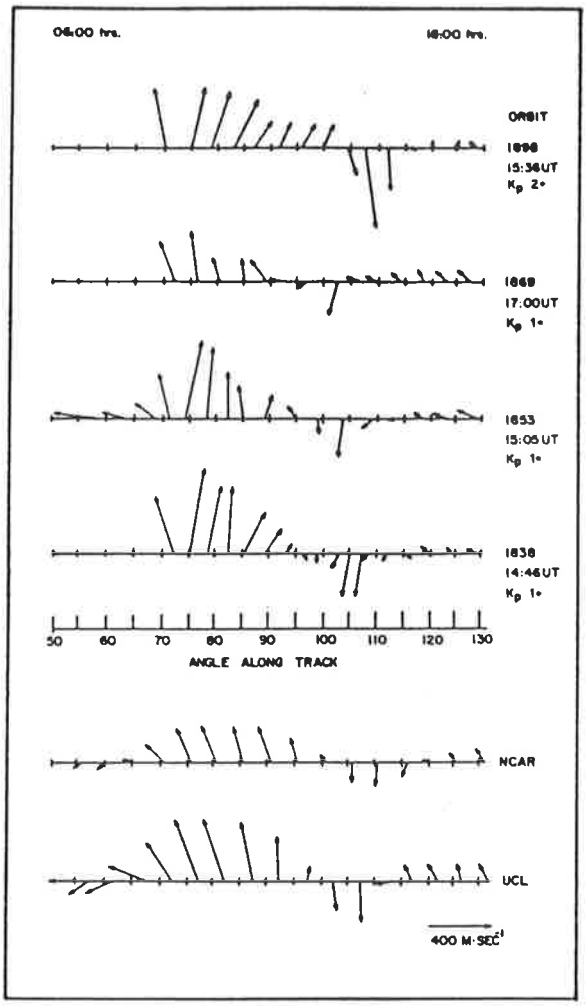

(b)

Figure 2.10 (a) Neutral wind vectors from DE-2 obtained on three passes over the south pole in the 2100 LT to 0900 LT plane. Data are displayed in geomagnetic coordinates. Strong antisunward winds were observed across the polar cap with sunward return flow in the dusk sector of the auroral oval.

(b) Neutral wind vectors plotted along the track of DE-2 for four north pole passes near 1500 UT. The satellite crossed the pole from 0600 to 1800 LT. The predictions of the NCAR and UCL models are also shown for the same local time plane and universal time (Hays et al. 1984).

A number of subsequent papers reported observations both from ground-based sites and from DE-2, all of which provided further confirmation of the dominant role of ion drag forcing at high latitudes (eg Rees et al. 1985a,b,c). With the main features of high-latitude circulation thus established, experimental and theoretical efforts have recently been directed to other areas, two of which concern the present project.

Section 2.3.2 described asymmetries in the high-latitude plasma convection which are related to the y-component of the IMF. Similar effects should also occur in the neutral circulation which is itself driven by the ion convection. Asymmetry in the neutral circulation was observed at Spitzbergen (78^{o}N, 16^{o}E) by McCormac and Smith (1984) who found evidence for an enlarged dusk circulation cell when IMF B_y was positive. A corresponding enlargement of the dusk cell was not observed for negative IMF B_y since this cell is suppressed by the Coriolis force. Similar conclusions were obtained by McCormac et al. (1985) who reported data from dawn-dusk crossings of the northern polar cap by DE-2. The position of the antisunward 'jet' across the polar cap was found to shift from the dawn to the dusk side as IMF B_y changed from positive to negative. Successful modelling of IMF B_y dependent asymmetries was reported by Rees et al. (1986).

Another currently active area is the field of thermospheric gravity waves. Such waves were studied extensively during the 1970s yet it was long assumed that the associated vertical velocities were small (a few ms^{-1}) at midlatitude. Using a TESS instrument, Hernandez (1982) observed vertical motions of up to $50ms^{-1}$ at Fritz Peak which were ascribed to the passage overhead of gravity waves generated within the auroral zones.

There have since been many observations of large vertical motions at high latitudes (eg Spencer et al. 1982; Herrero et al. 1984; Rees et al. 1984). The studies have shown that the thermosphere has a large, rapid and complex response to impulsive heating resulting from auroral processes. Vertical velocities of up to $50ms^{-1}$ are frequently observed even during geomagnetically quiet periods. During disturbed periods vertical velocities may exceed $100ms^{-1}$.

2.4 Summary and Outlook

The mechanism of ion drag plays an important role in determining thermospheric circulation at all latitudes. At high latitudes where the ionospheric plasma moves rapidly, ion drag is the principal momentum source for the neutral thermosphere. The resulting circulation resembles the basic two-cell pattern of ion convection. Asymmetries in this pattern are related to the y-component of the interplanetary magnetic field.

High-latitude heat sources significantly affect the global thermospheric circulation and are associated with Joule and particle heating in the auroral oval and polar cap. Impulsive heating events, associated with geomagnetic substorms, may generate large-amplitude gravity waves which propagate globally.

Understanding of the thermosphere has increased enormously over the past decade; this has been largely due to the development of global-scale observing techniques together with the use of sophisticated numerical models to aid in the interpretation of results. There has, however, been a serious imbalance in the observing program; almost all of the high-latitude, ground-based observations have been from the northern hemisphere. The only significant data base

from high southern latitudes is that due to DE-2 which ceased operation in 1983. There is therefore a need for extensive ground-based observations from this region. Mawson station, located in the vicinity of the auroral oval, is well suited to fulfil this role and it is hoped that the present project will help to restore the observational balance.

Before concluding this chapter it is perhaps appropriate to consider briefly the future direction of thermospheric research. It is now obvious that the neutral thermosphere is not an isolated system; it is coupled to the ionosphere and magnetosphere via ion drag and to the mesosphere via upward propagating tides and gravity waves. The coupling of these regions is crudely represented by current atmospheric models and the principal scientific challenge today is to understand the coupled system *as a whole*. This is the aim of the CEDAR (Coupling, Energetics and Dynamics of Atmospheric Regions) program which represents the main thrust of US optical atmospheric research through to the mid-1990s.

CEDAR will involve coordinated, global-scale campaigns using a variety of observing techniques. The atmospheric regions to be studied include the mesosphere, thermosphere, exosphere, ionosphere, magnetosphere and plasmasphere. Campaigns will first consider the mean state of the regions and then proceed to the study of perturbations resulting from geomagnetic substorms etc. It is envisaged that existing facilities will first be upgraded and then complemented by new 'state of the art' instrumentation to be deployed in the early 1990s. Parallel activity will occur in the fields of atmospheric modelling and data reduction.

It is hoped that CEDAR will eventually yield an order of magnitude improvement in scientific return. The next decade promises to be a significant period for atmospheric science.

Chapter 3

OPTICAL REMOTE SENSING OF THERMOSPHERIC TEMPERATURE AND WIND VELOCITY

3.1 Introduction

Techniques of optical remote sensing have been used for many years in the study of the upper atmosphere. The scope of such techniques has until recently been largely restricted to the use of low resolution devices such as photometers. These devices have proved successful in the investigation of radiation sources and photochemical processes but have yielded little information on the thermal and dynamical properties of the atmosphere.

Improvements in the sensitivity and reliability of high-resolution scanning spectrometers have, over the past two decades, allowed these instruments to develop into powerful and cost effective tools for probing the thermosphere, both from the ground and from space. The photoelectric Fabry-Perot spectrometer has proved to be one of the most successful instruments in this class and is the instrument used in this study.

The experimental technique, now well established, is based on the measurement of the Doppler shift and broadening of atomic emission lines in the airglow and aurora. The line width at half intensity, $\delta_B\lambda$ is given by (Buisson and Fabry 1912) :

$$\delta_B\lambda = 2(\ln 2)^{1/2}(2kT/M)^{1/2}\lambda_0/c \qquad (3.1)$$

where T and M are the absolute temperature and atomic weight of the emitting species, λ_0 is the centre wavelength, c the speed of light

and k is Boltzmann's constant.

Bulk motion of the emitting atoms with respect to the spectrometer causes the line to be Doppler shifted to a wavelength

$$\lambda' = \lambda_0(1 + v/c) \qquad (3.2)$$

where v is the component of the velocity along the line of sight and is defined as positive away from the spectrometer. Measurements of $\delta\lambda_B$ and $(\lambda'-\lambda_0)$ thus allow the determination of T and v. The assumption that T represents the temperature of the bulk neutral atmosphere implies equilibrium between the emitting species and the dominant neutral species. The validity of this assumption depends on the processes of excitation and emission. The height interval to which the measurements are assigned depends on the height distribution of the emitting species. These factors will be discussed further in section 3.2.

It is instructive to consider typical values of $\delta_B\lambda$ and $(\lambda'-\lambda_0)$ encountered in the upper thermosphere. For the λ630nm emission of atomic oxygen (M = 16) and taking T = 1000K and v = 10ms^{-1} we obtain $\delta_B\lambda$ = 3.6pm and $(\lambda'-\lambda_0)$ = 0.02pm. Clearly, a very high resolution spectrometer is required to measure these quantities. This requirement, together with the low radiance of the airglow and auroral sources, makes the Fabry-Perot spectrometer an excellent choice, combining as it does the properties of high resolution and light gathering ability.

3.2 The $O(^1D)$ λ630nm Emission in the Night Airglow and Aurora

The $O(^1D)$ state is excited by the following processes in the night airglow and aurora:

a) Auroral electron impact, causing transitions from the ^3P ground state

$$O(^3P) + e^* \rightarrow O(^1D) + e \qquad (3.3)$$

b) Dissociative recombination of O_2^+

$$O_2^+ + e \rightarrow O(^1D) + O \qquad (3.4)$$

c) Excitation by thermal electrons

$$O(^3P) + e \rightarrow O(^1D) + e \qquad (3.5)$$

d) Electron impact dissociation of O_2

$$O_2 + e^* \rightarrow O(^1D) + O \qquad (3.6)$$

e) Cascading from higher electronic states

$$O(^1S) \rightarrow O(^1D) + h\nu(558nm) \qquad (3.7)$$

The above sources have been shown to be insufficient to explain the observed emission rate profile obtained from coordinated rocket and satellite measurements of aurora (Rees et al. 1977; Sharp et al. 1979,1983). The reaction

f) $$N(^2D) + O_2 \rightarrow O(^1D) + NO \qquad (3.8)$$

has been proposed as the missing source by Rusch et al. (1978). Comprehensive auroral model calculations including (3.8) have successfully reproduced the observed altitude profile of λ630nm emission (Rees and Roble 1986) and suggest that this reaction is in fact the major source of thermospheric $O(^1D)$ atoms.

The $O(^1D)$ state has a radiative lifetime of ~110s and is effectively quenched by collisions with molecular nitrogen at low altitudes. Above 500km the production of $O(^1D)$ is negligible due to the low density of atomic oxygen. Figure 3.1 shows measured height profiles of the λ630nm volume emission rate obtained from the Visible

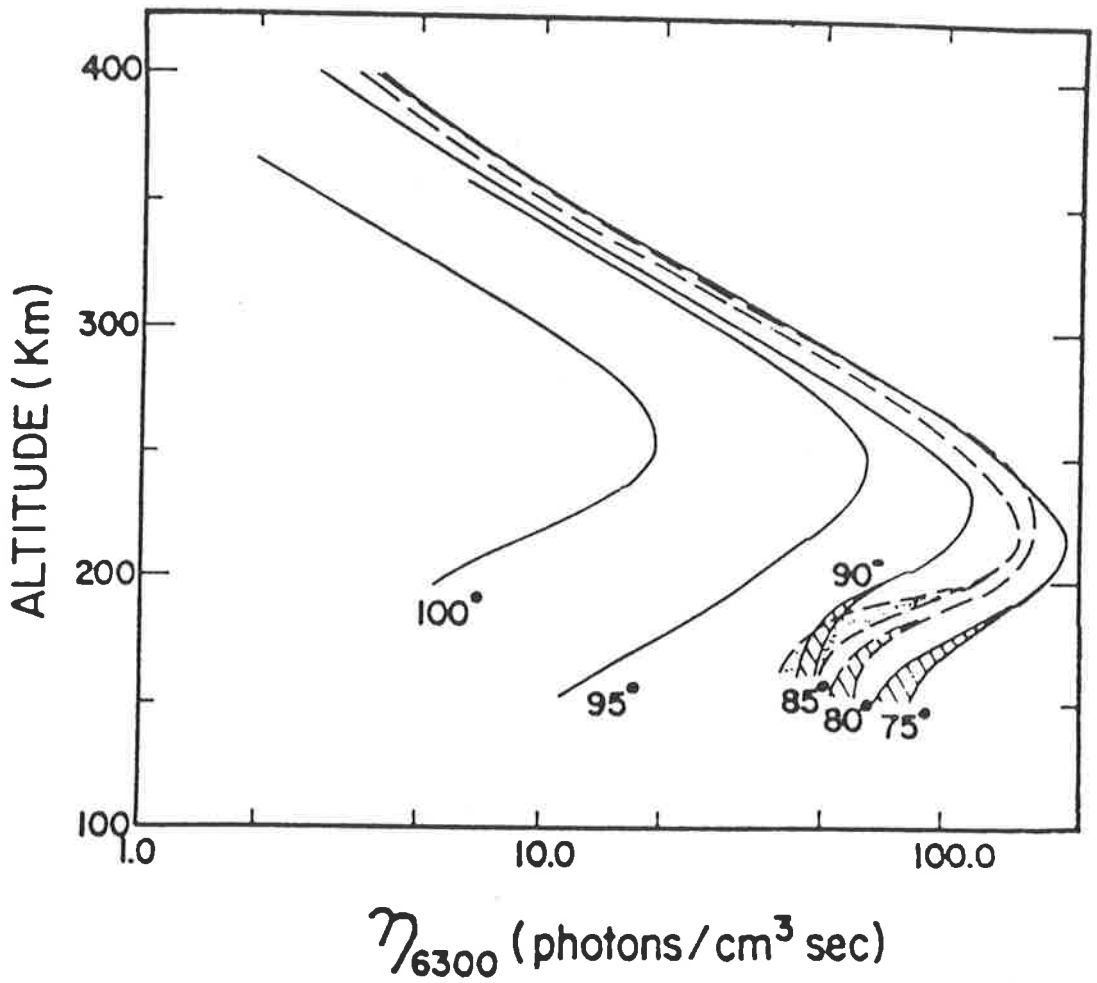

Figure 3.1 Altitude profile of the volume emission rate of [OI] 630nm radiation measured by the Visible Airglow Experiment aboard the Atmosphere Explorer-C spacecraft. Measurements were made under non-auroral conditions for a range of solar zenith angles (Hays et al. 1978).

Airglow Experiment aboard the Atmosphere Explorer-C (AEC) spacecraft (Hays et al. 1978). The measurements were made under non-auroral conditions for a range of solar zenith angles during twilight. The data show that the peak of the emitting layer is at 200-250km altitude and that the peak altitude increases with solar zenith angle. The thickness of the layer at half intensity is around 100km.

The radiance or surface brightness of atmospheric emissions is directly related to the line-of-sight integral of the volume emission rate. A commonly used unit of surface brightness is the rayleigh, denoted R, which is equal to $10^{10}/4\pi$ photons.s^{-1}.m^{-2}.steradian^{-1}. Under non-auroral conditions, λ630nm intensities are of the order of 100R. In bright auroras the intensity may exceed 100kR.

3.3 The $O(^1D)$ λ630nm Dayglow

During the daytime the following mechanisms cause excitation of $O(^1D)$ in addition to those discussed in section 3.2.

a) Photo-dissociation of molecular oxygen by solar ultraviolet radiation in the Schumann-Runge continuum (135-175nm)

$$O_2 + h\nu(135\text{-}175\text{nm}) \rightarrow O(^1D) + O \qquad (3.9)$$

b) Excitation by impact of local and conjugate photoelectrons

$$O(^3P) + e \rightarrow O(^1D) + e \qquad (3.10)$$

The main source above 200km is photoelectron excitation. The main source below 200km is photodissociation. Emission intensities are typically of the order of a few kilorayleighs.

Figure 3.2 shows observed volume emission rate profiles from AEC, taken at equatorial latitudes during summer and winter (Torr et al. 1981). The peak emission rate is ~200 photons.cm^{-3}.s^{-1} and the peak height ~200km in both cases. There is a substantial increase in the summer emission rates over the winter rates above ~250km altitude.

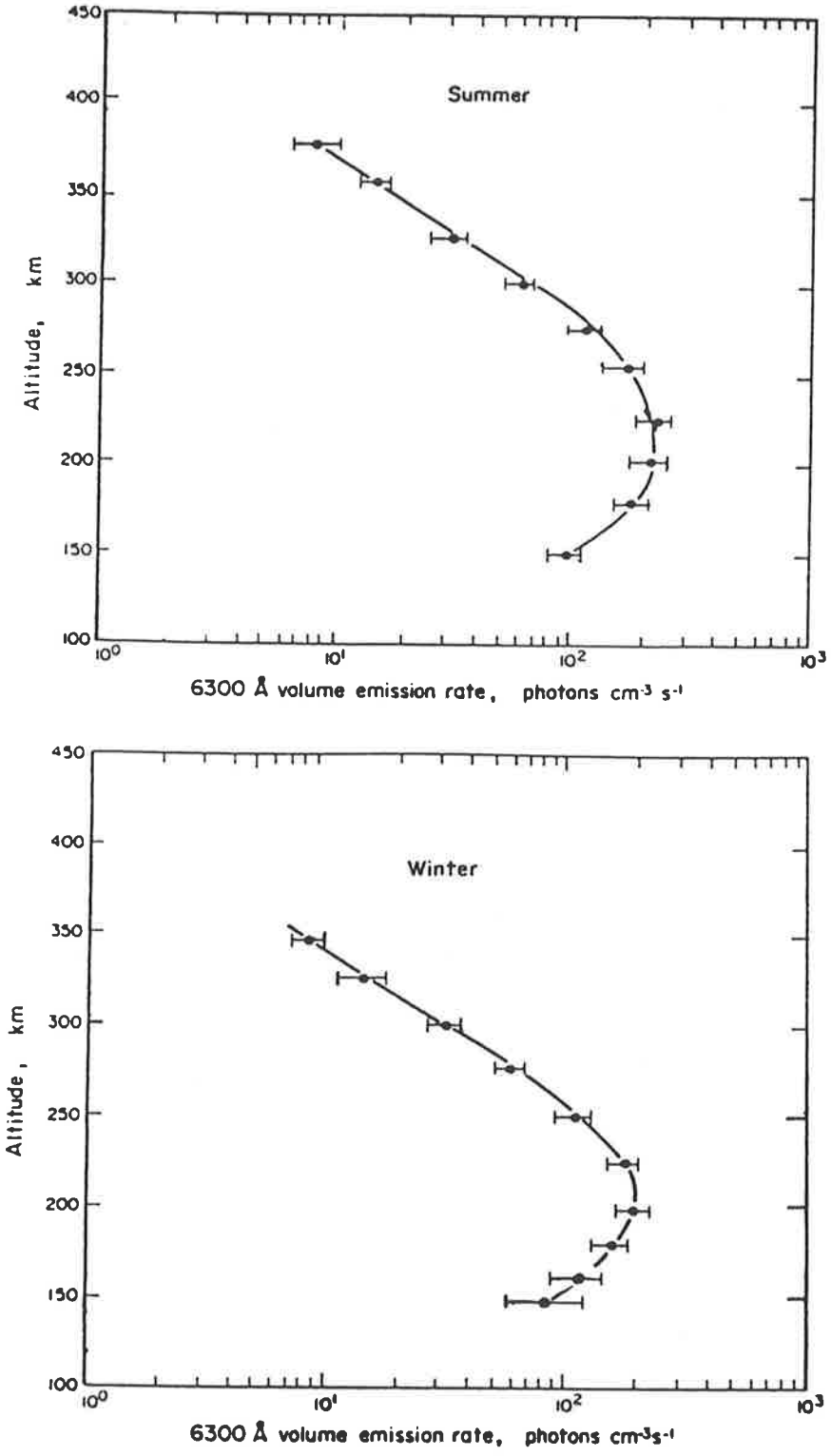

Figure 3.2 Altitude profiles of the volume emission rate of [OI] λ630nm dayglow measured by AEC during summer and winter (Torr et al. 1981).

3.4 Observations of the λ630nm Dayglow

3.4.1 Introduction

Ground-based observations of dayglow emission lines are made difficult by the enormous background of scattered sunlight present in the day sky. Application of the techniques described in section 3.1 requires that the emission line be isolated with a high degree of spectral purity. The difficulties imposed by this requirement have delayed the development of routine and reliable optical techniques for monitoring thermospheric dynamics over the full diurnal cycle.

Before reviewing the current state of affairs it is instructive to consider some of the problems associated with ground-based dayglow observations.

3.4.2 The Background of Scattered Sunlight

The intensity of scattered sunlight in the wavelength region near 630nm is $\sim 5 \times 10^{4}$ kR.nm^{-1} (Noxon and Goody 1962; Miller and Fastie 1972). Although the λ630nm emission is one of the brightest features of the visible dayglow spectrum, it contributes only a small fraction of the total radiation received from the day sky. For a spectrometer bandwidth comparable to the width of the emission line, the λ630nm emission contributes about 1-2% of the total signal. The problem is therefore to isolate this weak feature with sufficient precision to allow meaningful determination of Doppler shift and width.

A further complication is introduced by the spectral structure of the background, which is principally Rayleigh-scattered sunlight and therefore contains the Fraunhofer absorption lines. Figure 3.3 shows the solar spectrum in the region of 630nm (Delbouille et al. 1973);

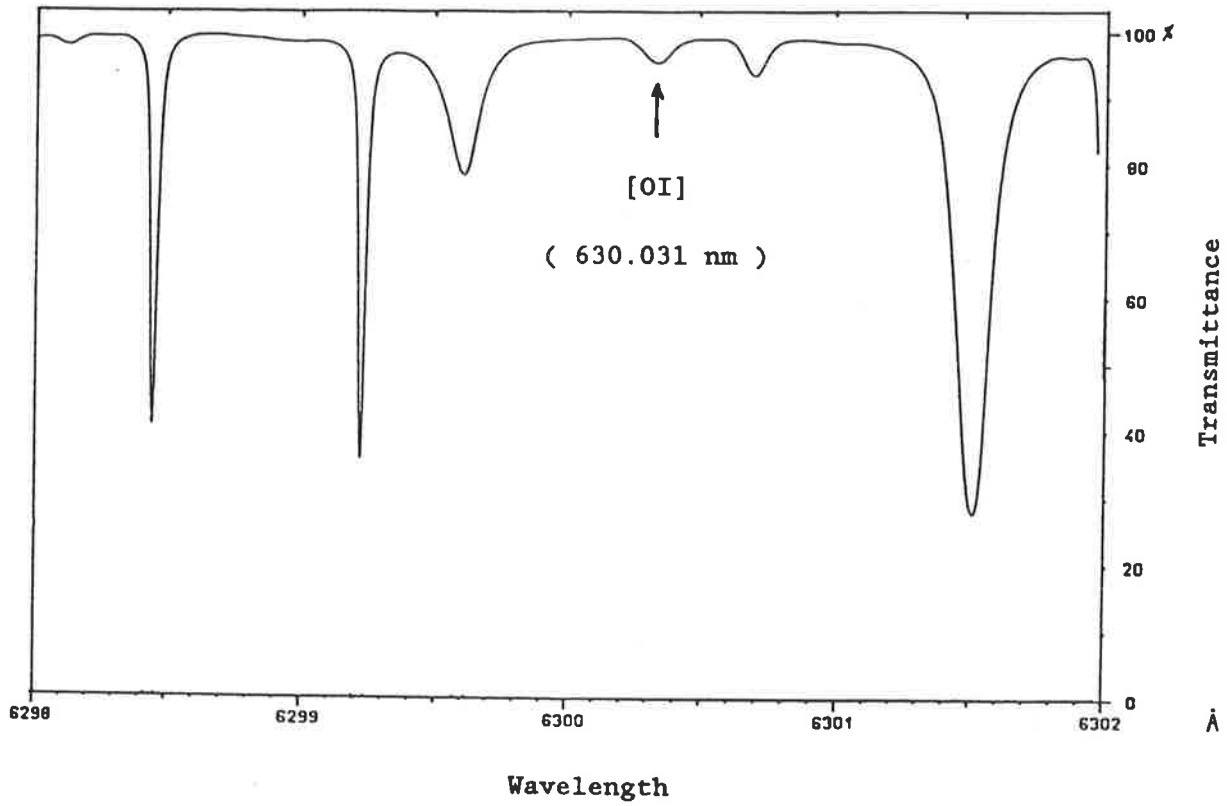

Figure 3.3 The solar spectrum in the region of 630nm. The arrow indicates the [OI] absorption line at λ630.031nm.

the emission line appears near the bottom of a small Fraunhofer line produced by atomic oxygen in the sun's photosphere, which is about 4% deep referred to the local continuum. The emission line thus appears in a region of considerable spectral structure and this must be removed if the correct line shape is to be inferred.

3.4.3 The Ring Effect

The Ring effect (Grainger and Ring 1962) arises from the presence of a continuous, unpolarised component in the skylight resulting from Rayleigh-Brillouin and rotational Raman scattering (Kattawar et al. 1981). The intensity of the Ring component has been observed up to a few percent of the scattered sunlight intensity and increases with solar zenith angle. The sky and solar spectra therefore differ not only in the presence of the emission line but also in the presence of the Ring component.

The Ring component affects the analysis of dayglow spectra as follows. Suppose the spectral structure of scattered sunlight is to be removed from the sky spectrum by subtraction of a suitably normalised solar spectrum (Figure 3.4). The Fraunhofer line is less deep in the sky spectrum than in the normalised solar spectrum and a positive feature results on subtraction. The presence of this feature complicates the process of isolation of the emission line.

3.4.4 Previous Observations

Successful ground-based observations of the λ630nm dayglow were first performed by Noxon and Goody (1962). More extensive observations were reported by Noxon (1964). Using a spectral scanning polarimeter with a bandwidth of 0.1nm, emission intensities in the range 5 to 50kR were observed. The observed intensities showed considerable

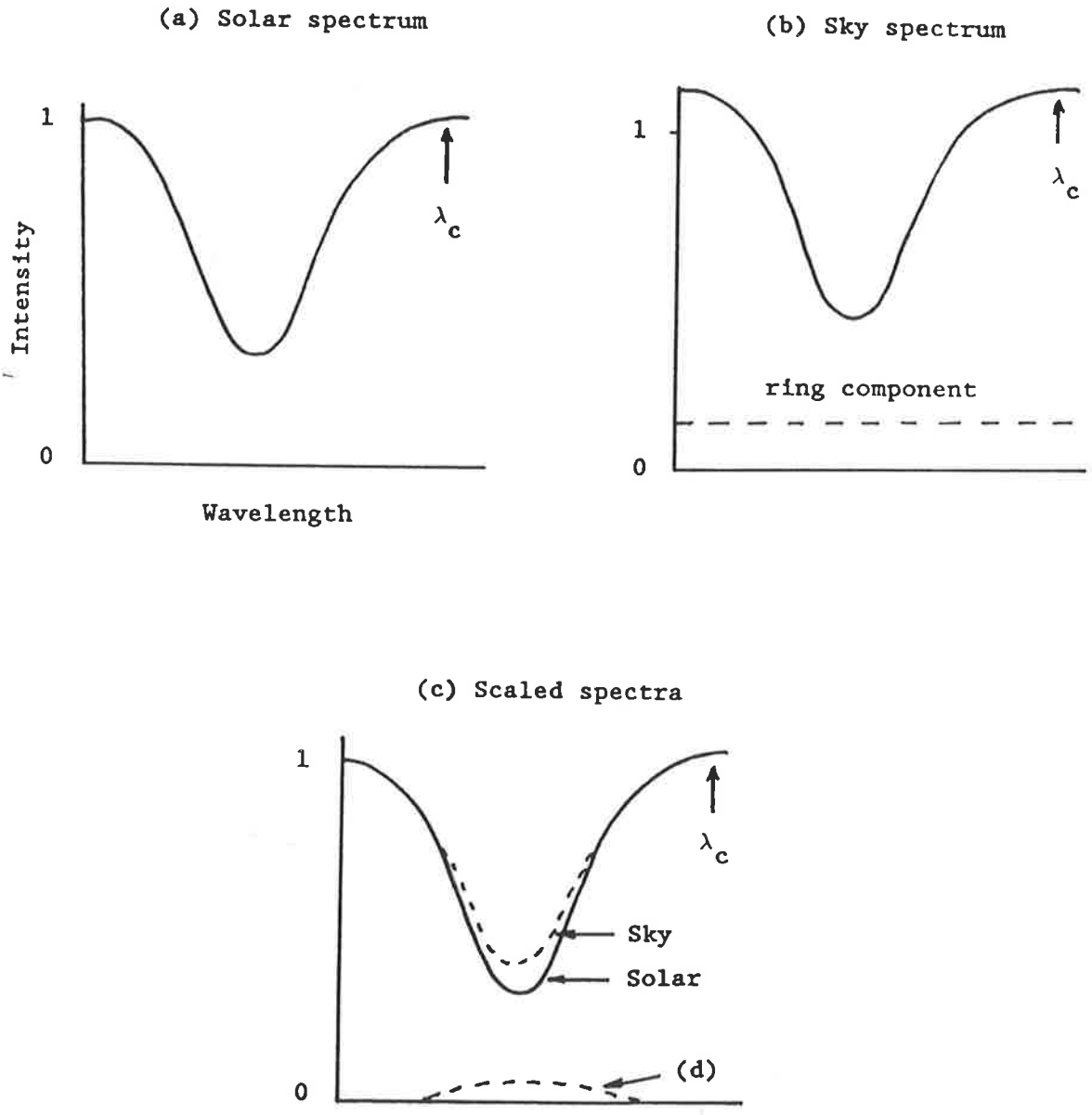

Figure 3.4 The Ring effect. The sky spectrum in the region of a Fraunhofer line is illustrated in (b) and has a fraction of its continuum value added as a grey spectrum. Upon normalising the solar spectrum (a) at a wavelength λ_c, the sky Fraunhofer line is relatively less deep than the solar line (c) resulting in a positive feature upon subtraction (d).

variability over time scales ranging from hours to days.

The first high-resolution experiment to isolate the λ630nm emission was performed by Bens et al. (1965). Spectra of the day sky and of direct sunlight were obtained using two Fabry-Perot interferometers and an interference filter in series. The emission line was obtained upon normalisation and subtraction of the spectra. Emission intensities of 6 to 50kR and a temperature determination of 1700±750K were reported.

Further temperature determinations were reported by Barmore (1972) who employed three Fabry-Perot interferometers in series to isolate the emission. The analysis procedure yielded estimates of emission intensity, temperature and ring component (Barmore 1975).

In 1972 the Mawson Institute for Antarctic Research installed a 150mm aperture Fabry-Perot spectrometer at Mount Torrens (33.9^{o}S, 139.0^{o}E). This instrument, designed for high-resolution observations of the nightglow, was subsequently adapted to dayglow observations by adding a second Fabry-Perot etalon (Cocks et al. 1980). The first successful determinations of Doppler shift of the λ630nm dayglow were obtained from this instrument in 1976 (Cocks 1977; Cocks and Jacka 1979).

The instrument used in this study is an improved version of the above and was installed at Mawson, Antarctica in 1980.

3.5 Interpretation of the Measurements

The temperature derived from equation 3.2 is representative of the bulk neutral temperature only if the emitting species and the dominant neutral species are in equilibrium. The mean time between collisions in the region of λ630nm emission is small (~1s) compared to the $O(^1D)$ radiative lifetime (~110s). The $O(^1D)$ atoms therefore have sufficient

time to become thermalised and the derived Doppler temperature is a good measure of the bulk neutral temperature at all heights within the emitting region.

At mid and low latitudes during quiet geomagnetic conditions the Fabry-Perot measurements correspond to a height range of about 180 to 280 km. Gradients of temperature and wind velocity are generally small within this region and the derived temperature is very nearly that of the exosphere (Roble et al. 1968; Hernandez et al. 1975).

The interpretation of measurements made in the auroral zone during disturbed conditions is less straightforward. The emitting layer is broader and extends down to altitudes where the temperature gradient becomes significant. Under such conditions the shape of the recorded emission line is no longer Gaussian and a single temperature cannot be assigned. This is often the case if the spectrometer is viewing a bright auroral feature. Careful checking of the recorded line shape is necessary in order to identify and eliminate records which have been contaminated in this manner.

Chapter 4

THEORY OF THE FABRY-PEROT INTERFEROMETER

4.1 Introduction

The basic theory of the single etalon Fabry-Perot interferometer (FPI) may be found in standard optics texts (Born and Wolf 1970; Jenkins and White 1981) and has been extended by several authors (Chabbal 1953,1958; Jacquinot 1954,1960; Hill 1963; Ballik 1966; Hernandez 1966,1970). Wilksch (1975,1985) has presented a restatement of the theory in which the order of interference rather than the wavenumber is used as the independent variable. Hernandez (1978) has investigated noise limitations on the retrieval of emission line parameters and has defined optimum conditions for the determination of Doppler widths and shifts of emission lines (Hernandez 1979,1982). Section 4.3 presents an outline of single etalon theory based upon the above works.

The theoretical description of the polyetalon FPI is complex and is as yet incomplete. Certain aspects of polyetalon theory and design have been treated by a number of authors Chabbal (1958), Mack et al. (1963), McNutt (1965), Stoner (1966), Roesler and Mack (1967), Roesler (1968,1974) and Daehler and Roesler (1968). Cocks (1977) has presented a detailed description of a dual FPI and has described the principal considerations in the design of a polyetalon system. A brief introduction to dual-etalon theory is presented in section 4.4.

4.2 Source Function, Instrument Transmission and Recorded Spectrum

The spectral source to be investigated may be described by a source function $B(\lambda)$ defined as the source radiance per unit wavelength interval and having units of photons.m^{-2}.s^{-1}.sr^{-1}.(wavelength)$^{-1}$. The spectrometer is described by the instrument transmission function defined as the spectrometer transmittance as a function of wavelength. The instrument transmission function will be denoted $I(\lambda-\lambda_0)$ where λ_0 is some reference wavelength. The function $I(\lambda-\lambda_0)$ may consist of a single peak or in the case of the FPI, a series of peaks.

The spectral structure of the source function is examined by varying some instrument parameter such that the transmission function is 'swept' across the wavelength region of interest; i.e. by varying λ_0. At each value of λ_0, the transmitted radiation reaching the detector is converted to a signal proportional to the flux. This signal is recorded as a function of λ_0.

In the subsequent discussion the following assumptions are made:

i) the transmission function does not change shape over a scan

ii) the source has a uniform surface radiance within the spectrometer field of view.

With the spectrometer tuned to λ_0 the flux transmitted in the wavelength region λ to $\lambda+d\lambda$ is

$$d\Phi(\lambda_0) = S\Omega I(\lambda-\lambda_0)B(\lambda)d\lambda \qquad (4.1)$$

where S is the area of the spectrometer entrance pupil and Ω is the spectrometer field of view in steradians.

The total flux transmitted by the spectrometer at λ_0 is obtained by integrating 4.1

$$\Phi(\lambda_0) = S\Omega \int_{-\infty}^{\infty} I(\lambda-\lambda_0)B(\lambda)d\lambda \qquad (4.2)$$

We define the recorded function $Y(\lambda_0) = \Phi(\lambda_0)/S\Omega$ and obtain the equation

$$Y(\lambda) = I(\lambda) \cap B(\lambda) \qquad (4.3)$$

where the symbol $\cap$ denotes the cross-correlation operation. Equation (4.3) may be alternatively expressed as

$$Y(\lambda) = R(\lambda) * B(\lambda) \qquad (4.4)$$

where * denotes the convolution operation and $R(\lambda) = I(-\lambda)$ describes the instrument's response to a monochromatic source. $R(\lambda)$ is called the instrument response function or simply the 'instrument function'.

4.3 Theory of the Single Etalon FPI

4.3.1 The Ideal Fabry-Perot Etalon

The ideal Fabry-Perot etalon consists of a pair of flat, parallel, transparent plates, the inside surfaces of which are coated with partially reflecting mirrors of reflectance R and transmittance T. Figure 4.1 shows the basic configuration: light from an extended source undergoes multiple reflections between the Fabry-Perot plates, resulting in a series of transmitted and reflected rays. The transmitted rays are collected by a lens and real, circular Fabry-Perot fringes are formed at the focal plane. An aperture centred on the focal point of the lens allows a portion of the fringe pattern to

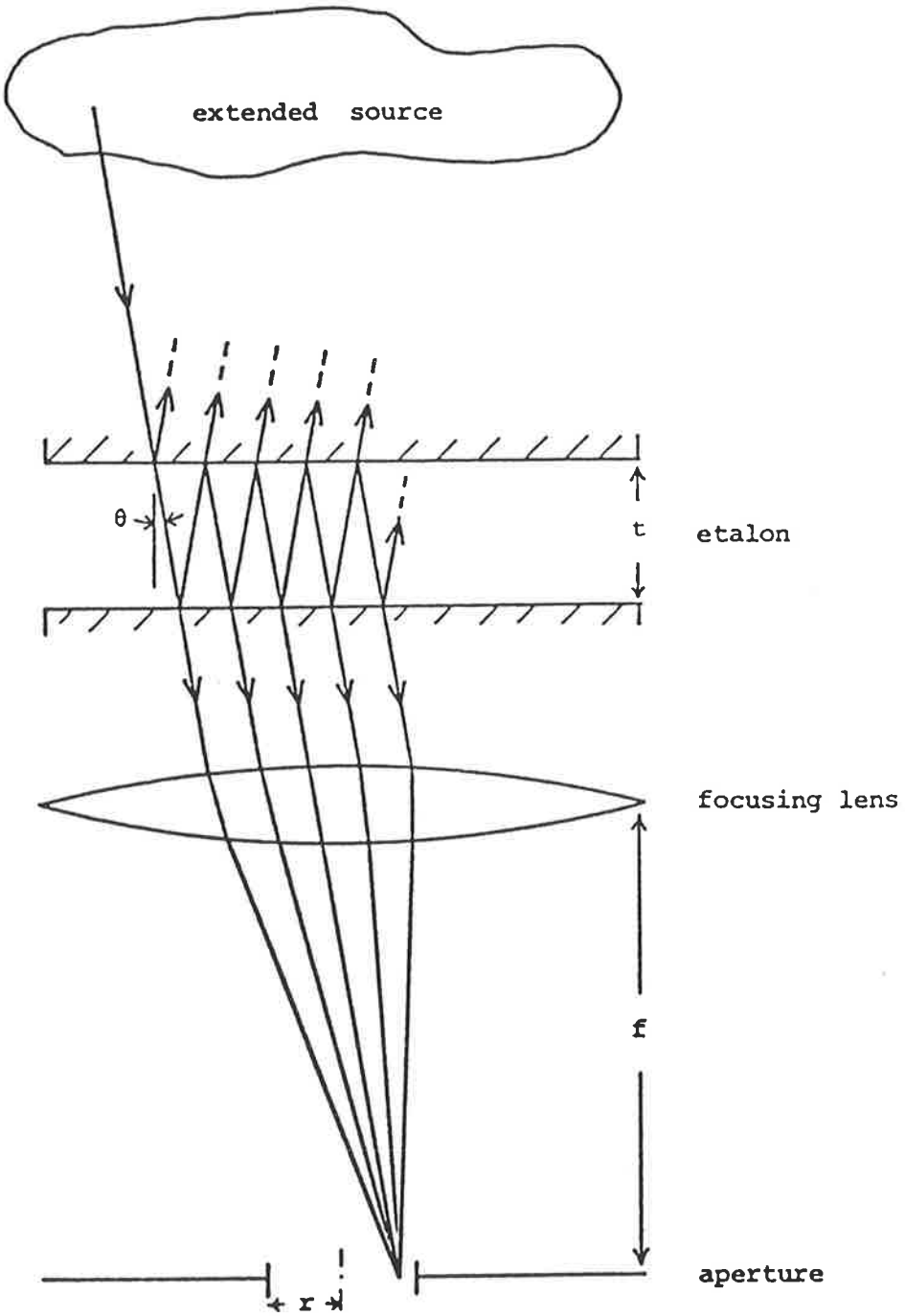

Figure 4.1 Principle of the Fabry-Perot etalon

be transmitted to a detector. If a photomultiplier is used only the central fringe may be recorded. The use of an imaging detector at the focal plane allows several fringes to be recorded with a corresponding gain in luminosity over the conventional arrangement.

The transmission of the ideal etalon is described by the Airy function

$$A(\lambda) = \frac{\tau_A}{1 + \frac{4R}{(1-R)^2} \sin^2\left(\frac{2\mu t \xi \pi}{\lambda} + \phi\right)} \qquad (4.5)$$

where t is the separation of the Fabry-Perot plates,

λ is the vacuum wavelength of the radiation,

μ is the refractive index of the medium between the plates,

τ_A is the combined transmittance of the plates and reflective coatings,

ϕ is the phase change on reflection at the plate surfaces,

and $\xi = \cos\theta$ where θ is the angle between the plate normal and the rays within the spacer medium.

(In the following discussion the phase change ϕ will be assumed to be incorporated in an adjusted value of t.)

Constructive interference occurs when the order of interference m is integral:

$$m = 2\mu t \xi / \lambda \qquad (4.6)$$

The spectrometer may be scanned in wavelength by varying either μ (refractive index or pressure scanning), t (separation scanning) or ξ (spatial scanning).

For a given μ,t and ξ the transmission function consists of a series of peaks (Figure 4.2). The spacing of adjacent peaks is called the free spectral range $\Delta\lambda$ and is given by

$$\Delta\lambda = \lambda/m \tag{4.7}$$

The full width at half-maximum of the peaks is denoted $\delta_A\lambda$. (Note: the full width at half-maximum of any function will henceforth be termed the 'width'). The ratio of $\Delta\lambda$ to $\delta_A\lambda$ is called the reflective finesse N_A. For $R > 0.5$ (which is always true in practice) this is given to good approximation by

$$N_A \simeq \frac{\pi\sqrt{R}}{(1-R)} \tag{4.8}$$

N_A may be interpreted as the number of resolvable lines within one free spectral range. In general, R and hence N_A are functions of λ; they may however be considered as constants over the small range of wavelengths scanned.

4.3.2 Effect of plate defects

The transmission function is modified by variations in the effective separation of the plates over the face of the etalon. These variations may be caused by imperfections in plate flatness and parallel alignment and by non-uniformity of the reflective coatings. Chabbal (1953) has shown that an etalon operating near normal incidence may be treated as a juxtaposition of elementary etalons of different separations. The fractional area ds/S of the elementary etalon with separation between t+x and t+x+dx is given by

$$ds/S = D_1(x)dx \tag{4.9}$$

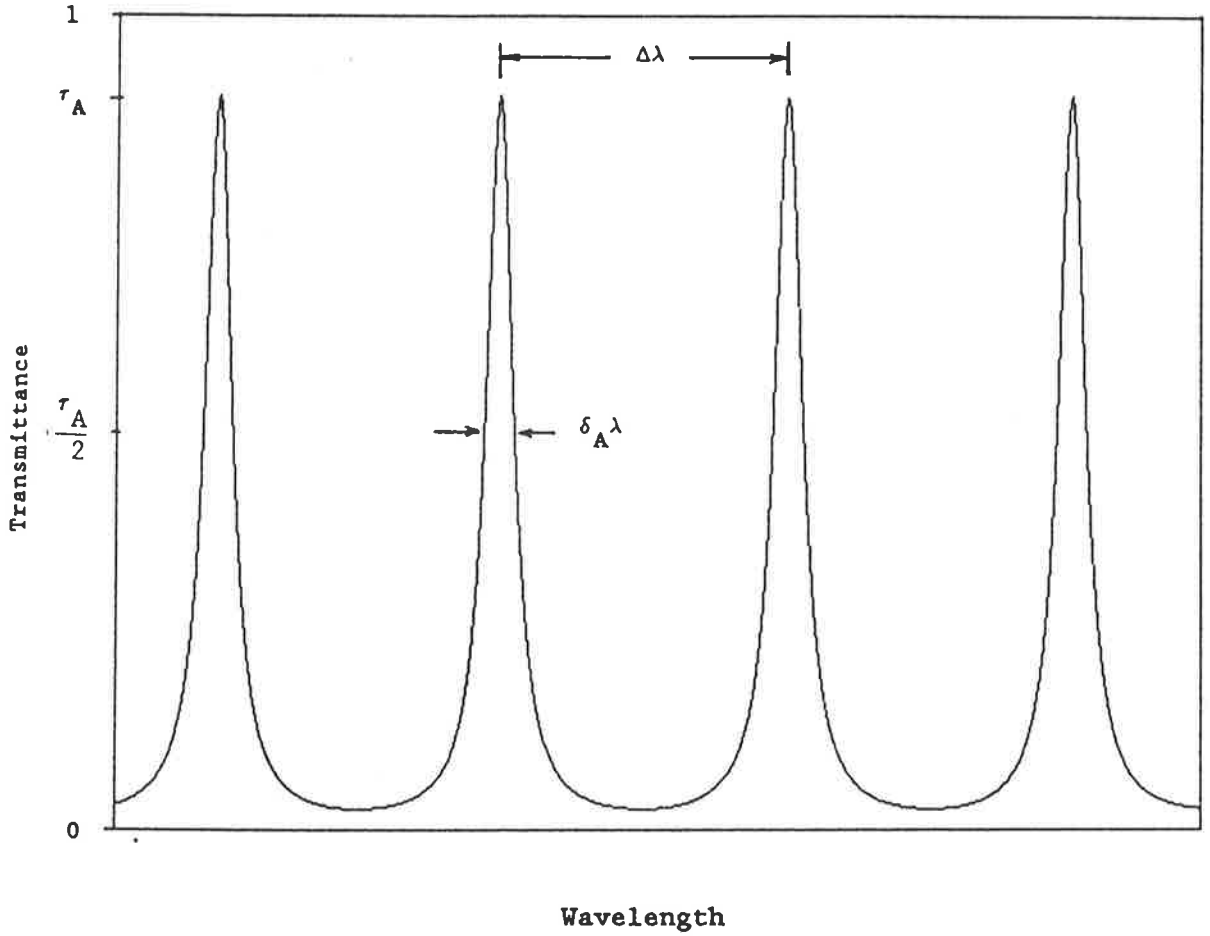

Figure 4.2 The Airy function plotted over several orders.

where $D_1(x)$ is the normalised defect function describing the distribution of plate defects. (Note that the symbol t will henceforth refer to the mean separation of the plates.)

We consider wavelengths in the vicinity of some reference wavelength λ_0. The transmittance of λ' by the elementary etalon of separation t is given by equation 4.5 and is illustrated in Figure 4.3. For an etalon of separation t+x (x>0 say) the transmission maximum of order m_0 shifts to a higher wavelength. The transmittance of λ' at separation t+x is equal to the transmittance of $\lambda'-\lambda_x$ at separation t. The quantities λ_x and x are related by equation 4.6 which yields

$$\lambda_x = x\lambda'/t \tag{4.10}$$

where we have assumed $x \ll t$ which is always true in practice. The elementary etalon of separation t+x contributes an amount $dE_{\lambda'}$ to the transmittance of λ' by the entire etalon, where

$$dE_{\lambda'} = A(\lambda'-\lambda_x)D_1(x)dx \tag{4.11}$$

We introduce a new version of the defect function, $D(\lambda_x)$, given by

$$D(\lambda_x) = \frac{1}{S}\frac{ds}{d\lambda_x} \tag{4.12}$$

This new defect function is related to the old one by

$$D(\lambda_x) = \frac{t}{\lambda'} D_1\left(\frac{t}{\lambda'}.\lambda_x\right) \tag{4.13}$$

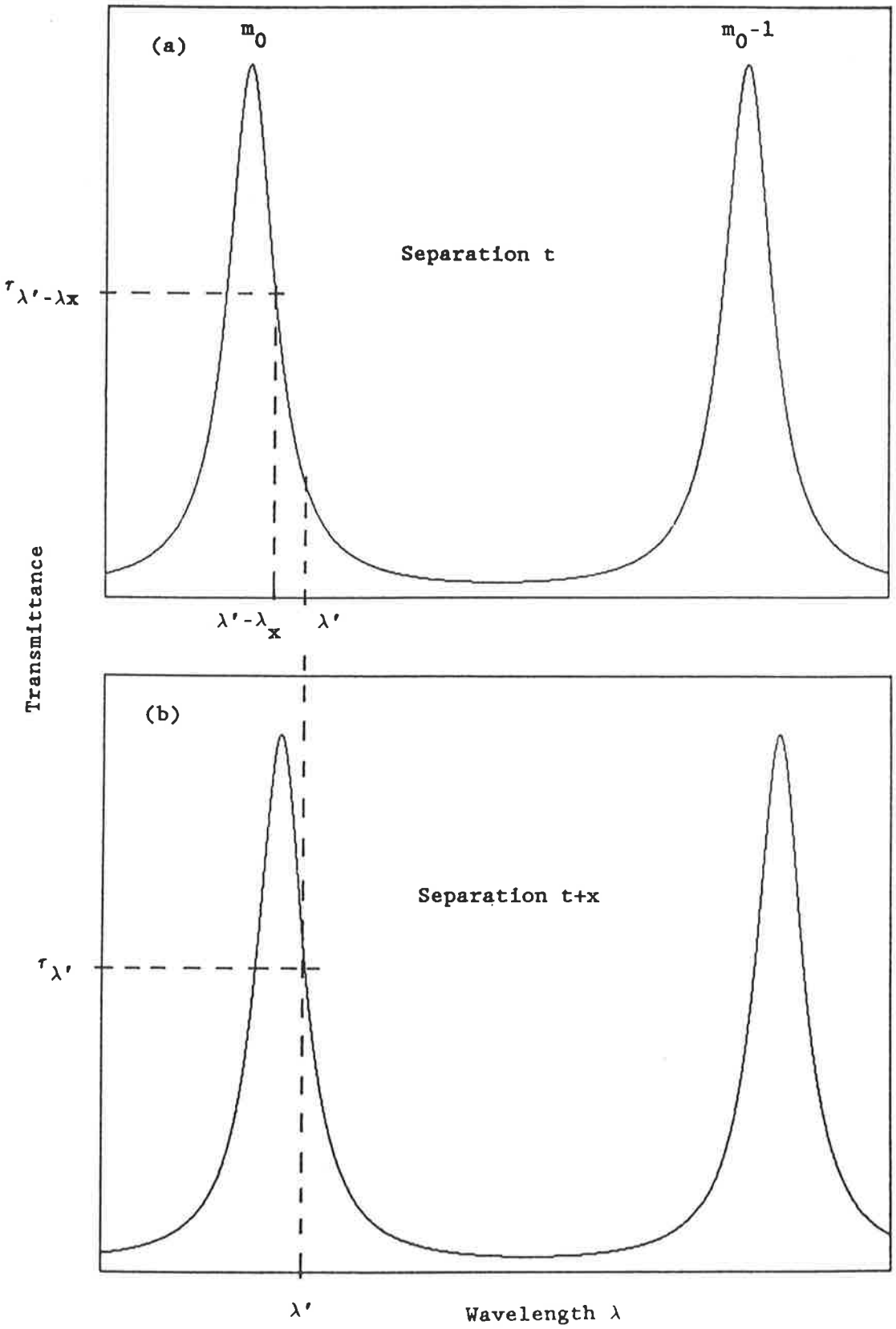

Figure 4.3 (a) The instrument function over orders m_0 and m_0-1 for a separation t. (b) At separation t+x (x>0), the orders m_0 and m_0-1 transmit at longer wavelengths.
The transmittance of λ' in (b) is equal to the transmittance of $\lambda'-\lambda_x$ in (a).

Since we are only considering small variations about λ_0 we may replace λ by λ_0 in the above expression which becomes

$$D(\lambda_x) = \frac{t}{\lambda_0} D_1\left[\frac{t}{\lambda_0}.\lambda_x\right] \qquad (4.14)$$

It is important to realise that the form of $D(\lambda_x)$ depends on λ_0, the wavelength region of interest. We rewrite 4.11 as

$$dE_{\lambda'} = A(\lambda'-\lambda_x)D(\lambda_x)d\lambda_x \qquad (4.15)$$

and integrate to obtain

$$E(\lambda) = A(\lambda) * D(\lambda) \qquad (4.16)$$

where the symbol * denotes the convolution operation.

$E(\lambda)$ is called the etalon function and describes the transmission of an etalon in the presence of plate defects. It is the convolution of the Airy function $A(\lambda)$ with a defect function $D(\lambda)$ whose form depends on the wavelength region of interest.

If the function $D_1(x)$ has a width δx (the scale size of the defects) then the width of $D(\lambda)$ is

$$\delta_D\lambda = \lambda_0\delta x/t \qquad (4.17)$$

and the defect finesse N_D is defined as

$$N_D = \Delta\lambda/\delta_D\lambda \qquad (4.18)$$

The width of the etalon function is denoted $\delta_E\lambda$ and is greater than both $\delta_A\lambda$ and $\delta_D\lambda$. The etalon finesse is defined as

$$N_E = \Delta\lambda/\delta_E\lambda \tag{4.19}$$

The areas of $A(\lambda)$ and $E(\lambda)$ will be equal since $D(\lambda)$ is normalised to unit area. The peak transmittance τ_E of $E(\lambda)$ is less than τ_A as a result of the broadening produced by the convolution operation. We may write $\tau_E = \tau_D \cdot \tau_A$ where τ_D is some fraction determined by the shapes of $A(\lambda)$ and $D(\lambda)$.

4.3.3 Effect of Finite Aperture

The discussion so far has considered radiation incident at a single value of ξ. In practice the instrument must employ a finite aperture and hence a finite range of ξ, leading to further modification of the transmission function.

We consider the full aperture to be divided into elementary apertures with different values of incidence. The elementary aperture admitting rays with incidence in the range $\xi+\xi_f$ to $\xi+\xi_f+d\xi_f$ subtends a solid angle $d\omega$ at the lens given by

$$d\omega/\Omega = F_1(\xi_f)d\xi_f \tag{4.20}$$

where Ω is the solid angle subtended by the complete aperture and $F_1(\xi_f)$ is the normalised aperture function. For the case of a circular aperture of radius r, centred on the optical axis, it is easily shown that

$$d\omega = 2\pi d\xi_f \tag{4.21}$$

and if we put ξ_f=0 when ξ=1, we obtain

$$F_1(\xi_f) = 2\pi \qquad -\delta\xi \leq \xi_f \leq 0 \qquad (4.22)$$
$$= 0 \qquad \text{otherwise}$$

where $\delta\xi$ is the width of $F_1(\xi_f)$. In this case $\delta\xi \approx 1/2(r/f)^2$ and $\Omega = 2\pi\delta\xi$ where f is the focal length of the lens (f>>r).

The analysis proceeds in a manner analogous to the previous section. We consider wavelengths in the vicinity of some reference λ_0. The transmittance of λ' at incidence $\xi+\xi_f$ is equal to the transmittance of $\lambda'-\lambda_\xi$ at incidence ξ where

$$\lambda_\xi = \xi_f\lambda'/\xi \qquad (4.23)$$

The elementary aperture with incidence $\xi+\xi_f$ contributes an amount $dI_{\lambda'}$ to the transmittance of λ' by the entire aperture where

$$dI_{\lambda'} = E(\lambda'-\lambda_\xi)F_1(\xi)d\xi \qquad (4.24)$$

We introduce a new aperture function $F(\lambda_\xi)$, given by

$$F(\lambda_\xi) = (1/\Omega)d\omega/d\lambda_\xi \qquad (4.25)$$

This new aperture function is related to the old one by

$$F(\lambda_\xi) = \frac{\xi}{\lambda_0}F_1\left[\frac{\xi}{\lambda_0}.\lambda_\xi\right] \qquad (4.26)$$

Figure 4.4 illustrates the functions $F_1(\xi_f)$ and $F(\lambda_\xi)$ for the case of a circular aperture centred on the optical axis.

Equation (4.24) may now be rewritten as

$$dI_{\lambda'} = E(\lambda'-\lambda_\xi)F(\lambda_\xi)d\lambda_\xi \qquad (4.27)$$

We integrate and obtain

$$I(\lambda) = E(\lambda) * F(\lambda) \qquad (4.28)$$

$I(\lambda)$ is the instrument transmission function. It describes the transmission of an interferometer with imperfect etalon and finite aperture. It is the convolution of the etalon function $E(\lambda)$ with the aperture function $F(\lambda)$.

If the width of $F_1(\xi)$ is $\delta\xi$ then the width of $F(\lambda)$ is

$$\delta_F\lambda = \lambda_0\delta\xi \qquad (4.29)$$

where we have taken ξ=1. The aperture finesse N_F is defined as

$$N_F = \Delta\lambda/\delta_F\lambda \qquad (4.30)$$

The width of $I(\lambda)$ is denoted $\delta_I\lambda$ and is greater than both $\delta_E\lambda$ and $\delta_F\lambda$. The instrument finesse is defined as

$$N_I = \Delta\lambda/\delta_I\lambda \qquad (4.31)$$

The peak transmittance τ_I of $I(\lambda)$ will be less than that of τ_E and we may write $\tau_I = \tau_F.\tau_E$ where τ_F is some fraction determined by the shapes of $E(\lambda)$ and $F(\lambda)$.

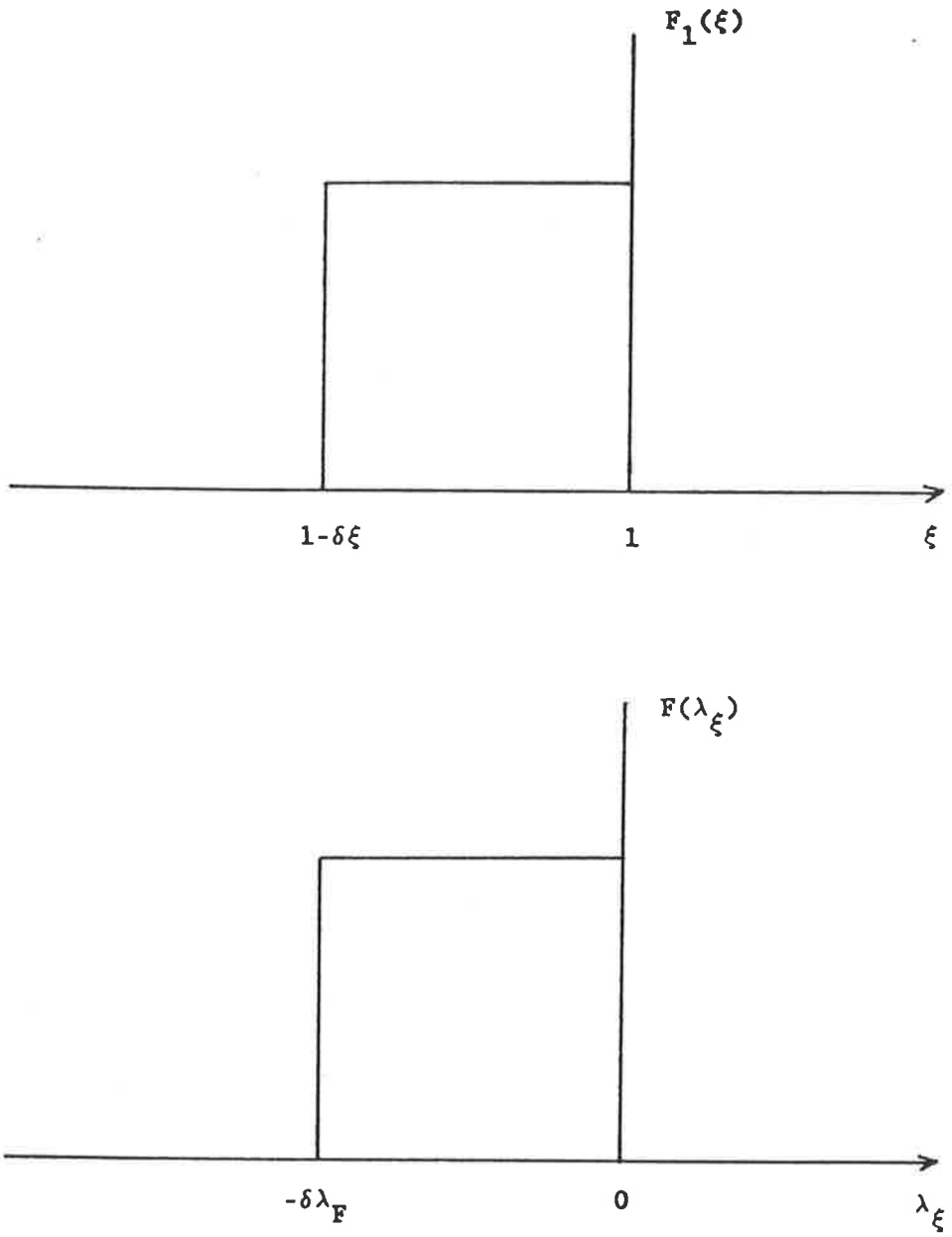

Figure 4.4 The aperture function in terms of the cosine of the angle of incidence (ξ) and the wavelength.

4.3.4 Transmitted Flux

Recalling equations (4.3),(4.16) and (4.28), the flux transmitted by the instrument is

$$\Phi(\lambda) = S\Omega\tau_c[I(\lambda) \cap B(\lambda)]$$
$$= S\Omega\tau_c[A(\lambda) * D(\lambda) * F(\lambda)] \cap B(\lambda) \qquad (4.32)$$

where we have introduced a transmission coefficient τ_c which describes the effect of absorptions and reflections caused by the various optical components. The maximum flux is given by

$$\Phi_{max} = S\Omega\tau_c\tau_A\tau_D\tau_F B_{max} \qquad (4.33)$$

4.3.5 Optimisation of Operating Parameters

In most applications the main objective is to achieve adequate spectral resolution whilst maximising the transmitted flux Φ. A rough guide which is commonly used is to set the instrument width $\delta_I\lambda$ equal to the source width $\delta_B\lambda$ and then to maximise Φ.

Equation (4.33) shows that the maximum flux is proportional to the product $\Omega\tau_F$. Chabbal (1953) has examined this quantity as a function of the ratio $\delta_F\lambda/\delta_E\lambda$ and has shown that a broad maximum exists near $\delta_F\lambda/\delta_E\lambda = 1$. The aperture size which optimises Φ is therefore that which results in an aperture function width approximately equal to the etalon width. Under such conditions, both of these widths will be somewhat less than the instrument width, typically by a factor of about 0.7.

The defect width $\delta_D\lambda$ places a lower limit on the achievable etalon width $\delta_E\lambda$; also if $\delta_D\lambda$ is much larger than $\delta_A\lambda$ the transmission factor τ_D is greatly reduced. It is advisable therefore to have $\delta_D\lambda \ll \delta_A\lambda$ whence $\delta_E\lambda$ will approximately equal $\delta_A\lambda$. The required reflectance may then be determined from (4.8). The instrument function width should be made no smaller than necessary for the application since the requirements on plate coatings, flatness and parallel alignment become more severe as $\delta_D\lambda$ is decreased.

4.3.6 Recorded Profile

In the Mawson spectrometer the transmitted flux is detected by a photomultiplier tube whose output is recorded as a function of the etalon plate separation. Photons arriving at the photocathode produce photoelectrons with a quantum efficiency Q. Electron multiplication occurs within the tube and a current pulse is produced at the anode. When the source radiance is low, as is the case for night observing, the pulses are amplified and counted directly by the data acquisition system.

The spectrometer is scanned by 'stepping' the plate separation through N (usually 128) values. Since the scan is restricted to less than one order we may associate with each plate separation t_n a wavelength λ_n. The index n also functions as the channel address for the data acquisition system. A line profile is recorded by scanning repetitively across the region of interest and summing successive scans. Repetitive scanning is necessary to reduce distortion caused by noise and by variations in source intensity.

With the spectrometer in the nth channel the flux incident on the photocathode is $\Phi(\lambda_n)$ photons.s^{-1}. The average pulse rate due to the

source is $Q\Phi(\lambda_n)$ and if the total time spent acquiring in each channel is t_d then the counts recorded are given by

$$y_n = t_d Q\Phi(\lambda_n) + b + z_n \qquad (4.34)$$

where b is a background term, independent of channel, which includes contributions from continuum radiation and photomultiplier dark current and z_n is a noise term which embodies the statistical fluctuations in the photon counting process. The results of the aquisition are therefore described by the set of numbers $\{y_n\}$.

4.4 The Dual-Etalon FPI

It has been shown that the single etalon FPI has a transmission function consisting of a series of maxima separated in wavelength by a quantity called the free spectral range. If radiation exists outside the free spectral range of interest and the FPI is scanned over one order, interpretation of the recorded spectrum is ambiguous. One requires therefore that information be derived from one bandpass only of the spectrometer. In order to achieve this the sidebands must be suppressed. For observations of isolated spectral lines in the night airglow and aurora, an interference filter usually suffices for this purpose, even though the bandpass of such a filter may be ten or more times the free spectral range of the FPI. For daytime observations a single bandpass must be isolated and this is achieved by placing two (or more) FPI's in series. To isolate a bandpass at wavelength λ_0, the etalons are all tuned for maximum transmission at this wavelength, but the separation of each etalon is chosen such that the respective sidebands occur at different wavelengths. The resulting transmission profile is approximately the product of the

individual profiles and there is a large reduction in peak transmission at wavelengths where the sidebands are not in coincidence. Exact or near coincidences will inevitably occur at some wavelengths but the system is designed such that these are sufficiently removed from the principal bandpass to be suppressed by the interference filter. The mathematical development of dual-etalon theory may be found in the references cited in section 4.1.

Chapter 5

THE FABRY-PEROT SPECTROMETER AT MAWSON

5.1 Introduction

The instrument used in this study is a dual, separation-scanned Fabry-Perot spectrometer in which the central fringe only is recorded. It was designed for high-resolution studies of the airglow and aurora over a wide range of wavelengths during night and day. The instrument is a development of that described by Jacka et al. (1980) and Cocks et al. (1980). Installation at Mawson was completed in 1980 and the instrument has been operated on a regular basis since 1981. A description of the spectrometer follows.

5.2 Optical Layout

The optical system is shown in Figure 5.1. Light enters the instrument via a periscope mounted on the roof of the observatory and controlled from the operator's console. The periscope is driven in steps of 0.1 degrees in zenith and 1 degree in azimuth by microprocessor controlled stepping motors and may be directed towards any part of the sky. A simple telescope on an equatorial mount is used to introduce sunlight for daytime observations.

Because of the very high roof (~4m), an optical relay is incorporated between the periscope and the spectrometer cabinet below. A mechanism allowing the introduction of various light sources for calibration purposes is located within the relay at a magnified image of the field stop.

The Fabry-Perot etalons and detector optics are suspended from a steel frame within an insulated, temperature controlled cabinet. The

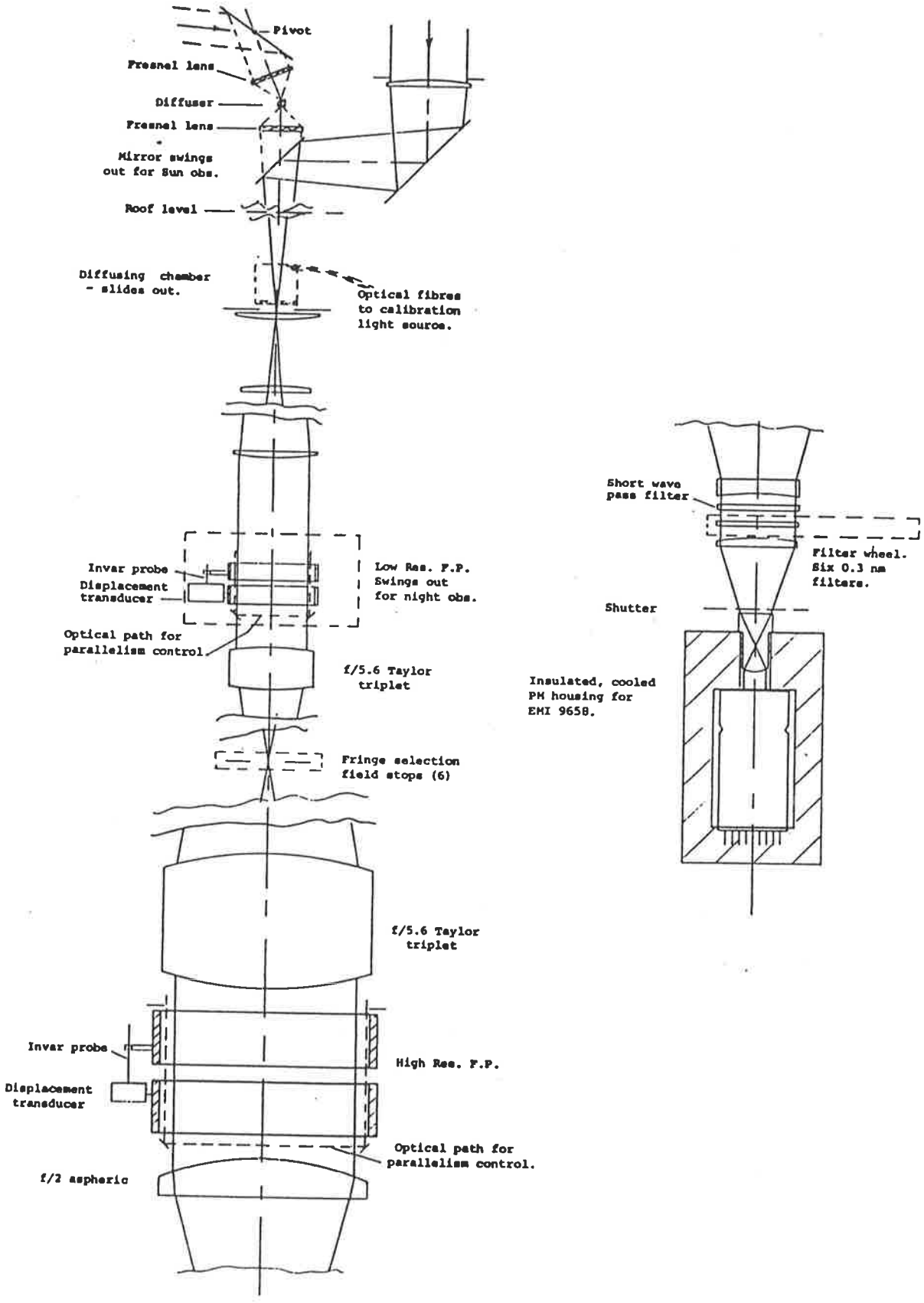

Figure 5.1 Optical system of the Mawson Fabry-Perot spectrometer

support frame is mounted on a concrete block connected to solid rock below and mechanically isolated from the observatory. There is no mechanical coupling to the optical relay above.

For daytime observing, collimated light from the optical relay is filtered by the low-resolution etalon and is focused onto a field stop by an f/5.6 Taylor triplet. For night observing the low-resolution etalon is swung out of the optical path by a motor and a blank tube inserted. A Geneva mechanism enables any of six field stops to be used, giving a field of view variable from 0.2 to 1 degree.
Light diverging from the field stop is collimated by a second f/5.6 Taylor triplet and filtered by the high-resolution etalon which forms the aperture stop of the system.

Up to six interference filters of ~0.3nm bandwidth are carried in a wheel above the photomultiplier housing. A short-wave pass filter is used to eliminate light scattered from the parallelism control systems.
The instrument is designed so that all routine operations may be performed externally from the operator's console. In practice it is possible to run the spectrometer for many weeks without opening the insulated cabinet, thus minimising thermal and mechanical perturbations.

5.3 Fabry-Perot Etalons

The two etalons are of similar construction with 50mm and 150mm diameter plates used in the low and high resolution etalons respectively. The plates are of fused silica and coatings are the 13-layer all-dielectric type described by Netterfield et al. (1980). The reflective finesse after ageing was N_A~27 at λ546nm and N_A~33 at λ633nm. Defect finesse in operation is N_D~35 for the high resolution etalon and N_D~60 for the low resolution etalon.

Fine control of plate separation and parallelism is provided by PZT 5H piezoelectric tubes polarised radially. The tubes have a piezoelectric expansion coefficient of ~1nm/V. The plates may be scanned over a maximum range of ~700nm (~2 orders of the $O(^1D)$ λ630nm emission). Large variations in plate separation are achieved by means of three steel support screws driven by stepping motors and controlled from the operator's console. The maximum plate separation is 25mm for the high resolution etalon and 5mm for the low resolution etalon.

5.4 Parallelism Control

It is required that the plates of the Fabry-Perot etalons be maintained parallel to a degree somewhat better than the plate defect. Servo-control of plate parallelism is applied to both etalons using the method of Ramsay (1962). In this scheme, a collimated beam of near-infrared light is passed down through the etalon space on one side and up through the opposite side to a PIN diode (Figure 5.2). When the paths AB=CD, the spectra resulting from each pass through the etalon space are identical and the detected signal is a maximum. In order to sense the direction of parallelism error a small amplitude (~3nm) 'wobble' of 1kHz is applied to one plate. The PIN diode output is amplified, filtered and fed to phase-sensitive circuitry, the output of which controls the plate parallelism through a negative feedback loop. The control scheme is applied across two orthogonal diameters in such a way that the mean separation remains constant.

5.5 Separation Control

In order to measure the small Doppler shifts resulting from thermospheric winds it is essential that long-term stability and linearity of the scan be maintained. Drifts in etalon separation due

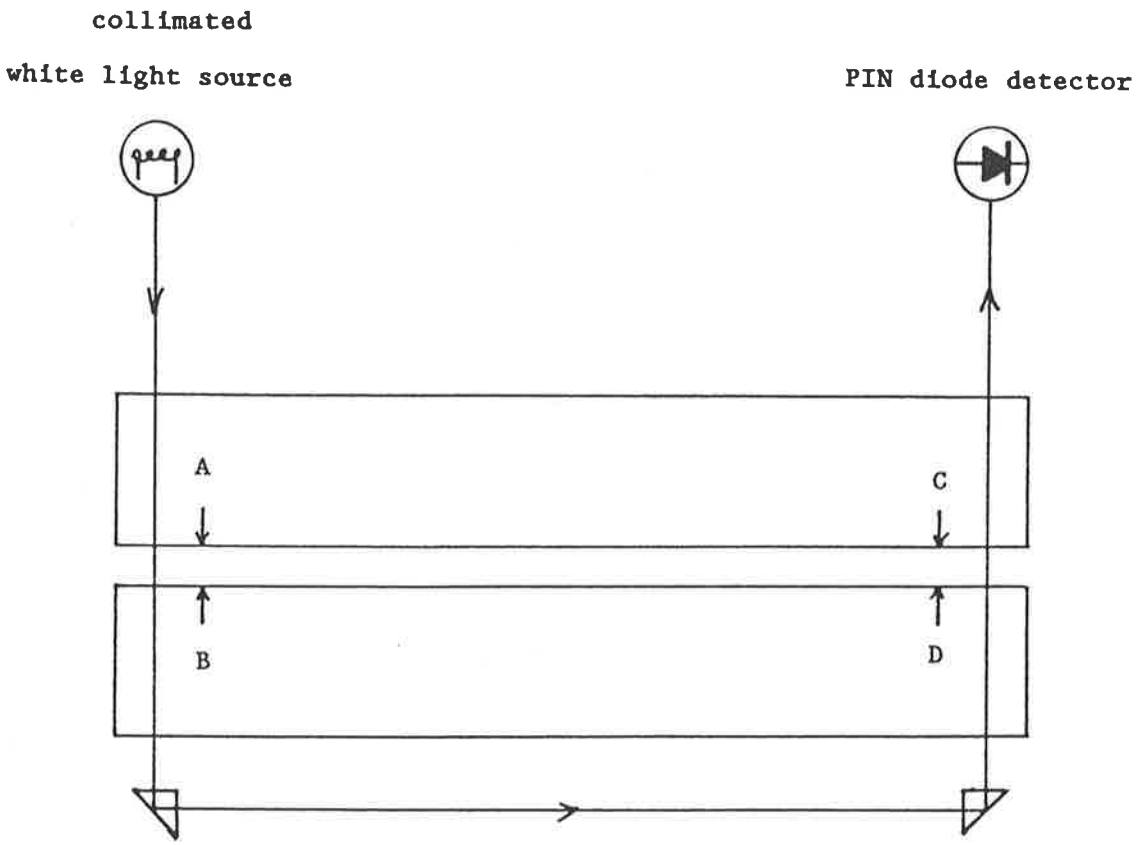

Figure 5.2 Parallelism control system schematic.

to temperature variations, together with the non-linearities, hysteresis and creep associated with piezoelectric materials require that the etalon be scanned under servo-control.

Variations in the geometrical separation of the plates are sensed by a capacitor displacement transducer, the output of which is compared with a staircase scan waveform. A pressure transducer within the etalon chamber provides a correction signal to compensate for barometric changes in the refractive index of the air between the plates.

The capacitor displacement transducer was designed and constructed at the Mawson Institute for Antarctic Research.It comprises 2 sets of stainless steel discs configured to form 4 parallel-plate, air-spaced capacitors (Figure 5.3). One set of discs is attached to the lower Fabry-Perot plate holder while the other movable set is connected to the upper plate holder via an invar probe. The four capacitors are connected in a bridge formation and a 10kHz signal is applied. The bridge may be balanced by adjusting the position of the probe by means of a motor drive. Any displacement of the plates causes an unbalance of the bridge. The amplitude and phase of the output signal indicate the magnitude and direction of displacement. Phase-sensitive circuitry is used to produce a dc voltage which is proportional to the displacement of the plates from some arbitrary zero. This signal is combined with the barometric correction, a manual offset and the scan waveform to produce an error signal which controls the voltage applied to the piezoelectric tubes. The optical separation of the plates is therefore controlled precisely by the scan waveform.

(a)

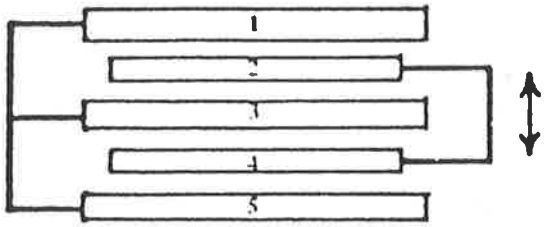

(b)

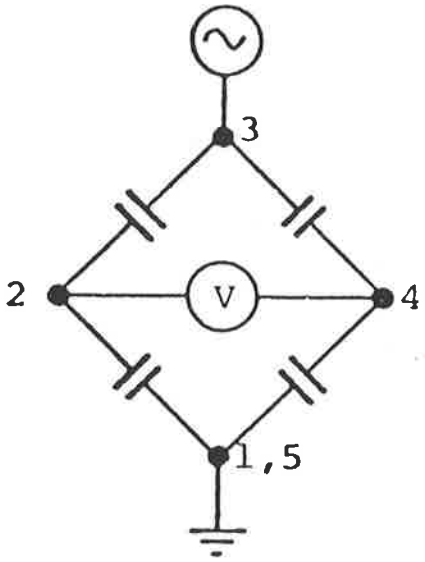

Figure 5.3 Capacitive displacement transducer. (a) Schematic of mechanical arrangement, (b) electrical connection of the discs.

5.6 Photon Detection

An EMI 9658A photomultiplier with an S20 photocathode is used. The photocathode is deposited on a multipyramidal form impressed on the inside surface of the front window; this enhances the effective quantum efficiency. A Peltier junction device is used to cool the photomultiplier to -30C. Dark counts are further reduced to $10s^{-1}$ by the technique of magnetic defocusing.

Photomultiplier pulse counting is employed for night observing. This is not possible during the daytime as the higher signal levels introduce unacceptable spectral distortion as a result of pulse counting losses. For daytime observing the photomultiplier current is amplified and a voltage-controlled oscillator is used to provide a pulse train for input to the pulse counting circuitry.

5.7 Data Acquisition System

The data acquisition system comprises three microprocessors accessing a common block of memory. The memory consists of 256 channels, each of 24 bits capacity, and may be addressed in two separate blocks of 128 channels to permit the acquisition of two distinct spectra as required for daytime observations.

One processor controls the real-time display of data on a CRO screen, one controls the recording of data on cassette tape and the third controls the acquisition of data, involving pulse counting, generation of the scan waveform and overall coordination of the observing program.

A variety of observing programs is provided. In the simplest configuration a single spectrum is accumulated in 128 or 256 channels. The instrument is repeatedly scanned over the selected wavelength range until a predetermined number of scans is completed. Acquisition

then ceases and the operator may record the accumulated data or continue further acquisition if the signal to noise ratio is unsatisfactory.

The data are recorded in the form of ASCII characters. In addition to the signal counts, housekeeping data are recorded including periscope zenith and azimuth angles, date, start and stop times, filter number, scan range and speed etc. For daytime observing the instrument alternately accumulates sky and solar spectra which are stored in separate 128-channel blocks of memory.

Chapter 6

DATA ANALYSIS

6.1 Introduction

The Mawson Fabry-Perot spectrometer, when used for night observing, yields raw data in the form of airglow/auroral spectral line profiles. A single profile consists of a set of numbers $\{y_n\}$ which is described by equation (4.34). From this we must determine values of emission intensity, temperature and wind velocity. The analysis may be considered in two stages:

i) The source function $B(\lambda)$ must be recovered from the recorded profile.

ii) The quantities of interest must be determined from the recovered source spectrum. We shall also require estimates of the uncertainties of these determinations.

Recovery of the source function involves removal of the instrument broadening effect by numerical deconvolution. A number of techniques are available; the one used in this work was developed at the Mawson Institute and is described in detail by Wilksch (1975). The following description is based on that work.

The method consists of fitting to the data a numerically generated profile which is the convolution of an appropriate instrument function with a Gaussian curve. The parameters of the Gaussian (peak position, width and height) are varied to find the curve which best fits the data in a least squares sense. An empirically determined version of the instrument function is used, thus removing the need for an analytic representation. The fitting is carried out in the Fourier transform domain, using only those components which are not dominated by noise.

6.2 The Analysis Scheme

Recalling equation (4.34), a line profile is represented by the set of numbers $\{y_n\}$ given by

$$y_n = s_n + b + z_n \tag{6.1}$$

where s_n is the contribution due to the source, b is a constant backgound term and z_n describes the statistical fluctuations in the data. We assume that the expected value of z_n, denoted $\langle z_n \rangle$, is zero and also that the variance $\langle z_n^2 \rangle$ is independent of n. This second assumption is reasonable when the source signal is small compared to the background. We may therefore write

$$\langle y_n \rangle = s_n + b \tag{6.2}$$

The method consists of deriving a number of trial sets $\{s_n\}$, each corresponding to a different combination of emission parameters (intensity, temperature and wind velocity) and a constant b which together give the best fit to the data. The set which best fits the data is taken to be that which minimises the χ^2 parameter defined as

$$\chi^2 = \sum_{n=0}^{N-1} [y_n-(s_n+ b)]^2/\sigma^2 \tag{6.3}$$

$$\text{where} \quad \sigma^2 = \langle z_n^2 \rangle \tag{6.4}$$

Consider now the discrete Fourier transform of the sets $\{y_n\}$ and $\{s_n\}$. The set $\{\tilde{y}_{n'}\}$ is the discrete Fourier transform (DFT) of $\{y_n\}$ if

$$\tilde{y}_{n'} = \sum_{n=0}^{N-1} y_n \exp(-i2\pi nn'/N) \qquad (6.5)$$

We denote this relationship by

$$\{y_n\} \supset \{\tilde{y}_{n'}\} \qquad (6.6)$$

The transform set will in general be complex-valued. We note in particular that if $\{y_n\}$ is real then $\{\tilde{y}_{n'}\}$ will have conjugate symmetry about $n'=N/2$.

The DFT is a linear operation and we may therefore write

$$\{y_n - (s_n + b)\} \supset \{\tilde{y}_{n'} - \tilde{s}_{n'}\} \qquad (6.7)$$

where

$$\{s_n + b\} \supset \{\tilde{s}_{n'}\} \qquad (6.8)$$

The transform of the constant b is non-zero only for $n'=0$ and so $\{\tilde{s}_{n'}\}$ is the same as the transform of $\{s_n\}$ except at $n'=0$ where

$$\tilde{s}_0 = \sum_{n=0}^{N-1} s_n + Nb \qquad (6.9)$$

We note also that if $\{x_n\} \supset \{\tilde{x}_{n'}\}$ then

$$\sum_{n=0}^{N-1} x_n^2 = \sum_{n'=0}^{N-1} |\tilde{x}_{n'}|^2 / N \qquad (6.10)$$

We may therefore write (6.3) as

$$\chi^2 = \frac{1}{N\sigma^2} \sum_{n'=0}^{N-1} |\tilde{y}_{n'} - \tilde{s}_{n'}|^2 \qquad (6.11)$$

The task is therefore to minimise χ^2 by suitable choice of $\{\tilde{s}_{n'}\}$.

Now equations (4.4) and (4.34) show that

$$s_n = S\Omega Q \tau_c t_d (R(\lambda) * B(\lambda)) \tag{6.12}$$

s_n is therefore a sample of some function $S(\lambda)$ which is the convolution of the source function with a function $H(\lambda)$. That is

$$s_n = S(\lambda_n) \tag{6.13}$$

where $$S(\lambda) = H(\lambda) * B(\lambda) \tag{6.14}$$

and $$H(\lambda) = S\Omega Q \tau_c t_d R(\lambda) \tag{6.15}$$

We apply the well-known convolution theorem to (6.14) and, recalling (6.8), (6.9) obtain

$$\begin{aligned} \tilde{s}_{n'} &= \tilde{B}_{n'} \tilde{H}_{n'} \qquad n'=1 \ldots N-1 \\ &= \tilde{B}_0 + Nb \qquad n'=0 \end{aligned} \tag{6.16}$$

where $\{H_n\}$ is assumed to be normalised so that $\tilde{H}_0=1$ and all scaling factors are absorbed into $\{B_n\}$. Equation (6.11) is now written as

$$\chi^2 = (1/N\sigma^2) \left\{ |\tilde{y}_0 - \tilde{B}_0 - Nb|^2 + \sum_{n'=1}^{N-1} |y_{n'} - B_{n'} H_{n'}|^2 \right\} \tag{6.17}$$

χ^2 may be minimised by first choosing $\{\tilde{B}_{n'}\}$ so as to minimise the terms under the summation sign. This will determine $\tilde{B}_0$ and the remaining term may be made to vanish by choosing $b=(\tilde{y}_0-\tilde{B}_0)/N$. The task is therefore reduced to that of minimising

$$\chi^2 = (1/N\sigma^2) \sum_{n'=1}^{N-1} | \tilde{y}_{n'} - \tilde{B}_{n'}\tilde{H}_{n'} |^2 \qquad (6.18)$$

It has been pointed out that the transform sets have conjugate symmetry about n'= N/2 (assuming N even). Equation (6.18) may therefore be written

$$\chi^2 = (2/N\sigma^2)\left\{ \sum_{n'=1}^{N/2-1} |\tilde{y}_{n'} - \tilde{B}_{n'}\tilde{H}_{n'}|^2 + \frac{1}{2}|\tilde{y}_{N/2} - \tilde{B}_{N/2}\tilde{H}_{N/2}|^2 \right\} \qquad (6.19)$$

Now as n' increases towards N/2, the value of $|\tilde{B}_{n'}\tilde{H}_{n'}|$ will usually decrease while $|\tilde{y}_{n'}|$ becomes dominated by noise. The expected value of $|\tilde{y}_{n'}|^2$ for $n' \to N/2$ is $N\sigma^2$ (from equation 6.10) and hence the expected value of $|\tilde{y}_{n'} - \tilde{B}_{n'}\tilde{H}_{n'}|^2$ approaches $N\sigma^2$. Thus for n' greater than some number M, which depends on the signal to noise ratio of the data, the contribution of each term to the total χ^2 is unity. The task of minimising χ^2 is further reduced to that of minimising χ_M^2 where

$$\chi_M^2 = (2/N\sigma^2) \sum_{n'=1}^{M} | \tilde{y}_{n'} - \tilde{B}_{n'}\tilde{H}_{n'} |^2$$

$$= (2/N\sigma^2) \sum_{n'=1}^{M} |\tilde{H}_{n'}|^2 |\tilde{y}_{n'}/\tilde{H}_{n'} - \tilde{B}_{n'}|^2 \qquad (6.20)$$

where M is chosen such that, for n'>M, the signal contribution to $\tilde{y}_{n'}$ is small compared to the noise contribution. The factor $N\sigma^2$ is equal to the expected value of $|\tilde{y}_{n'}|^2$ and is easily obtained from the power spectrum of the data (Figure 6.1).

The interpretation of (6.20) is as follows: $|\tilde{H}_{n'}|^2$ is the 'power spectrum' of the instrument function while $\tilde{y}_{n'}/\tilde{H}_{n'}$ represents the

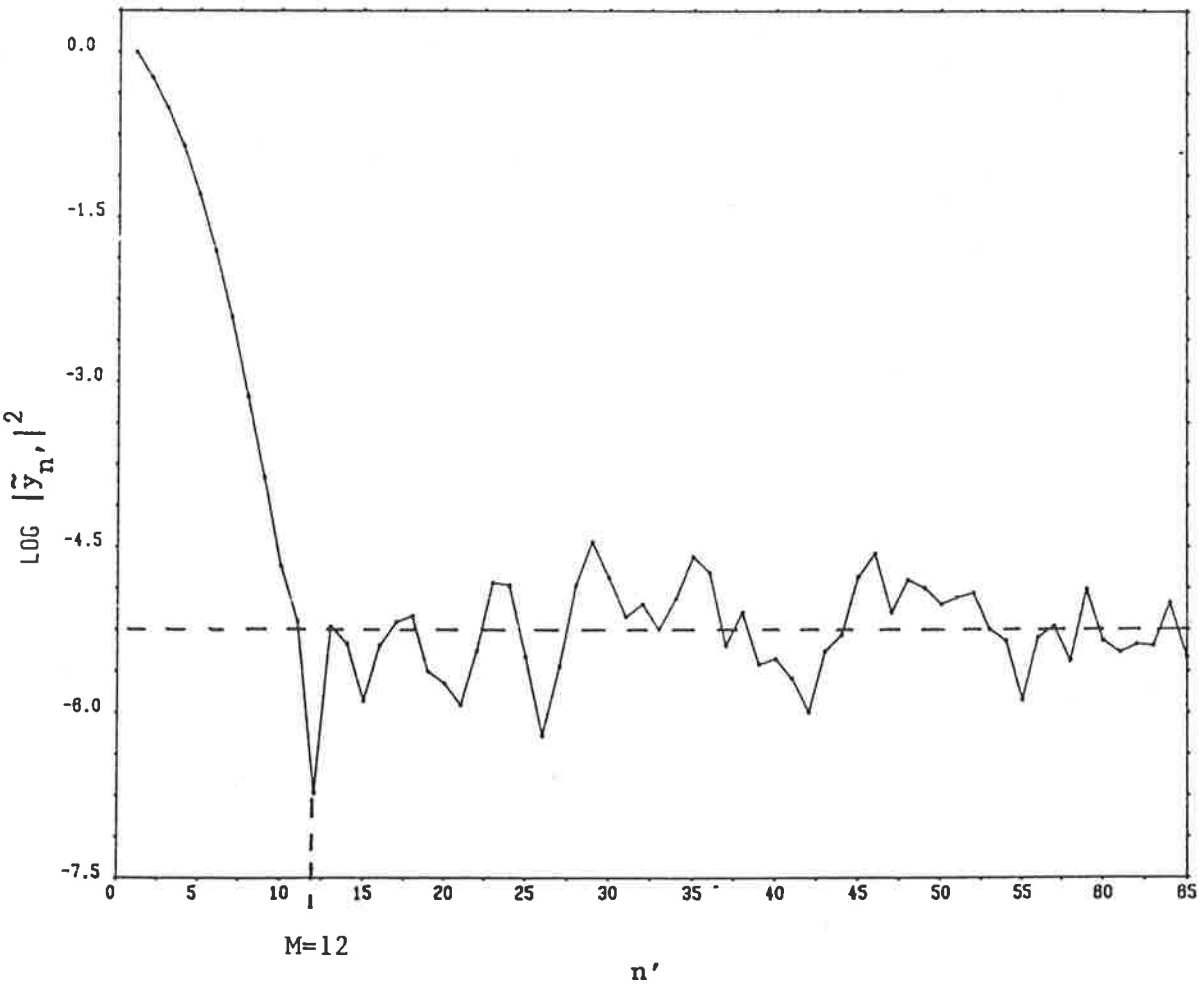

Figure 6.1 Discrete power spectrum of a typical profile. The squared moduli of the Fourier components are plotted on a logarithmic scale against the index n'. Only the first half of the spectrum is shown, the second half is a mirror image. The data have been normalised so that $|\tilde{y}_0|^2=1$. Only the first 12 points are considered in the least squares fitting procedure, the remainder being noise-dominated. The expectation value of $|\tilde{y}_{n'}|^2$ for n'>M is $N\sigma^2$ as indicated by the broken line.

transform of the direct deconvolution of the data. We are thus performing a deconvolution of the data followed by a least-squares fit to the source function in the transform domain, using $|\tilde{H}_{n'}|^2$ as a weighting function. The use of the instrument function power spectrum as a weighting function, together with truncation of the data transform at n'= M ensures the suppression of the high-frequency, noise-dominated components.

6.3 Form of the Source Transform

The source transform has conjugate symmetry about n'= N/2 and is given by (Wilksch 1975)

$$\tilde{B}_{n'} = r \exp(-pn'^2 - iqn') \qquad n'=0\ldots N/2$$
$$\tilde{B}_{N-n'} = \tilde{B}^*_{n'} \qquad n'=1\ldots N/2-1 \qquad (6.21)$$

where $p = (\pi m_0 N_\Delta / cN)^2 (2kT/M)$

$q = 2\pi n_r / N$

$r = S\Omega Q \tau_c t_d N_\Delta A_\Delta L$

and m_0 is the spectrometer order at the wavelength of interest

N_Δ is the number of channels corresponding to one order

A_Δ is the area under one period of the Airy function

n_r is the peak channel of the recorded profile.

The parameter p is proportional to the temperature T of the emitting species while r is proportional to the source radiance L. Parameter q is related to v_r, the line-of-sight component of the wind velocity by

$$n_r = m_0 N_\Delta v_r/c + n_0 \qquad (6.22)$$

where n_0 is the peak channel corresponding to the rest-frame wavelength.

6.4 Obtaining the Instrument Function

In this work, the instrument function was obtained by first recording, under normal operating conditions, a line profile of the λ546nm emission of Hg^{198}. The recorded profile must be relatively noise-free; that is, $\{\tilde{H}_{n'}\}$ becomes noise-dominated only for some n' in excess of the number M of equation (6.20). Several steps are necessary in order to obtain from this profile an instrument function applicable at λ630nm.

First, the line width of the λ546nm emission is not negligible and must be removed from the recorded profile. This is achieved by deconvolving the profile with a Gaussian curve of width 0.54pm corresponding to a temperature of 300K. This yields the instrument function applicable at λ546nm.

Second, in order to adapt the instrument function to a different wavelength we consider its component functions as functions of channel number. The defect and aperture functions, thus considered, are unaffected by a change of wavelength whereas the Airy function undergoes a change of scale; that is, the number of channels corresponding to one period of the Airy function is changed in proportion to the change in wavelength. Furthermore, the reflective finesse will usually vary with wavelength, leading to further modification of the Airy function.

The instrument function at λ546nm is thus deconvolved with the Airy function appropriate to that wavelength and the resulting function convolved with an Airy function appropriate to λ630nm. This step requires that the reflective finesse be known at the two wavelengths.

Finally, the peak of the instrument function is arbitrarily shifted to channel zero. This step is carried out in the transform domain by application of the shift theorem.

6.5 Estimation of Airglow Parameters

A grid-search procedure (Bevington 1969) is used to find a minimum value of χ_M^2 (equation 6.20) by variation of the three parameters p,q and r which determine $\{\tilde{B}_n,\}$ according to (6.21). When the minimum is located, the final values of p,q and r are converted back to estimates of temperature, peak position and emission intensity. The analysis routine also returns an estimate of Nb (equation 6.17), the total number of counts due to background sources.

An estimate of the uncertainty in the best-fit values of p,q, and r is obtained using the method described by Bevington (1969). The uncertainty in the estimate of a parameter is taken to be that departure from the best-fit value which gives rise to an increase of unity in χ_M^2.

6.6 Determination of Wind Velocity

Temperature variations within the Fabry-Perot etalon cause changes in the mean plate separation which in turn cause the instrument wavelength scale to drift. This must be corrected before wind velocities can be calculated. Furthermore, in the absence of a laboratory source of $O(^1D)$ λ630nm radiation, a zero velocity reference

must be established.

Instrument drift is monitored by frequent wavelength calibrations using the λ630.5nm emission of Ne^{20}. Calibrations are performed before and after each atmospheric observation. The calibration procedure takes 1-2 minutes and does not intrude significantly on observing time.

Figure 6.2 shows the peak positions of calibration and atmospheric profiles as functions of time over a few hours of observation. Drift is corrected by subtracting from each atmospheric peak position the value of the calibration curve, linearly interpolated at the midpoint of the atmospheric observation.

A zero velocity reference is established by assuming that the vertical component of the velocity, averaged over all zenith observations made on that night, is zero. This assumption is unlikely to lead to errors greater than a few $m.s^{-1}$. The quantity n_0 of equation (6.22) is therefore determined, enabling line-of-sight velocities to be calculated.

In order to calculate the horizontal component of velocity we consider Figure 6.3 which shows the instrument viewing geometry. The line-of-sight velocity v_r is given by

$$v_r = v_h \sin\theta + v_z \cos\theta \qquad (6.23)$$

where v_h is the horizontal component

v_z is the vertical component

and θ is the zenith angle of the observation

Vertical velocities of several tens of $m.s^{-1}$ are frequently encountered in the auroral zone even during quiet geomagnetic conditions. During disturbed conditions velocities of up to $100m.s^{-1}$ have been observed (Wardill & Jacka 1986; Rees et al. 1984a).

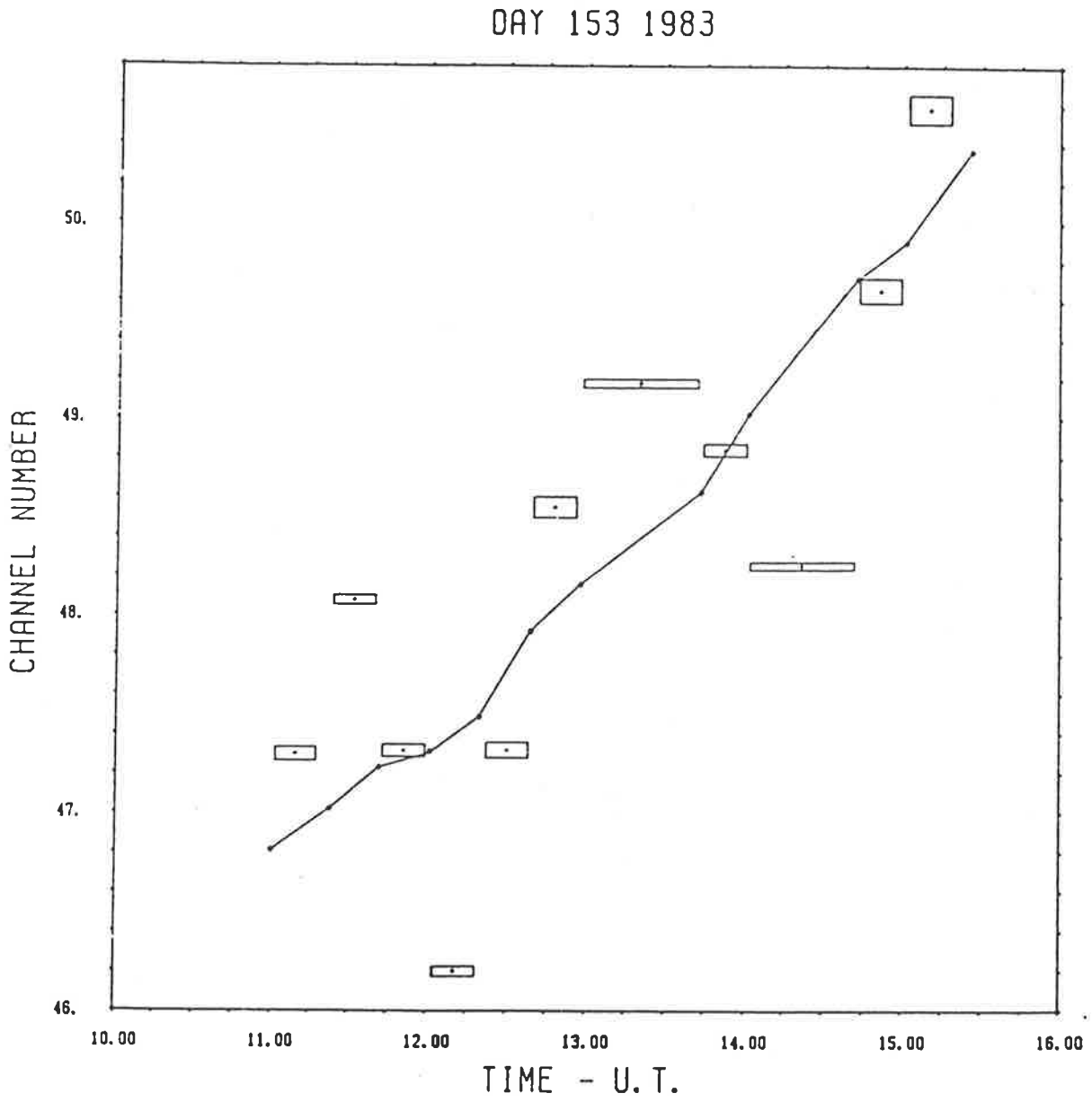

Figure 6.2 Correction of wavelength drift: The points joined by the solid line are peak positions of the calibration profiles. Airglow/auroral profiles are represented by the rectangles which indicate the duration of the observation and the uncertainty in the determination of peak position. Wavelength drift is corrected by subtracting from the airglow/auroral peak positions the value of the calibration curve, linearly interpolated at the midpoint of the observation.

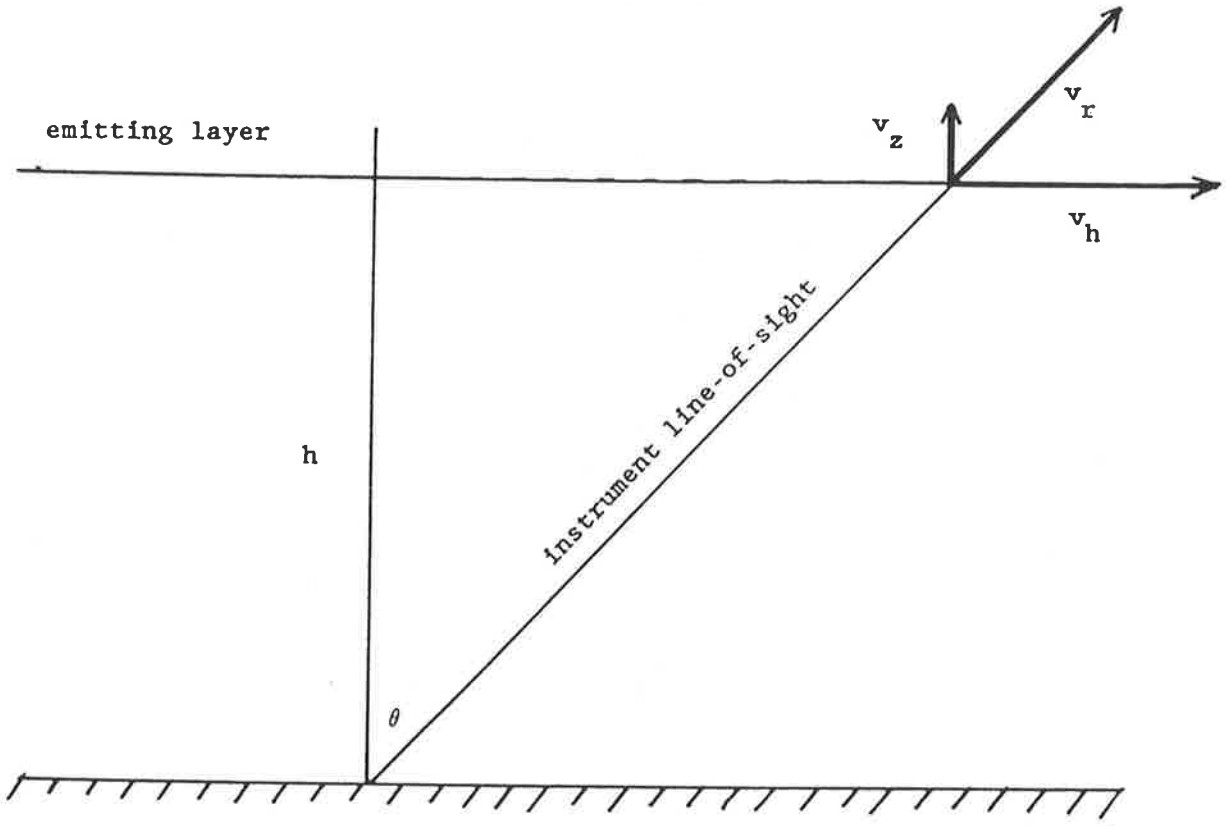

Figure 6.3 Instrument viewing geometry: The emitting layer is at height h, where the horizontal and vertical components of the wind velocity are v_h, v_z. The sum of the projections of these components onto the instrument line of sight gives the radial velocity v_r.

The vertical velocity can, of course, only be measured directly above the observatory (θ=0) whereas v_r is measured some 400km away (for θ=60°). Furthermore, measurements of the overhead vertical velocity and of v_r are typically separated in time by at least 20 minutes. It is unreasonable to assume that the vertical velocity measured overhead can be reliably used in the determination of v_h at some other time and location. The second term on the right of equation (6.23) is therefore unknown and constitutes a significant source of error in the determination of v_h.

The procedure adopted in this work is to calculate v_h from (6.23) under the assumption that v_z=0. The root-mean-square value of the measurements of v_z made overhead on that night is then calculated and taken as an estimate of the typical magnitude of v_z at the other observing locations. This is combined with the statistical error in v_r to give an estimate of the uncertainty in v_h.

Chapter 7

RESULTS OF OBSERVATIONS

7.1 The Data Set

The author was based at the *Australian National Antarctic Research Expeditions* station at Mawson (67.6°S, 62.9°E) from December 1982 to January 1984. The spectrometer was operated during the period January 17, 1983 to January 10, 1984 whenever clear skies permitted. Both the single etalon (nighttime) and dual etalon (daytime) configurations were used. Single etalon observations were confined to the period from February to October while most of the daytime observations were made outside this period. Unfortunately, the computing facilities at Mawson were severely limited and the complete analysis of the data could not begin until the author's return to Australia in February 1984.

The analysis of the daytime data proved difficult. The recovered λ630nm line spectrum, obtained by subtracting the spectrum of scattered sunlight from the spectrum of the sky, was frequently found to be distorted to such an extent that further analysis was impossible. Also, the time resolution achieved in the daytime observations was very poor, with a single observation typically requiring ninety minutes of signal integration. The frequent interruption of summer observations by patchy cloud caused further problems. It was therefore decided that the daytime observations were unlikely to yield reliable results and they will not be discussed further in this report.

Analysis of the data obtained from the single etalon configuration was straightforward. These observations were made at nighttime during the winter and equinoxes of 1983. After discarding those observations affected by cloud, a total of 60 nights of reliable data was obtained. Table 7.1 shows the dates on which observations were made, with the corresponding values of the daily A_p index. (Note: a typical night's observing covers two UT dates, finishing at ~0100 UT. In the following sections, all dates will refer to the UT day on which observations *commenced*, and on which the majority of the night's observations was therefore made.)

7.2 Procedure for Averaging Wind and Temperature Results

In order to investigate the dependence of the observed wind and temperature on time, geomagnetic activity, and IMF B_y, we require a procedure for averaging results over several nights.

Consider the results obtained from a single night's observations; these consist of a set of wind and temperature measurements distributed over five viewing directions (the four geographic cardinal directions and the zenith). The wind and temperature measurements are each treated as a set of five time series; one series for each viewing direction. A single observation requires ~20 minutes of signal integration and thus the members of a given series are separated in time by approximately 5 x 20 = 100 minutes. Figure 7.1 illustrates the results obtained on a typical night (June 14, 1983).

To allow results to be averaged over several nights, a set of half-hourly samples is derived from each series by linear interpolation. The samples are taken on the UT hour and half-hour. Average results are then obtained by calculating, for each sample time, the mean values of the wind and temperature samples in each of the viewing directions.

Table 7.1

Date	Day No.	Ap
Feb 02 1983	033	5
Feb 07 1983	038	43
Feb 08 1983	039	18
Feb 09 1983	040	18
Feb 20 1983	051	41
March 10 1983	069	7
March 12 1983	071	53
March 14 1983	073	26
March 16 1983	075	11
March 18 1983	077	20
March 21 1983	080	12
March 27 1983	086	3
April 11 1983	101	8
April 13 1983	103	36
April 14 1983	104	45
April 26 1983	116	28
April 27 1983	117	14
April 28 1983	118	12
April 29 1983	119	39
May 02 1983	122	14
May 17 1983	137	64
May 18 1983	138	12
May 20 1983	140	10
May 22 1983	142	51
May 24 1983	144	77
May 26 1983	146	10
May 27 1983	147	11
May 30 1983	150	9
June 02 1983	153	8
June 03 1983	154	6
June 05 1983	156	6
June 06 1983	157	11
June 08 1983	159	12
June 09 1983	160	20
June 12 1983	163	16
June 13 1983	164	70
June 14 1983	165	12
June 15 1983	166	17
June 16 1983	167	8
June 17 1983	168	17
June 23 1983	174	17
June 24 1983	175	6
June 26 1983	177	13

Table 7.1 cont.

Date	Day No.	Ap
July 03 1983	184	8
July 04 1983	185	8
July 05 1983	186	6
July 13 1983	194	19
July 14 1983	195	6
July 15 1983	196	5
July 19 1983	200	9
July 20 1983	201	7
Sept 17 1983	260	25
Sept 18 1983	261	11
Sept 19 1983	262	54
Sept 20 1983	263	22
Sept 22 1983	265	13
Sept 23 1983	266	4
Oct 18 1983	291	51
Oct 19 1983	292	8
Oct 20 1983	293	6
Oct 23 1983	296	21

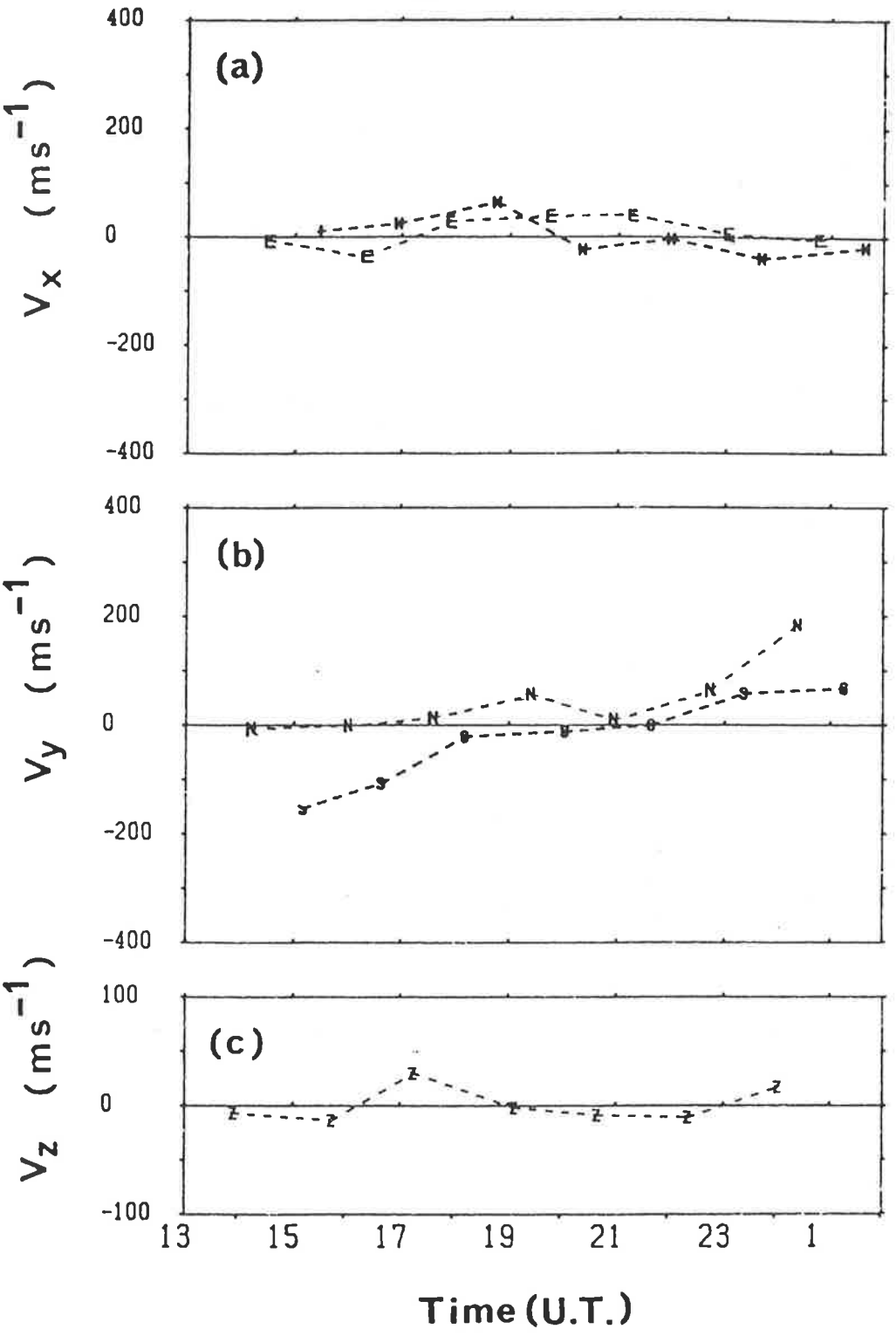

Figure 7.1 (a) zonal (b) meridional and (c) vertical components of the thermospheric neutral wind velocity, measured on June 14, 1983. The symbols N,E,S,W,Z refer to the geographic direction in which a particular observation was made (north, east, south, west, zenith). Error bars have been omitted since they do not exceed the height of the symbols.

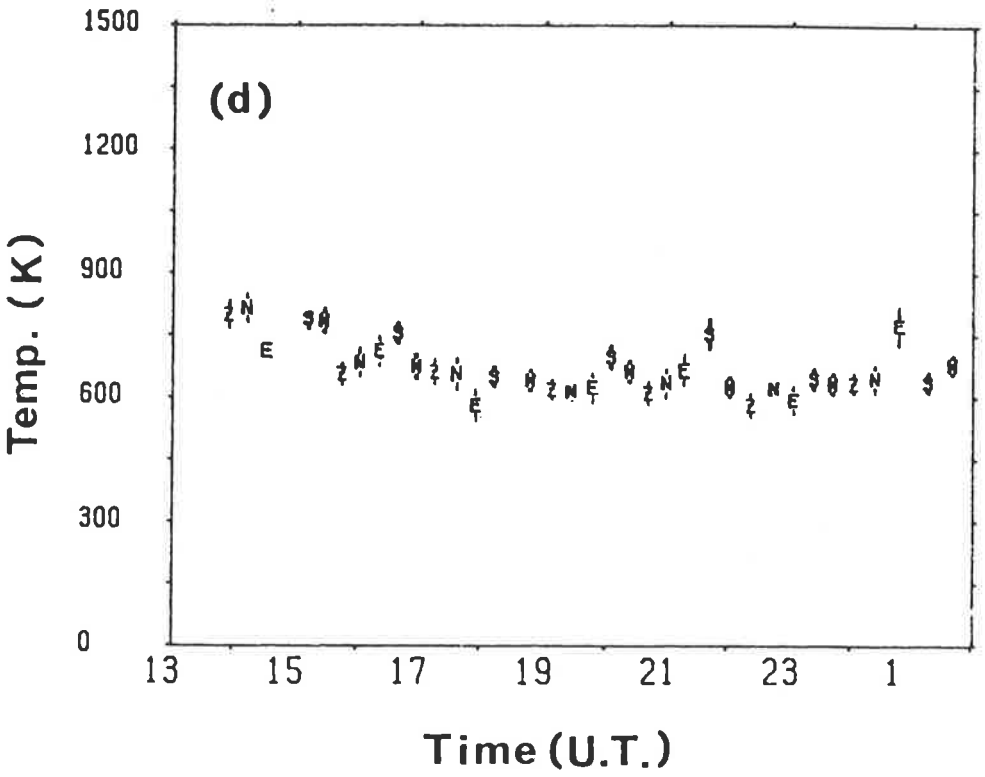

Figure 7.1 (d) observed thermospheric neutral temperature on June 14, 1983. Error bars are included where they exceed the height of the symbols.

Wind results will frequently be displayed in vector format to assist in interpretation. The meridional components of the half-hourly wind vectors are obtained by averaging the north-viewing and south-viewing samples. The zonal components are obtained by averaging the east-viewing and west-viewing samples. The resulting vector is thus an estimate of the overhead wind, obtained by linear interpolation both in time and in space.

7.3 Diurnal Variation and Geomagnetic Dependence of Thermospheric Neutral Winds and Temperatures

7.3.1 Introduction

Ion drag and solar radiation provide the primary sources of momentum and energy for the thermosphere at high latitudes. These sources have been described in Chapter 2 and the resulting circulation has been discussed.

Although the results and conclusions presented in Chapter 2 are well established, there have been very few ground-based observations of thermospheric winds and temperatures from high southern latitudes. The first step in the analysis of the Mawson data was, therefore, to examine the observed winds for the characteristics of ion drag forcing and to determine the dependence of winds upon geomagnetic activity.

7.3.2 Results

Wind and temperature observations were considered from 54 nights during the equinoxes and winter of 1983. In order to assess the dependence upon geomagnetic activity, these data were divided night by night into two categories, according to the A_p index. The first

category (A_p<25) corresponded to quiet to moderate conditions and contained 44 nights of observations. The second category ($A_p \geq 25$) corresponded to disturbed conditions and contained 10 nights.

Figure 7.2 shows the averages, over these categories, of the half-hourly wind vectors, transformed to geomagnetic coordinates. The general form of the circulation was the same in both cases with south-westward (sunward) flow in the afternoon and evening hours changing to equatorward (antisunward) flow around magnetic midnight. Wind speeds were typically ~100ms^{-1} during quiet/moderate conditions and increased to ~200ms^{-1} during disturbed conditions. A pronounced reduction in wind speed was observed to coincide with the maximum rate of change of wind direction around 2000-2200 magnetic local time (MLT).

The averages of the half-hourly temperature samples are shown for each A_p category in Figure 7.3. Averages have been calculated for each of the five viewing directions. The standard deviations of the temperature samples for a given time and direction ranged from 15 to 25K for A_p<25 and from 25 to 50K for $A_p \geq 25$. Error bars have, however, been omitted for clarity.

Significant and systematic differences in temperature were observed over the five viewing directions. The highest temperatures were observed to the geographic south and the lowest temperatures in the north and zenith. Observed temperatures were in the range 600-800K during quiet/moderate conditions and showed a broad minimum around 1600UT. Temperatures were considerably higher during disturbed conditions and ranged up to ~1200K with a broad minimum around 1800UT. However, the smaller sample size and greater variability of temperature made the exact nature of the diurnal variation uncertain.

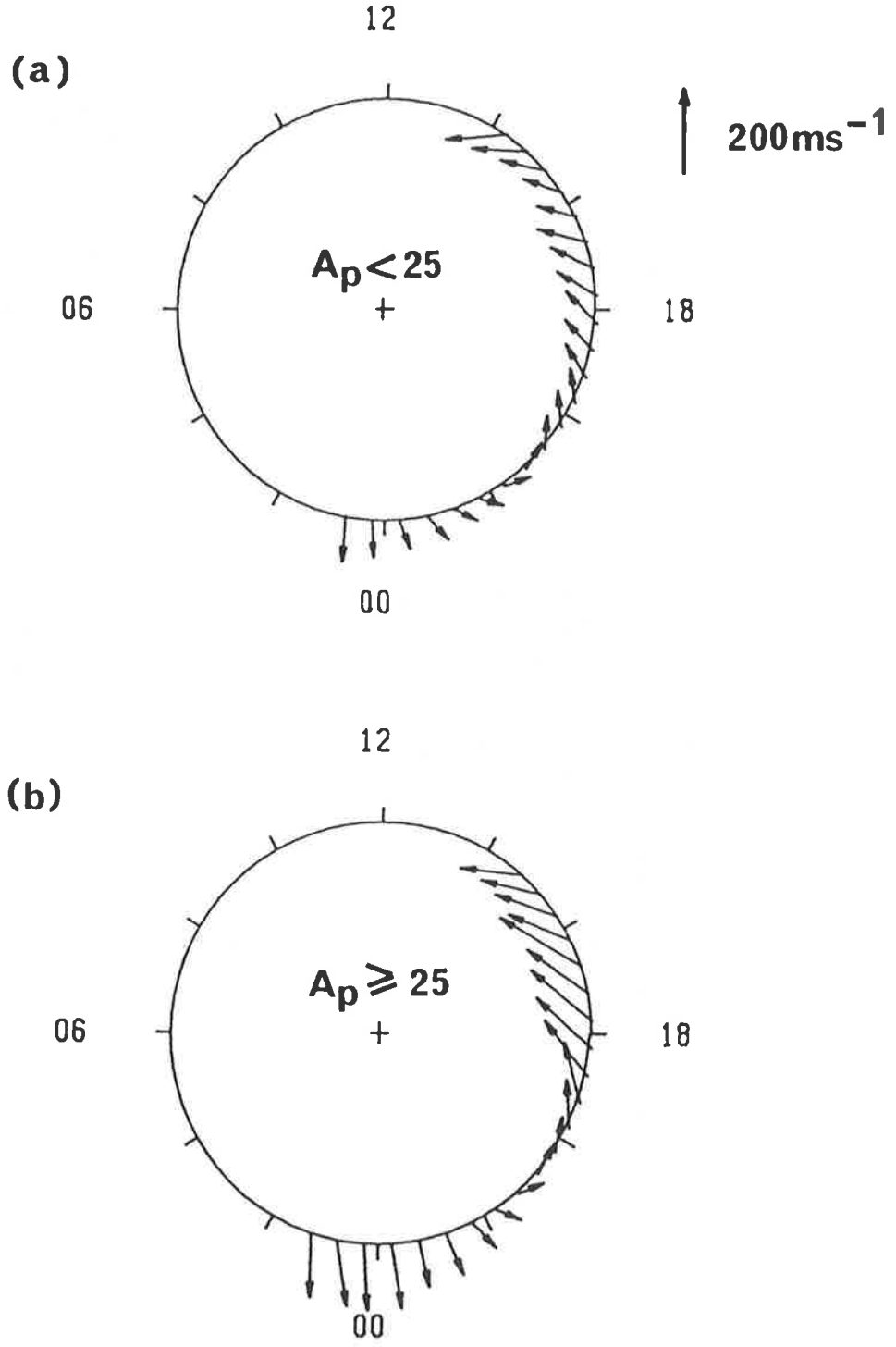

Figure 7.2 Average wind vectors observed under (a) quiet to moderate and (b) disturbed geomagnetic conditions. The vectors are plotted in geomagnetic coordinates; in each diagram geomagnetic south is toward the centre of the circle and magnetic local time is shown around the circumference.

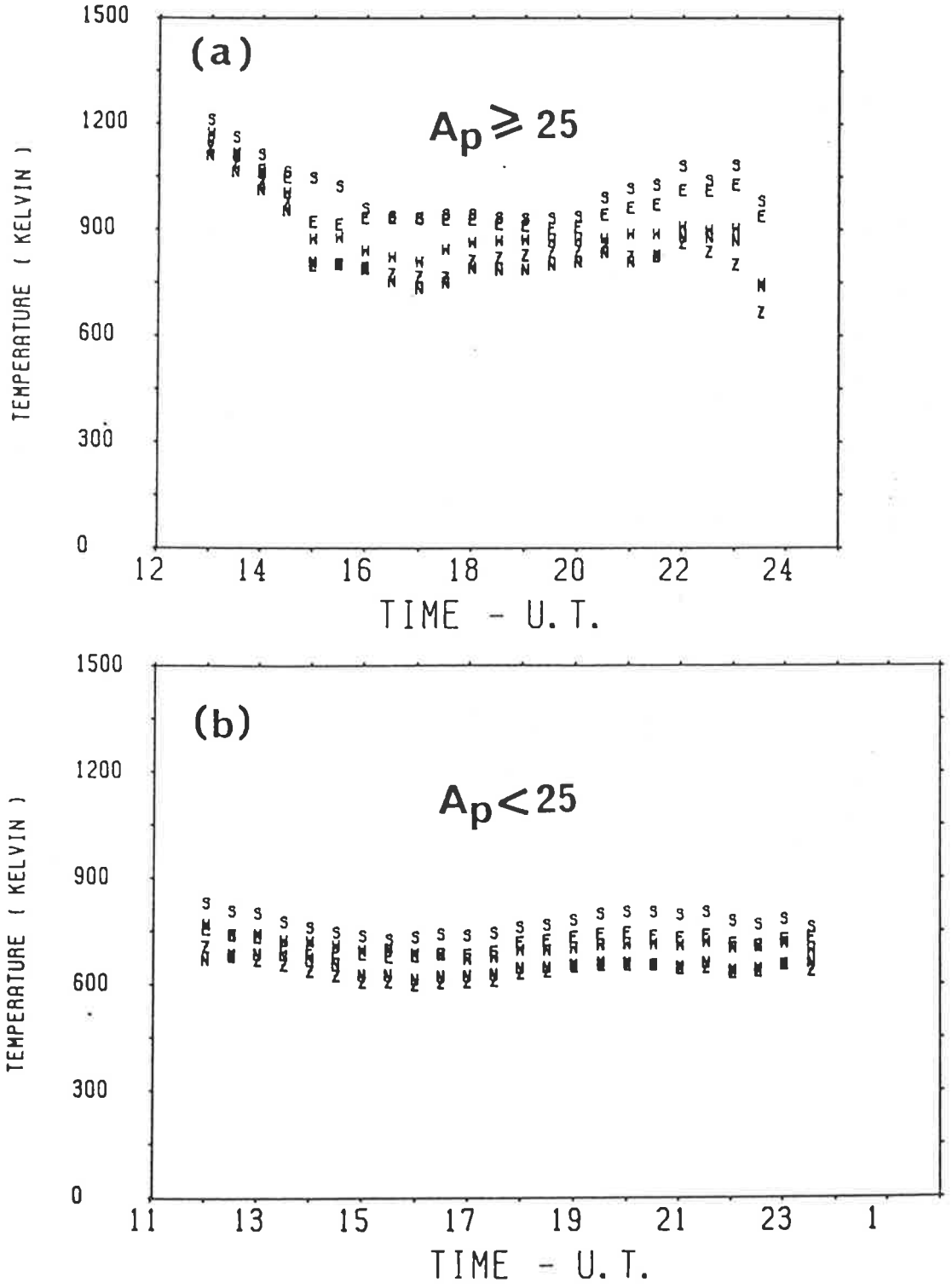

Figure 7.3 Average thermospheric temperature as a function of universal time observed under (a) quiet to moderate and (b) disturbed geomagnetic conditions. The symbols N,E,S,W,Z refer to the direction of observation. Error bars have been omitted for clarity.

7.3.3 Discussion

The observed winds followed the pattern of ion convection described in section 2.3.2. This is illustrated by Fig. 7.4 which shows an idealised version of the convection pattern on which the trajectory of Mawson is indicated.

The afternoon and evening measurements were made within the sunward-flowing region of the dusk convection cell. Equatorward winds observed near magnetic midnight occured as Mawson entered the region of antisunward convection across the polar cap. Reduced wind speeds were observed around 2000-2200 MLT as the station passed close to the stagnant centre of the dusk cell.

During disturbed conditions, the polar electric field strength and the ionospheric conductivity are enhanced. Both of these effects lead to increased ion-neutral momentum transfer and hence to increased neutral wind speeds as observed. The observed increase in temperature may be ascribed to the effects of Joule heating and particle precipitation.

These results therefore confirm the view that ion drag forcing is the principal momentum source for the high-latitude thermosphere, in agreement with similar studies in the northern hemisphere and with the predictions of thermospheric general circulation models.

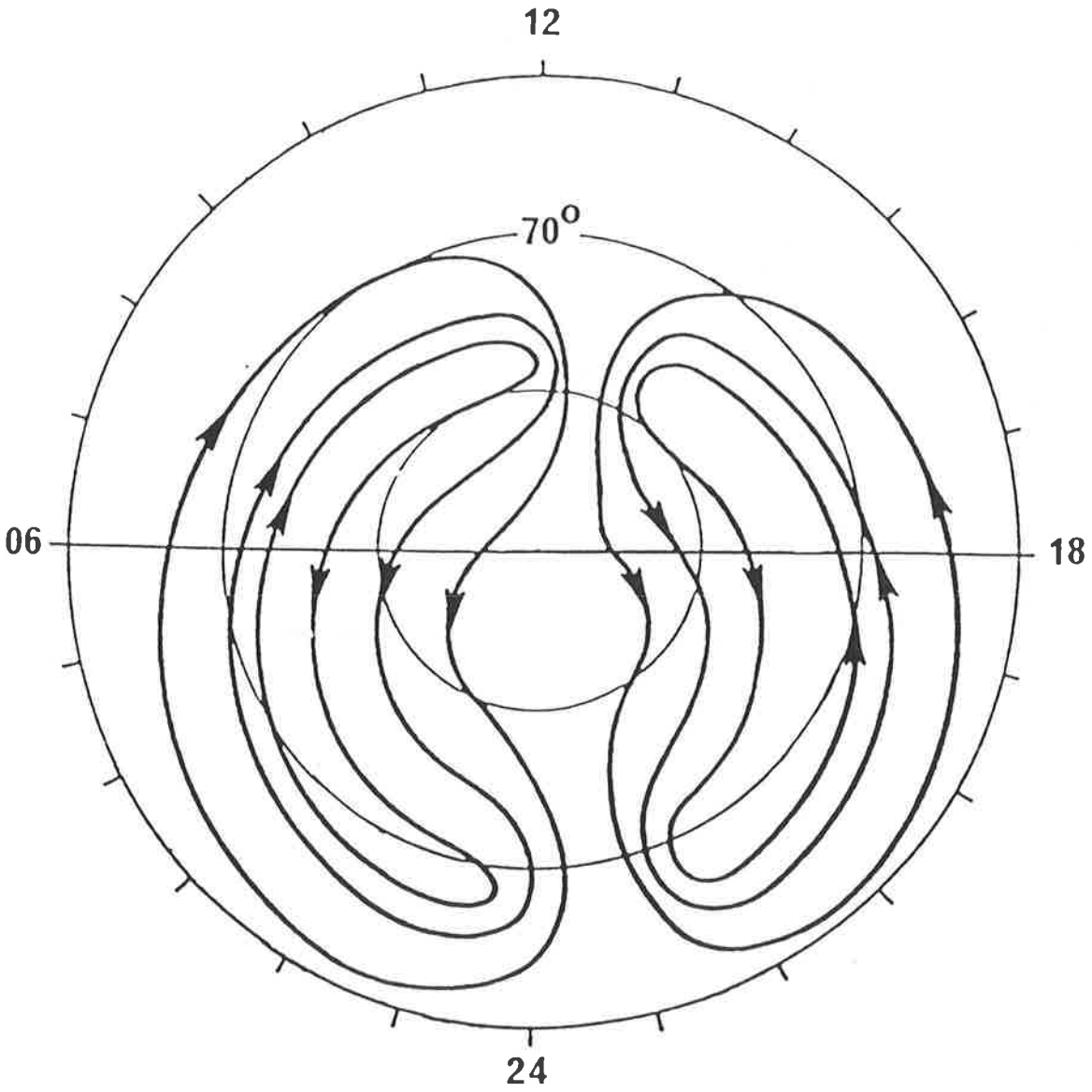

Figure 7.4 Idealised version of the high-latitude plasma convection pattern adapted from Heelis et al. (1982). Geomagnetic coordinates are used (geomagnetic latitude and magnetic local time). Mawson's trajectory through the pattern is indicated by the 70° geomagnetic latitude circle.

7.4 Dependence of Thermospheric Neutral Winds on the Y-component of the Interplanetary Magnetic Field

7.4.1 Introduction

The geometry of the high-latitude convection pattern has been discussed in section 2.3.2. In general, the pattern is not symmetric about the noon-midnight magnetic meridian but shows asymmetries which are related to the y-component of the interplanetary magnetic field (IMF B_y). In the northern hemisphere, the dawn circulation cell is enlarged for IMF $B_y<0$ and the dusk cell enlarged for IMF $B_y>0$. In the southern hemisphere the dusk cell is enlarged for IMF $B_y<0$ and the dawn cell enlarged for IMF $B_y>0$. Since the convecting ions provide the primary momentum source for the neutral thermosphere, similar asymmetries are to be expected in the neutral circulation.

Ground-based measurements from Spitsbergen ($78^{o}.2$N, 15.6^{o}E, $75^{o}\Lambda$) have shown a definite dependence of the neutral circulation on IMF B_y which was particularly evident in the zonal component of the flow around noon (McCormac and Smith 1984). Observations made in the northern hemisphere by the Dynamics Explorer-2 spacecraft have also shown a number of asymmetries in the neutral flow including: (1) an asymmetry in the polar cap flow, with the region of most rapid anti-sunward flow shifting from the dawn-side to the dusk-side as IMF B_y changed from positive to negative; (2) a shift in magnetic local time of the region of entry of neutral gas into the polar cap, from the dawn-side to the dusk-side of the noon-midnight meridian as IMF B_y changed from positive to negative; and (3) changes in the relative sizes of the dawn and dusk circulation cells consistent with the known changes in the geometry of the high-latitude ion convection pattern (McCormac et al. 1985). The dusk cell has been observed to dominate

entirely the high-latitude circulation during periods when IMF B_y was large and positive (5-10nT) (Killeen et al. 1984). These and other observations have been supported by the results of thermospheric model calculations which have used, as input, an IMF B_y-dependent description of the high-latitude electric field (Rees et al. 1986).

The location of Mawson within the auroral zone is well-suited for ground based investigation of the effects discussed above. The horizontal wind data were therefore examined for dependence upon the sign of IMF B_y.

7.4.2 Results

The horizontal wind data were grouped according to the sign of IMF B_y as measured by the IMP-8 spacecraft. IMP-8 was launched into a geocentric orbit of ~30 x 40 R_e on October 26, 1973 and has a period of ~12.5 days. The spacecraft is in the solar wind for 6-8 days per orbit, during which time interplanetary data are available. (Continuous monitoring of the IMF was previously provided by ISEE-3 which orbited the earth-sun libration point, approximately 240R_e sunward of the earth, until mid-1982 when it was redirected into the earth's magnetotail.)

Measurements of the IMF were available on 26 of the 54 nights on which thermospheric winds were observed. Examination of the hourly-averaged values of the IMF revealed 7 nights on which IMF B_y remained negative throughout the period of observation and 13 nights on which IMF B_y remained positive. The remaining 6 nights were rejected since the sign of IMF B_y was uncertain due to fluctuations or to data gaps.

Figures 7.5a and 7.5b show the averaged neutral wind vectors for IMF B_y negative and positive respectively. The patterns differ in several respects. For IMF B_y negative the observed wind speeds are generally larger and the transition from poleward to equatorward flow occurs 1-2 hours earlier than in the IMF B_y positive case. The most important difference, however, is to be found in the behaviour of the zonal component. For IMF B_y negative the zonal component is westward throughout the period of observation, whereas for IMF B_y positive, the zonal component shifts from westward to eastward at ~2200 MLT.

7.4.3 Comparison with the Predictions of a Thermospheric Model

The University College thermospheric general circulation model (TGCM) has been discussed in Chapter 2. Output from the model has been made available for comparison with the Mawson observations. The model output was sampled at Mawson's longitude and at an altitude appropriate to 630nm observations, yielding neutral temperatures and wind vectors as functions of latitude and of universal time. The high-latitude convection pattern was specified by the A2 and B2 models of Heppner and Maynard (1983). These models are discussed in section 2.3.2 and illustrated in Figure 2.7.

Two simulations were provided which are labelled JC and MC. The simulations have been widely used in the interpretation of northern hemisphere data from ground-based Fabry-Perot spectrometers and from Dynamics Explorer-2. In the JC simulation, for IMF B_y positive, the B2 convection pattern is applied to the northern hemisphere and the A2 pattern to the southern hemisphere. In the MC simulation, for IMF B_y negative, the A2 pattern is applied to the northern hemisphere and the B2 pattern to the southern hemisphere. The JC simulation is in fact more appropriate to conditions prevailing at December solstice while

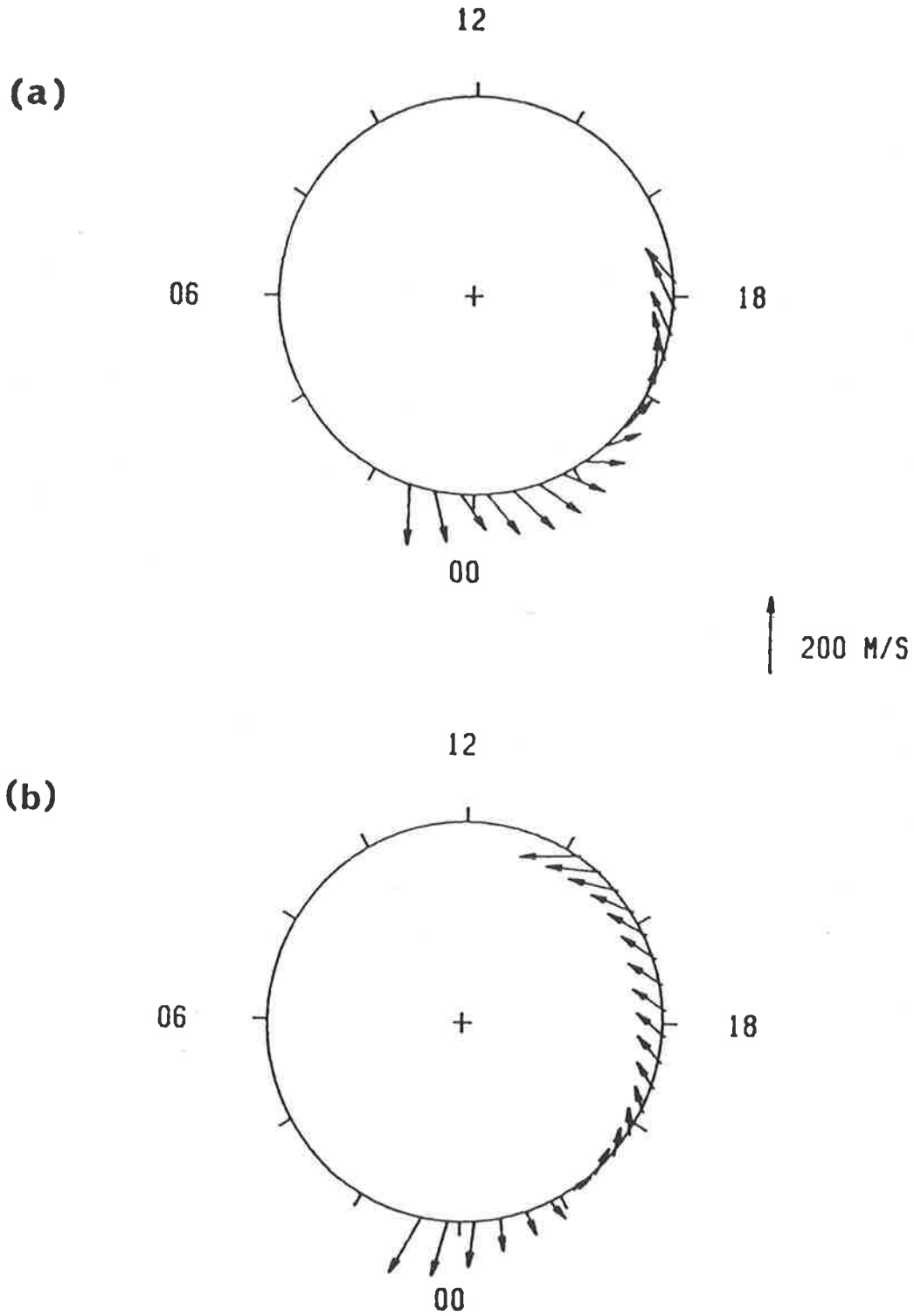

Figure 7.5 Average wind vectors plotted in geomagnetic coordinates:
(a) For IMF B_y negative
(b) For IMF B_y positive

the MC simulation is appropriate to June solstice. The differences in the circulation patterns predicted by the two simulations are, however, largely due to the differences in the convection fields and the predictions can therefore be meaningfully compared with the Mawson results, which were obtained during a period spanning the June solstice and both equinoxes. Finally, the simulations are appropriate to a time of high solar activity, whereas the Mawson results were obtained under average solar conditions. The observed wind speeds are therefore expected to be smaller than those predicted by the model and the observed wind pattern should be contracted toward the geomagnetic pole.

(i) JC Simulation

Figure 7.6a shows part of the output from the JC simulation. Wind vectors were available at 2^{o} intervals in geographic latitude and at 1.2 hour intervals in Universal Time. The vectors shown are for latitudes of 64^{o}, 68^{o} and 72^{o}; the latitude of Mawson is 67.6^{o}. The orientation of the vectors gives the wind direction in geographic coordinates; i.e. north is to the top of the page and east is to the right. Magnetic midnight at Mawson is at ~2230 UT.

The model predicts a region of sunward (westward) and equatorward winds in the late afternoon and evening hours, which are driven by the dusk convection cell. Sunward flow associated with the dawn convection cell is evident in the band of eastward winds which moves poleward past Mawson from 0600 to 1000 UT. Poleward winds are predicted during the noon and early afternoon.

The averaged observed wind vectors for IMF B_y positive are shown in Figure 7.6b for comparison. Note that the wind scale differs from that of Figure 7.6a. The observed and predicted wind directions are in

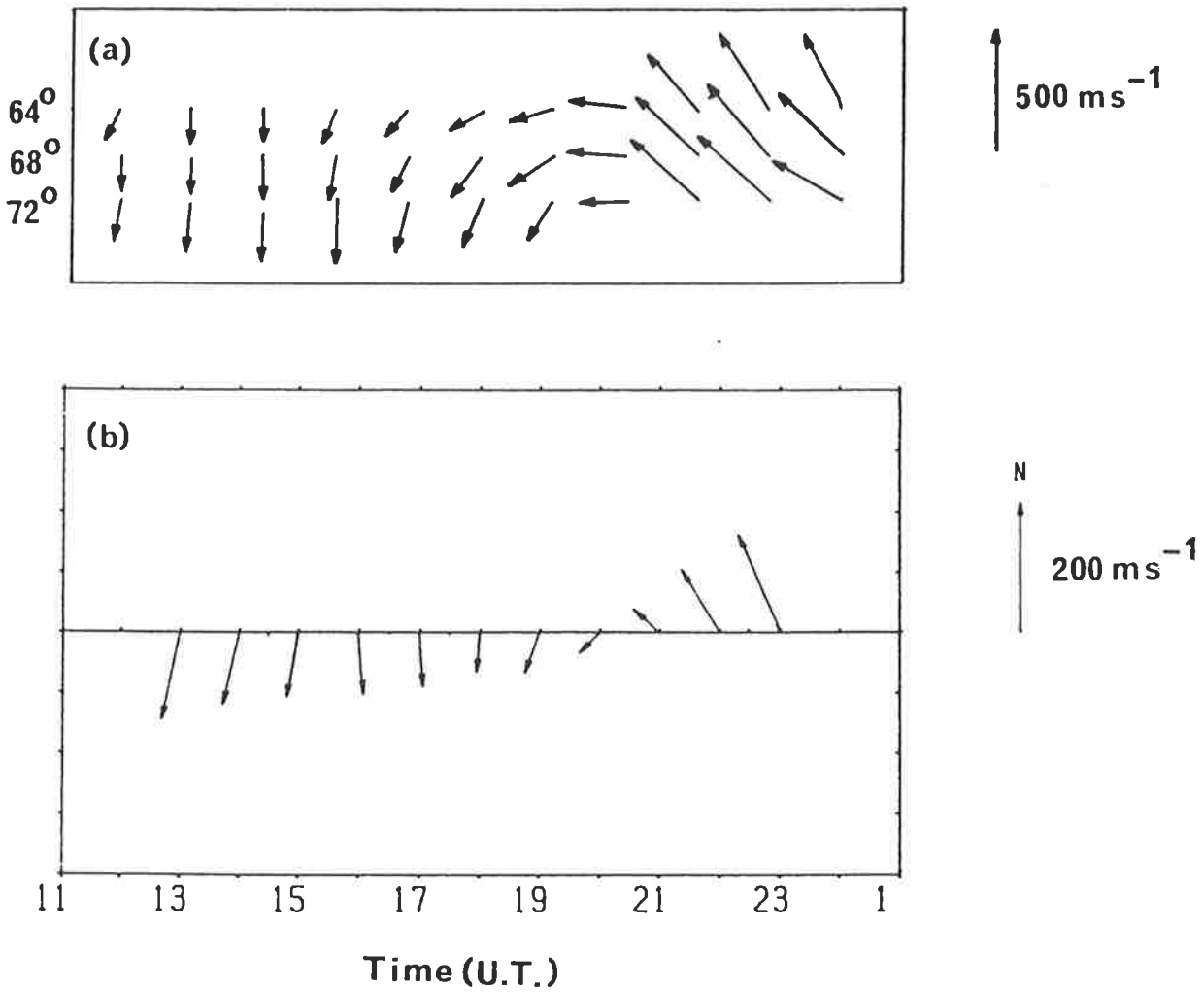

Figure 7.6 Comparison of observed winds with predictions of the University College model:
(a) model wind vectors for the JC simulation, shown for geographic latitudes 64 - 72°.
(b) average observed wind vectors for IMF B_y positive.

good agreement although the observed wind speeds are considerably smaller. The latitude at which the model winds best fit the observations is uncertain as the latitudinal variation of the model winds is small within the period of observations.

(ii) MC Simulation

Output from the MC simulation is shown in Figure 7.7a. The output was available at 5^{o} intervals in latitude and is shown for latitudes of 60^{o}, 65^{o}, 70^{o} and 75^{o}. In the evening hours, westward winds associated with the enlarged dusk convection cell are enhanced with respect to the complementary IMF B_y situation. The band of westward winds commences earlier and extends well into the morning hours, reversing the sunward flow seen in this sector in the JC simulation.

Averages of the observed wind vectors for IMF B_y negative are shown in figure 7.7b. After 1900 UT, enhanced westward winds were observed, whose direction was in reasonable agreement with the model predictions for 65^{o} and 70^{o} latitude. Prior to 1900UT, the observed winds were nearly poleward and corresponded more closely to the model predictions for 75^{o}. As in the IMF B_y positive case, the observed wind speeds were approximately one half of those predicted by the model.

7.4.4 Discussion

The observed winds show a strong dependence on the sign of IMF B_y, consistent with the results of previous studies in the northern hemisphere. The (geomagnetic) westward component observed around magnetic midnight when IMF B_y was negative suggests that the dusk circulation cell was considerably expanded and influenced the antisunward flow across the polar cap. Conversely, the observed eastward component when IMF B_y was positive indicates expansion of the dawn circulation cell.

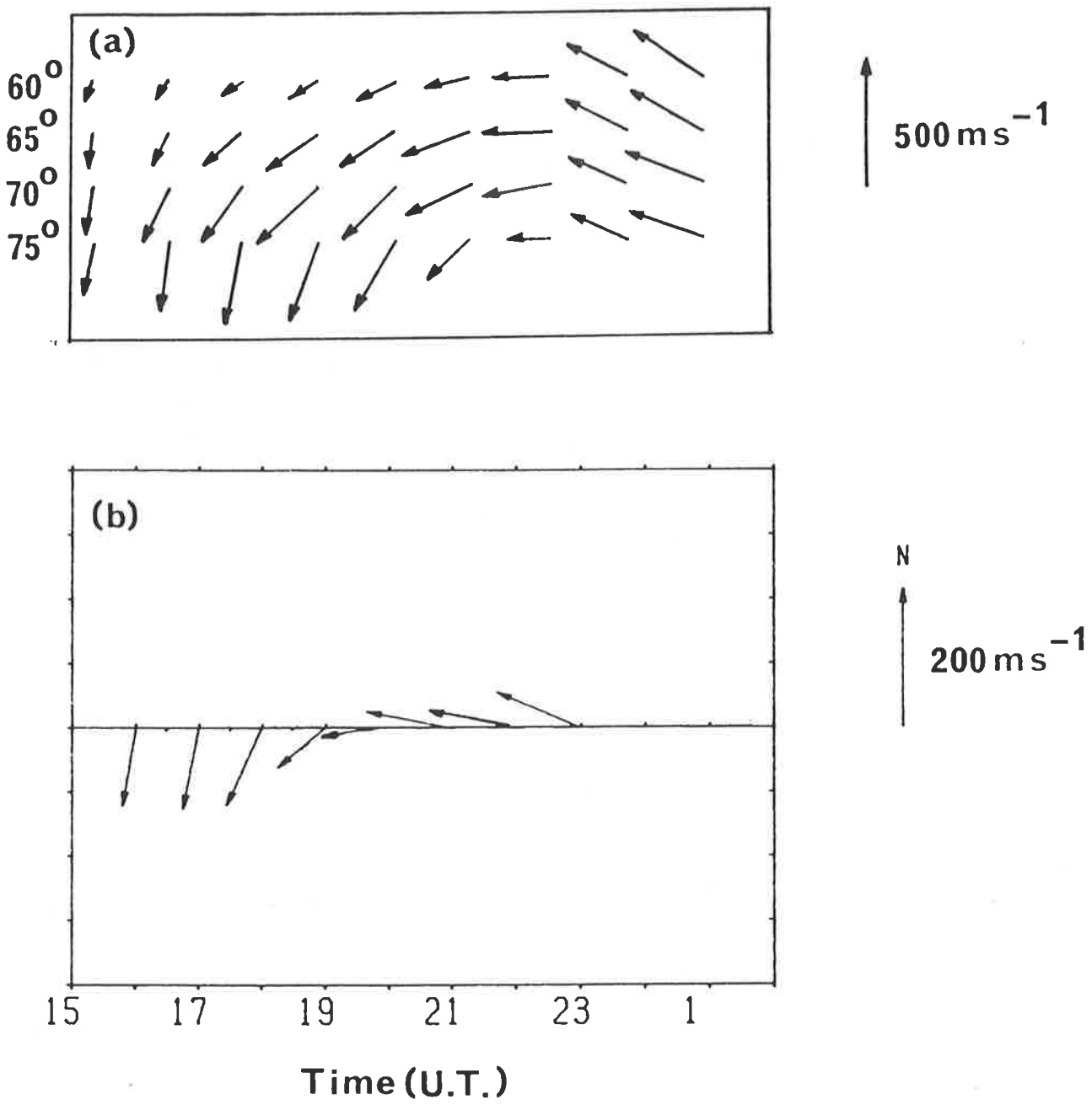

Figure 7.7 Comparison of observed winds with predictions of the University College model:
(a) model wind vectors for the MC simulation, shown for geographic latitudes 60 - 75°.
(b) average observed wind vectors for IMF B_y positive.

The comparison of observed winds and model predictions is encouraging and shows reasonable agreement of wind directions for IMF B_y positive and negative. The discrepancy between predicted and observed wind speeds is no doubt due, in part, to the assumption of high solar activity which applies to the model calculations.

One important feature of the model winds was not apparent in the observations due to the limited UT coverage; this concerns the relative effectiveness with which the dawn and dusk cells are driven for IMF B_y positive and negative respectively. The model results show that the (anticyclonic) dusk cell is present for IMF B_y positive and negative and is particularly well developed in the latter case, with strong westward flow occurring from ~1600-0400 UT. The eastward flow associated with the dawn cell is however quite weak for IMF B_y positive and is virtually absent for IMF B_y negative, having been reversed by the enhanced westward flow of the dusk cell. This can be explained by the fact that eastward-moving air parcels in the dawn cell are deflected to lower latitudes by the Coriolis force and are therefore removed from the region of ion convection. Westward-moving parcels, on the other hand, are constrained to follow the direction of ion convection since localised pressure gradient forces act to oppose the Coriolis force and hence to reduce the path curvature (McCormac and Smith 1984). In both hemispheres therefore, the anticyclonic dusk cell is more effectively driven than the cyclonic dawn cell.

7.5 Vertical Motions and Thermospheric Gravity Waves

7.5.1 Introduction

Observations were restricted to the zenith on 6 nights during 1983. These observations yielded information on vertical motions and allowed certain properties of thermospheric gravity waves to be inferred. Internal atmospheric gravity waves exist at periods greater than a characteristic value called the Väisälä-Brunt period; in the F-region this is ~15 minutes. In order to resolve features on this time-scale the signal integration time was fixed at 5 minutes. This is less than the average time used in observations of horizontal winds but gave adequate results nevertheless.

The dates of the observations are shown below with the corresponding values of the A_p index.

Date	Day Number	Ap
April 13, 1983	103	36
April 14, 1983	104	45
May 24, 1983	144	77
July 20, 1983	201	7
Sept. 19, 1983	262	54
Sept. 20, 1983	263	22

The results from May 24 and September 19 have been discussed previously by Wardill and Jacka (1986) but will be included in the present section for the sake of completeness. Certain parts of the discussion in section 7.5.3 have also been adapted from the above paper.

7.5.2 Results

The vertical wind measurements from all six nights are shown in Figure 7.8. Note that, in the absence of a rest-wavelength measurement, the zero velocity for a given night is taken to be the time-average of all vertical velocity measurements obtained on that night. The measurements are therefore subject to a systematic error equal to the mean value of the *true* vertical velocity over the period of observation.

The results show striking evidence of thermospheric gravity waves with oscillatory behaviour apparent on each night. Typical wind speeds were of the order of a few tens of ms^{-1} but often exceeded $50ms^{-1}$, and on occasion reached $100ms^{-1}$. The time-scale of the oscillations varied from ~20 to 60 minutes.

The results of July 20 are particularly interesting; this was a day of extremely low geomagnetic activity (A_p=7) yet vertical motions of $50ms^{-1}$ were observed during much of the night. Moderate to extremely disturbed conditions prevailed on the remaining days with A_p ranging from 22 to 77.

In order to determine the relationship between vertical motions and geomagnetic activity, the local magnetic and all-sky camera records were examined. Magnetic bay disturbances occurred on all 6 nights. On three nights, large magnetic bays were associated with distinctive features in the vertical wind records. We now consider each of these nights in turn:

(i) April 13, 1983

Figure 7.9 shows the vertical wind measurements for April 13, together with the observed temperature and the H-component of the local magnetogram. A negative bay disturbance of ~250nT amplitude

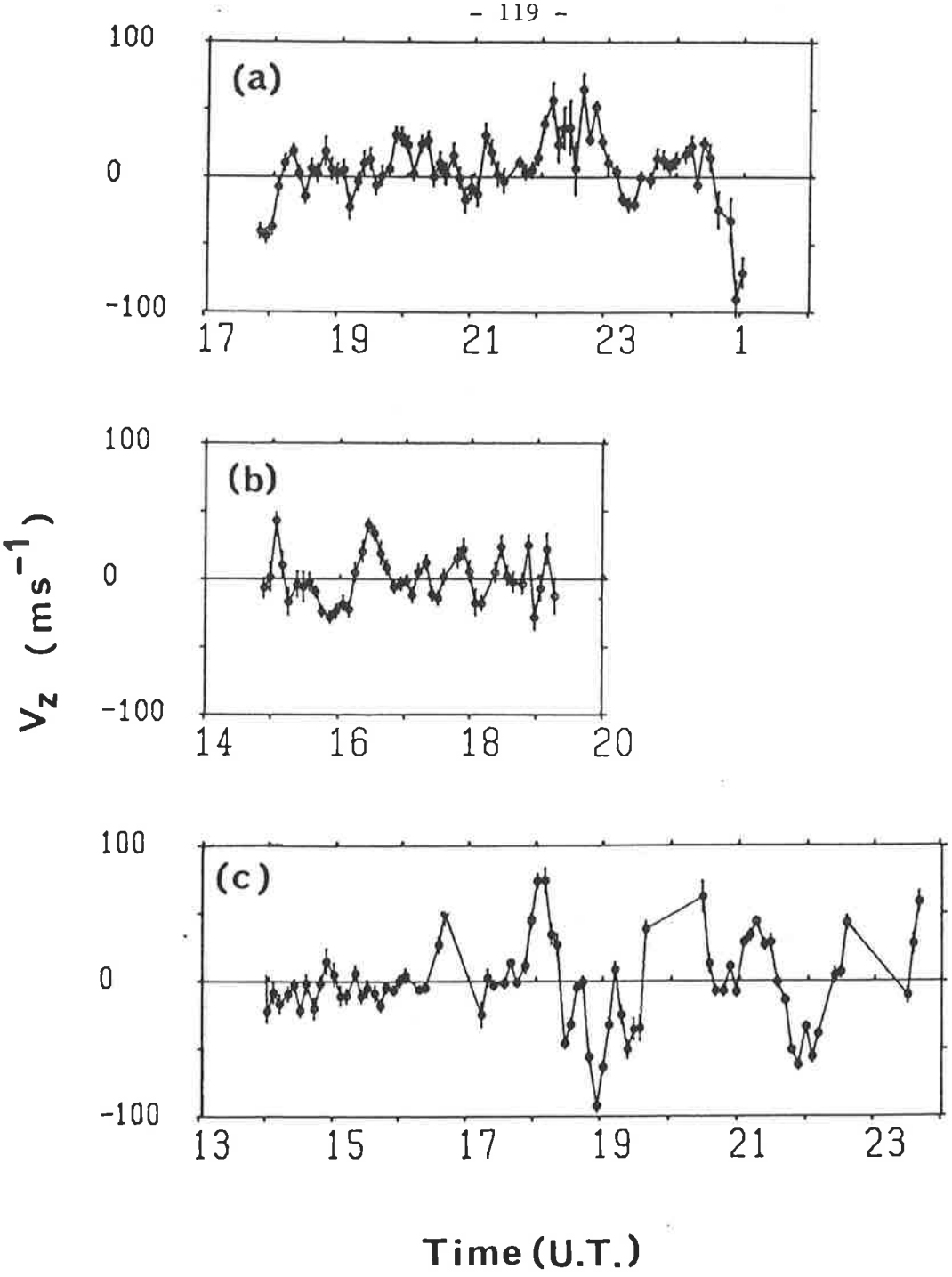

Figure 7.8 Vertical wind observations from:
(a) April 13, 1983
(b) April 14, 1983
(c) May 24, 1983

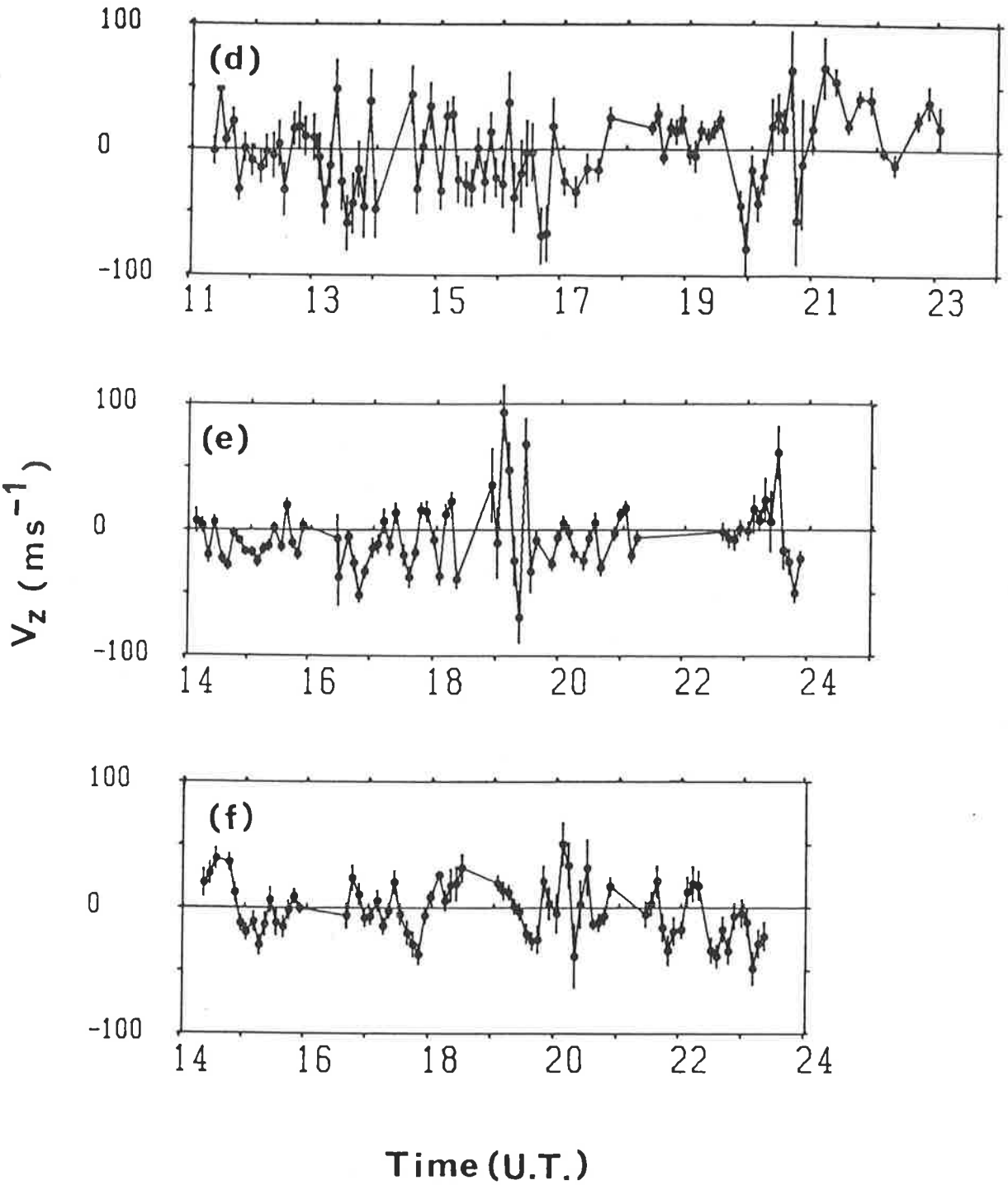

Figure 7.8 Vertical wind observations from:
(d) July 20, 1983
(e) September 19, 1983
(f) September 20, 1983

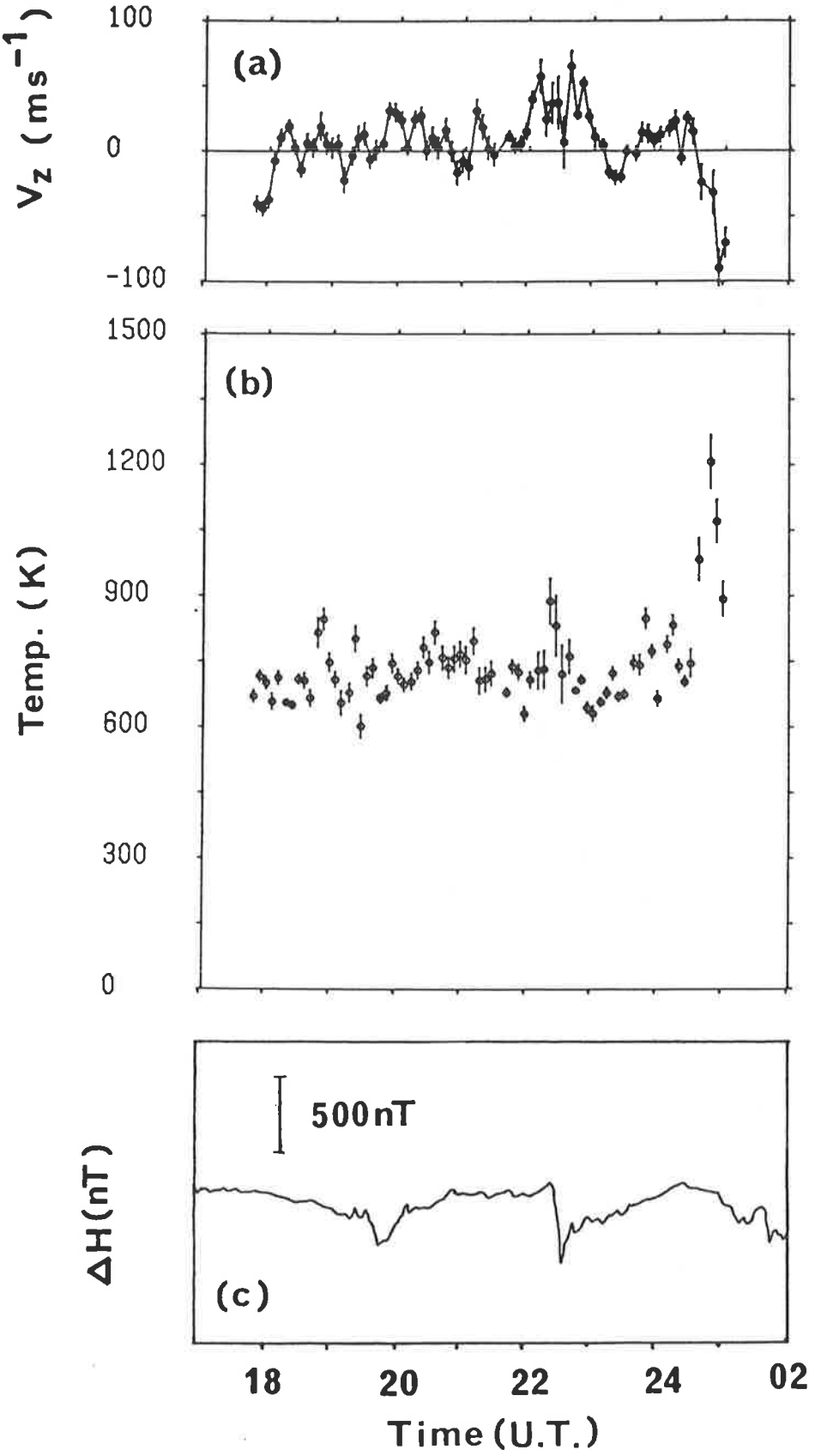

Figure 7.9 (a) vertical wind, (b) temperature and (c) H-component of the local magnetogram observed on April 13, 1983.

commenced at 2230UT. This coincided with a sudden increase in temperature of ~200K and a prolonged period of upward wind. Large downward winds of up to 100ms^{-1} were observed between 0030 and 0100UT. These winds coincided with a rapid increase in temperature from ~750K to ~1200K. The geomagnetic field was quiet during this time.

(ii) May 24, 1983

Figure 7.10 shows the vertical wind, the temperature and the magnetogram H-component for May 24. The geomagnetic field was quiet prior to 1600 UT and the vertical wind relatively small (<25ms^{-1}). The commencement of a large negative bay disturbance at 1630 UT was accompanied by an upward wind of 50ms^{-1} and was followed by the expansion phase of an auroral substorm, as indicated by the all-sky camera record. Oscillations of the vertical wind with zero mean and amplitude ~50ms^{-1} persisted throughout the subsequent 6 hours of observations, during which time a second negative bay disturbance occurred at 2030UT. The effects of the two disturbances are not readily separable in the period 2030-2230 UT.

The temperature data show little evidence of local heating, with the exception of moderate temperature enhancements from 1820 to 1930 UT and around 2200 UT. These were periods of sustained downward motion.

(iii) September 19, 1983

Figure 7.11 shows the results for September 19. The wind data reveal a group of oscillations of amplitude ~30ms^{-1} in the period 1630-1830 UT, during which time the geomagnetic field was relatively quiet. A negative disturbance occurred at 1900 UT, which was followed by the expansion phase of an auroral substorm. The thermosphere

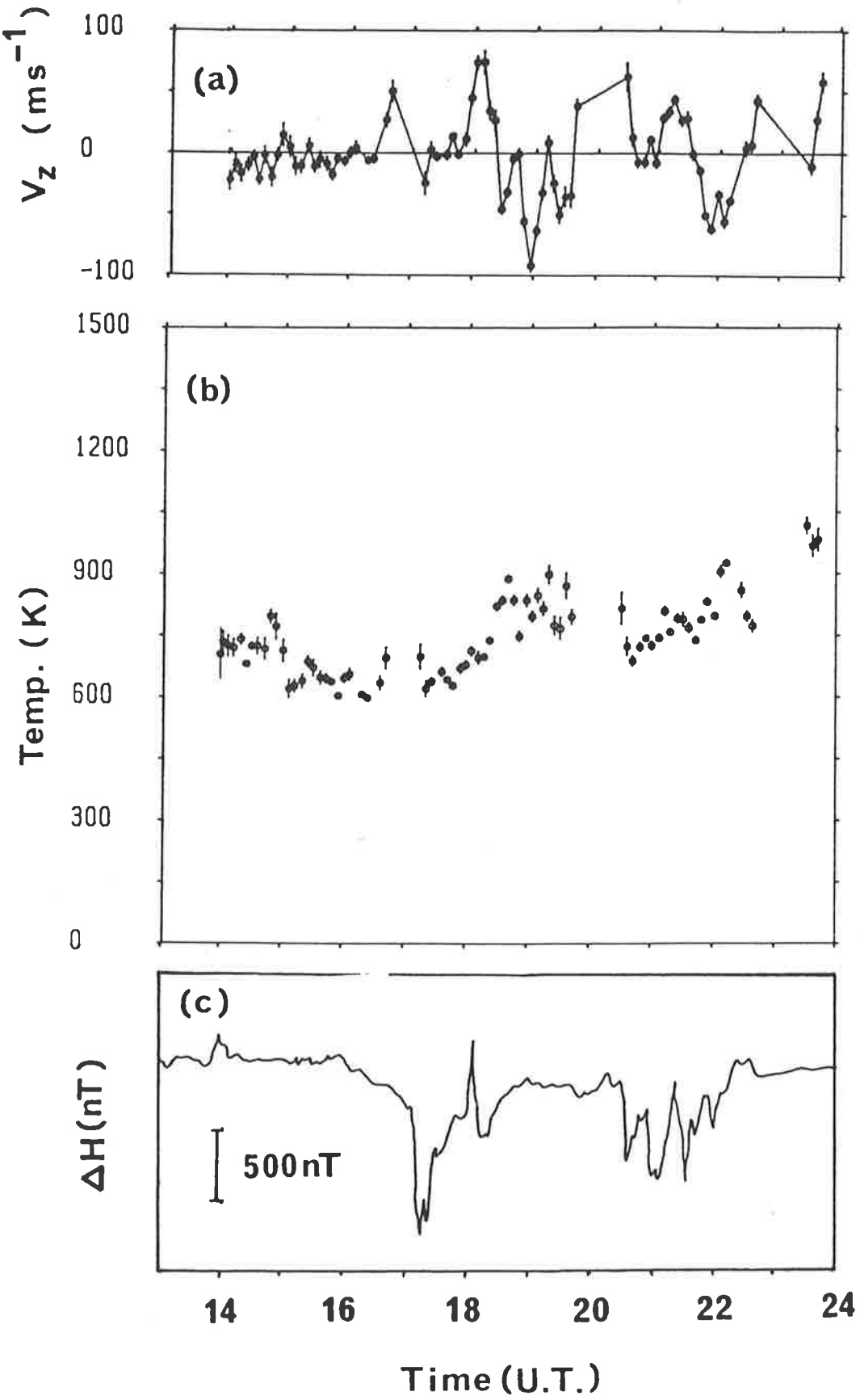

Figure 7.10 (a) vertical wind, (b) temperature and (c) H-component of the local magnetogram observed on May 24, 1983.

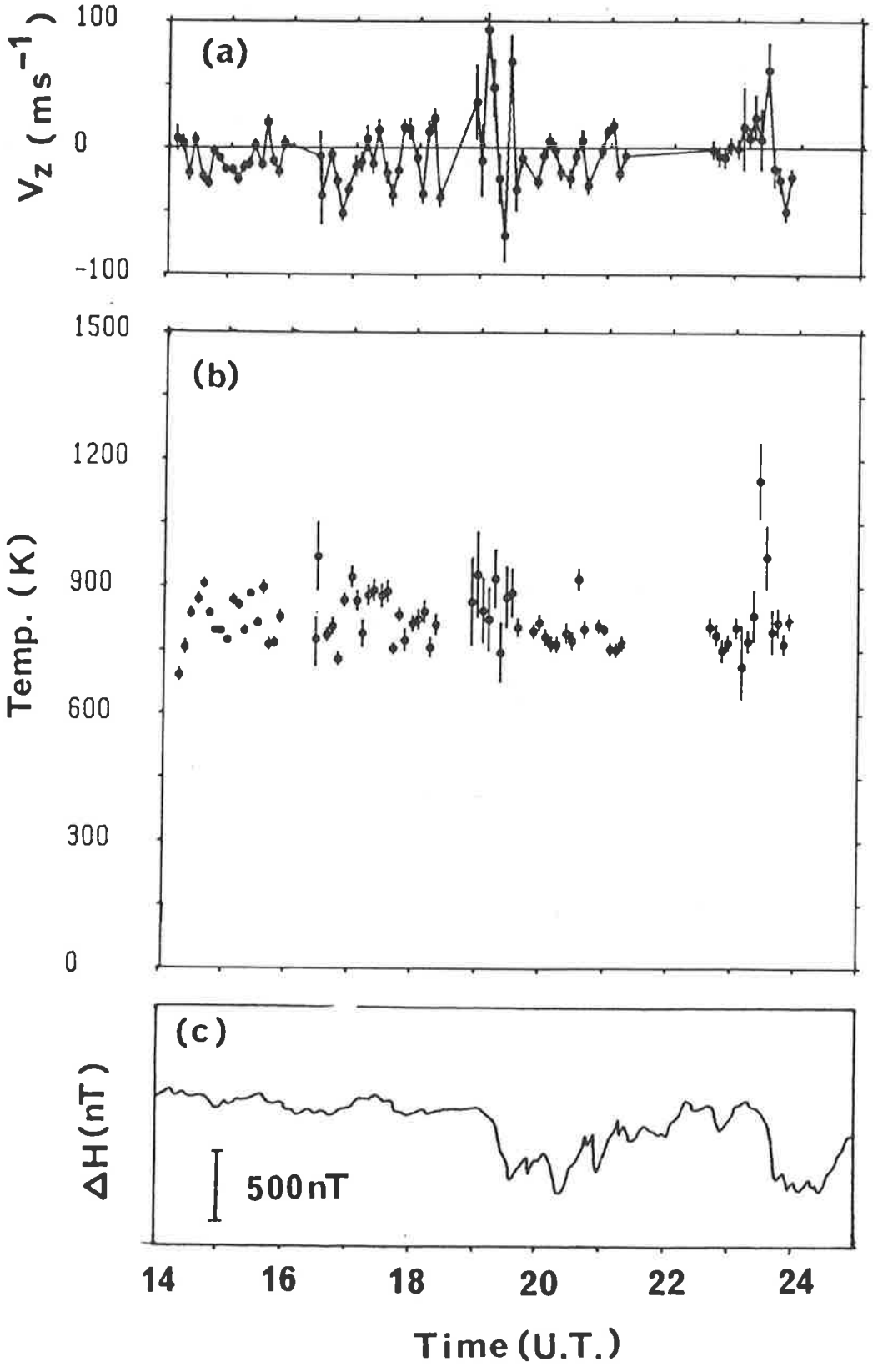

Figure 7.11 (a) vertical wind, (b) temperature and (c) H-component of the local magnetogram observed on September 19, 1983.

responded by expanding rapidly upwards, reaching a maximum velocity of $100ms^{-1}$. The upward motion was sustained for 30 minutes and was then replaced by oscillations of small amplitude and a period of ~30 minutes. The temperature data show no clear evidence of local heating.

7.5.3 Discussion

To date, there have been relatively few measurements of vertical motions in the neutral thermosphere. Rieger (1974) has reported motions of $15ms^{-1}$ at low, medium and high latitudes, observed in barium release experiments, and Spencer et al. (1976), using a mass spectrometer aboard the Atmosphere Explorer-C spacecraft, have observed vertical winds up to $80ms^{-1}$ near the auroral oval during disturbed geomagnetic conditions. Subsequent observations have shown that strong ($>50ms^{-1}$) vertical winds are a common feature of the high-latitude thermosphere during both quiet and disturbed conditions (Spencer et al. 1982; Rees et al 1984a). In particular, the vertical wind shows a large, rapid and complex response to localised, impulsive energy input associated with auroral substorms.

The results of the present study confirm the general conclusions stated above. Oscillatory motions of large amplitude were observed on all nights and were consistent with thermospheric gravity waves. The present data base is strongly biased towards disturbed geomagnetic conditions; however, the results of July 20 indicate that large vertical motions may also occur during extremely quiet conditions.

If a localised heat source is applied to the lower thermosphere expansion will occur and upward motion is to be expected at all levels above the source. Thermospheric models have confirmed and extended this picture (Mayr et al. 1984a,b). Calculations indicate that the thermosphere responds rapidly to localised heating. The largest

perturbations occur above the source, where the wind is chiefly upward. As the source is turned on or off oscillations occur and thermospheric gravity waves are generated which redistribute geomagnetic energy globally. Outside the source region the behaviour is more complex and is dominated by oscillations.

The data from April 13, May 24 and September 19 are in substantial agreement with the model predictions and with observations in the northern hemisphere (Rees et al. 1984a). The most striking feature is the extremely rapid and complex response of the thermosphere to impulsive energy input associated with auroral substorms. This is particularly evident on May 24 and September 19, when strong upward winds occurred in direct response to geomagnetic energy input. On April 13, the disturbance commenced during a pre-existing period of upward wind and the thermospheric response is less obvious.

The calculations of Rees et al., (1984b) indicate downward winds of 30-80ms^{-1} which act as a significant local energy source outside the principal source region following the end of the disturbance. This is confirmed by the results of April 13 where strong downward winds of up to 100ms^{-1} occur from 0030 to 0100 UT and are accompanied by a temperature increase of ~450K. Also, on May 24, prolonged periods of downward wind from 1820 to 1930 and 2140 to 2220 UT are accompanied by temperature increases of ~200K. These temperature perturbations are delayed by 1-2 hours relative to the onset of the geomagnetic disturbances and are therefore not attributable to direct heating from auroral sources. The results suggest that the vertical wind plays a significant role in the redistribution of geomagnetic energy.

7.6 Horizontal Divergence of the Wind Field

The measurements of the horizontal wind field revealed an interesting problem which remains outstanding. The problem relates to large horizontal divergence of the wind field which is apparent in the individual wind measurements made in the four cardinal directions.

Figure 7.12 shows the averages of the half-hourly samples for $A_p<25$. The measurements of the geographic meridional component made to the north and to the south are shown in Figure 7.12a and the zonal measurements in Figure 7.12b. Horizontal gradients of several hundreds of metres per second were observed in both components. The observing geometry is illustrated in Figure 7.13a which shows that measurements made to the north and to the south are separated by a horizontal distance of ~800km, as are measurements to the east and west. The horizontal gradients in both meridional and zonal directions therefore amount to $\sim 0.2 ms^{-1}/km$. Figure 7.13b indicates the average location of the auroral electrojet. The electrojet is oriented approximately in the geographic northeast to southwest direction and its position with respect to Mawson varies both with UT and with geomagnetic activity. The average position is close to Mawson's zenith.

It is clear that a divergent 'line-source' of velocity, associated with the electrojet, could account qualitatively for the observed horizontal divergence. This idea will now be developed further; it must be pointed out however, that the following discussion is necessarily speculative due to the incomplete nature of the available data.

It has been well established that the auroral zones are important sources of thermospheric gravity waves resulting from Joule and particle heating in the lower thermosphere. The propagation of these waves at middle and low latitudes has been studied extensively and is

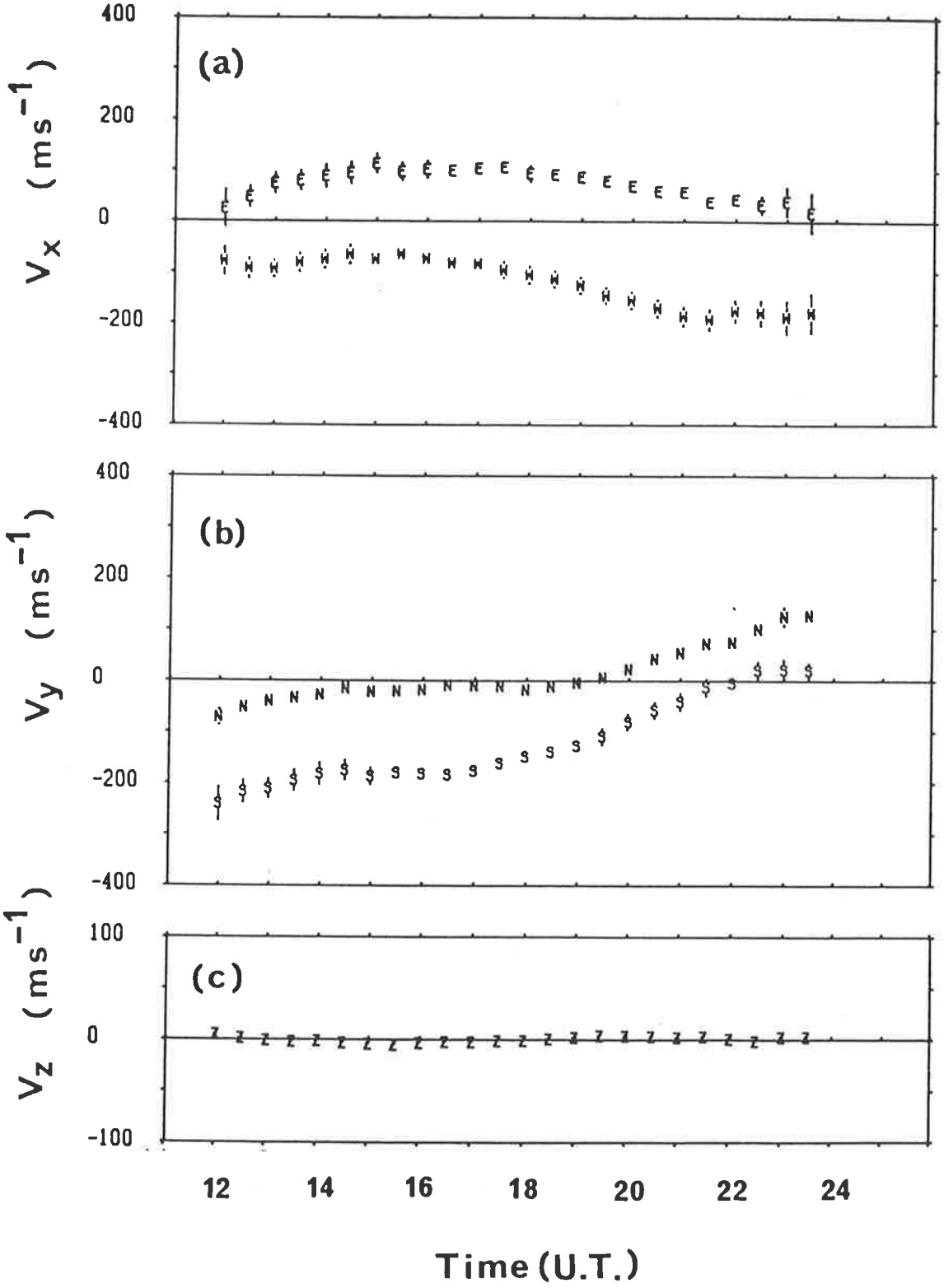

Figure 7.12 Averages of (a) zonal, (b) meridional and (c) vertical wind observations obtained under quiet to moderate geomagnetic conditions (A_p<25), and shown as functions of universal time. The symbols N,E,S,W,Z indicate the geographic direction of observation. Error bars are shown wherever they exceed the height of the symbols.

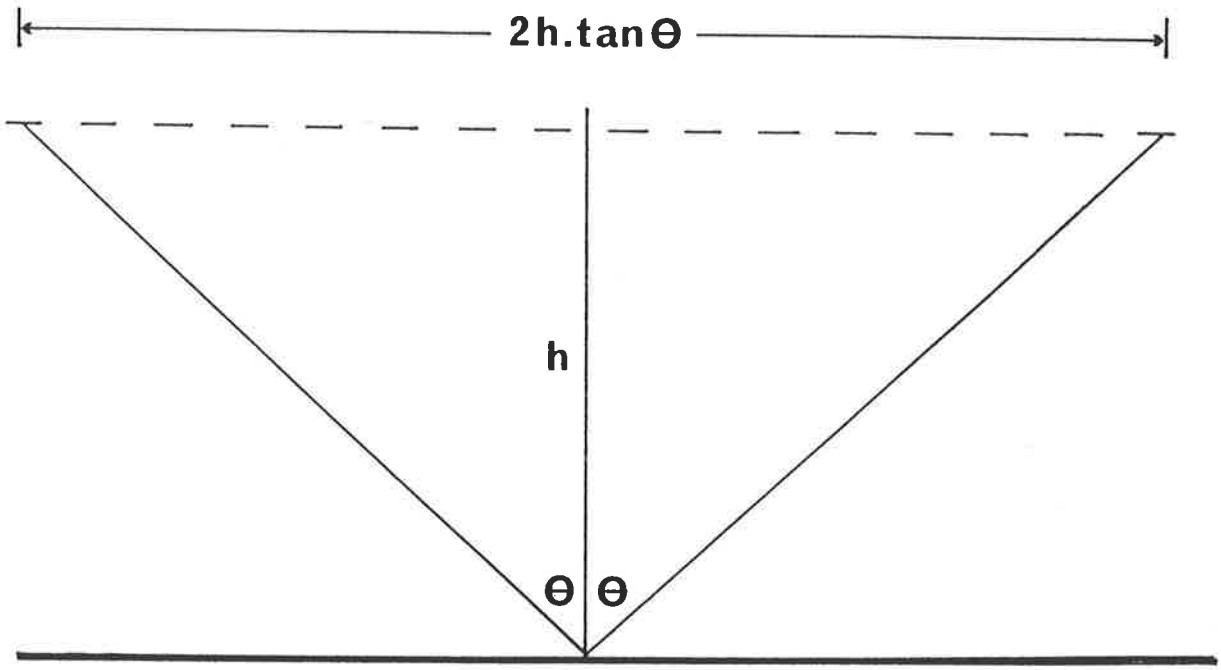

Figure 7.13 (a) observing geometry in section; the earth's surface (assumed flat) is indicated by the heavy horizontal line, h is the height of the emitting layer and θ is the zenith angle of the observation. Observations made to the north and south are thus separated by a horizontal distance of $2h.\tan\theta$, as are observations to the east and west.

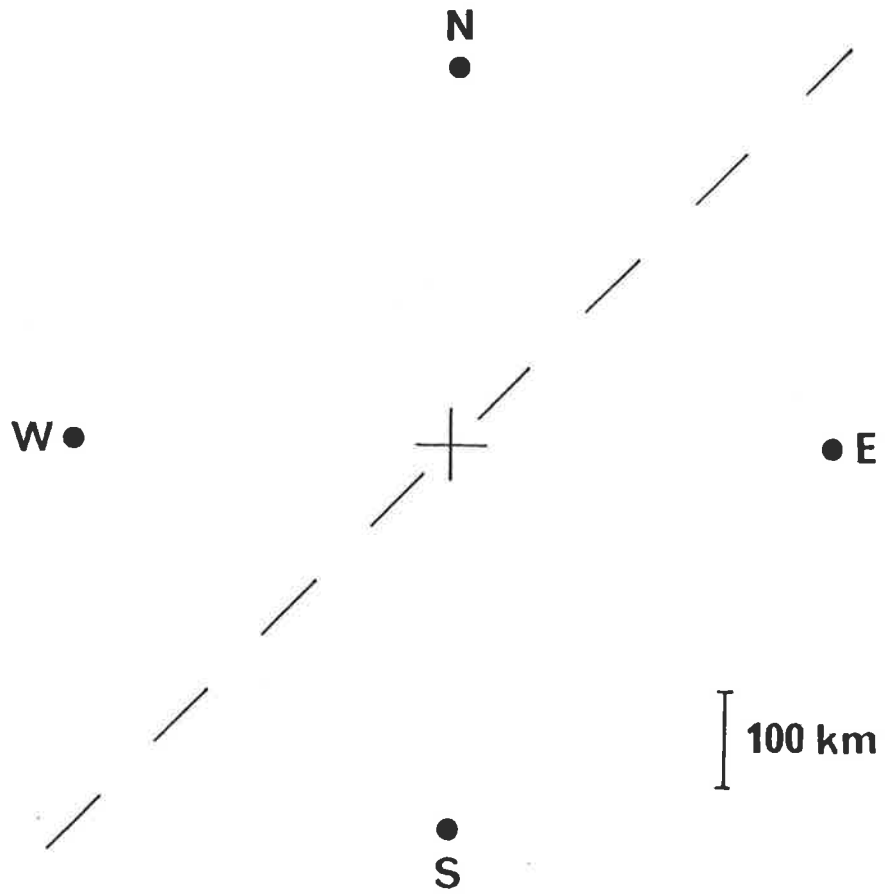

Figure 7.13 (b) observing geometry in plan view; Mawson is indicated by the central cross, the points labelled N,E,S,W indicate the position of observations made to the geographic north, east, south and west. The approximate average location of the auroral electrojet is indicated by the broken line.

reviewed by Francis (1975). Recent observations, made within the auroral zones, have revealed vertical motions in excess of $100ms^{-1}$ and have demonstrated considerable wave activity even during relatively quiet geomagnetic conditions. These observations have been discussed in section 7.5.

The results presented in section 7.5 suggest that oscillations in the vertical component of the wind velocity are frequently present during quiet to moderate conditions, with amplitudes of $\sim 25ms^{-1}$ and periods in the range 20 to 60 minutes. It is proposed that the observed divergent flow is driven by momentum deposition resulting from the dissipation of gravity waves generated in the vicinity of the auroral electrojet.

The acceleration of the background flow resulting from wave dissipation may be estimated from the measured wave parameters. We note that propagating gravity waves transport horizontal momentum, the vertical flux of which is given by (Hines 1960, 1972)

$$F_{xz} = \rho w_0^2 \tau / \tau_g$$

where ρ is the atmospheric density, w_0 the amplitude of the vertical velocity oscillation, τ the wave period and τ_g the Vaisala-Brunt period. In the absence of dissipation F_{xz} is independent of height and the exponential decrease of ρ with height is compensated by an increase in w_0. This process is however limited by the high kinematic viscosity of the upper thermosphere; dissipation results and the wave energy and momentum are transferred to the background atmosphere. Midlatitude studies have found wave amplitudes to be independent of height above ~250km (Testud 1970). Under such conditions the acceleration of the background flow is given by

$$dU/dt = w_0^2 \tau / 2 \tau_g H$$

where H is the atmospheric scale height.

In the 200-300km region we may take τ_g~15 minutes and H~50km. The vertical wind measurements suggest that w_0~25ms^{-1} and τ~45 minutes are typical values of the wave parameters. Inserting these values into the above equation yields a horizontal acceleration of 0.02ms^{-2}. This is comparable to typical Coriolis accelerations and perhaps a factor of two lower than ion drag acceleration in this region of the atmosphere (Hays et al. 1979). The observed divergence is therefore qualitatively consistent with the results expected from a line source of velocity, which is identified with momentum deposition resulting from dissipating gravity waves, generated within the auroral electrojet.

Further study is definitely required in order to expand on the above statement. The most important requirement is to reduce the time resolution of the observations to a few minutes, thus permitting both the horizontal wind field and the detailed behaviour of the vertical component to be obtained. This would allow changes in divergence to be related more directly to wave activity. The new generation of imaging Fabry-Perot spectrometers is capable of such measurements and should allow significant improvement over the preliminary results presented here.

Chapter 8

CONCLUSIONS

8.1 Summary of Results

The observations confirm that at high latitudes, the neutral thermosphere is driven principally by momentum transfer from convecting ions. This conclusion is in agreement with ground-based observations from the northern hemisphere, with satellite observations and with the predictions of thermospheric general circulation models.

The observed winds followed the pattern of ion convection resulting from electric fields of magnetospheric origin. The wind direction was sunward in the afternoon and evening hours, changing to antisunward around magnetic midnight. Both the averaged winds and the results from individual nights followed this basic pattern. During disturbed geomagnetic conditions the wind speeds were increased but wind directions remained largely unchanged. Observed temperatures were in the range 600-800K during quiet to moderate geomagnetic conditions (A_p<25) and reached up to 1200K during disturbed conditions. A broad minimum in temperature at around 1600UT was noted.

Further examination of the wind data revealed a stong dependence on the y-component of the interplanetary magnetic field (IMF B_y) as measured by the IMP-8 spacecraft. For IMF B_y negative, the geomagnetic zonal component of the averaged wind vectors was westward from ~1800-0200MLT. For IMF B_y positive the zonal component shifted from westward to eastward at ~2200MLT. The dependence of IMF B_y was therefore especially pronounced around magnetic midnight. This phenomenon may be

explained by reference to the known relationship between IMF B_y and the geometry of the polar ion convection pattern. For IMF B_y negative, the dusk convection cell becomes enlarged in the southern hemisphere, while for IMF B_y positive the dawn cell is enlarged. The enlarged cell strongly influences the neutral circulation across the polar cap and in the magnetic midnight region of the auroral oval, in agreement with the observations.

The observed winds were compared with the output of a thermospheric general circulation model developed at University College, London. Two model runs were considered: one for IMF B_y negative and another for IMF B_y positive. In both cases good agreement was obtained between model and observed wind directions although the model wind speeds were generally larger than those observed. This discrepancy was attributed to the fact that high solar activity was assumed for the model simulations. The model results suggested that the dusk convection cell is usually more prominent than the dawn cell, since the associated anticyclonic flow is effectively assisted by the Coriolis force.

Observations of the vertical component of the wind revealed large oscillatory motions consistent with the presence of thermospheric gravity waves. Amplitudes were typically greater than $20ms^{-1}$ and periods were in the range 20-60 minutes. These oscillations were observed during both quiet and disturbed geomagnetic conditions. The oscillations were consistent with the presence of thermospheric gravity waves, resulting from Joule heating in the vicinity of the auroral electrojet. The response of the vertical wind to impulsive heating events associated with auroral substorms was extremely rapid, with upward motions of $100ms^{-1}$ developing on time scales of 5-10

minutes. Periods of strong downward motion were found to coincide with temperature increases of up to 200K. The results suggest that thermospheric gravity waves of large amplitude are a common feature of the high-latitude thermosphere and that they may play an important role in the redistribution of geomagnetic energy.

On most nights, large divergences were apparent in the horizontal wind observations. It is speculated that the divergent flow results from the dissipation of gravity waves, generated along the auroral electrojet. Simple calculations support this hypothesis but further study is required in this area (see next section).

8.2 Problems and Recommendations

A number of problems were identified during the course of this work. Most of these relate to the Fabry-Perot spectrometer, the associated facilities at Mawson and the difficulties inherent in conducting science in the Antarctic. These will now be briefly summarised.

The time resolution of the observations is limited by the intensity of the 630nm emission and by the throughput of the spectrometer. For all observations except the vertical wind measurements of section 7.5, signal integration continued until a preset total count was achieved. This resulted in integration times of typically ~20 minutes. A complete observing cycle over north, east, south, west and zenith thus required ~100 minutes. This was too long to permit identification of gravity wave fluctuations in the horizontal and vertical components of the wind. For the vertical wind measurements of section 7.5, integration time was fixed at ~6 minutes to ensure that fluctuations down to the Väisälä-Brunt period (~15

minutes) could be detected. This reduced integration time yielded results which were acceptable except when the 630nm emission was extremely weak.

It appears, therefore, that the time resolution of the horizontal wind observations could have been improved by a factor of two or more. Unfortunately, this conclusion was not reached until the author returned to Australia, since the limited computing facilities at Mawson permitted only a cursory examination of the data. The results have at least provided information allowing the time resolution and statistical error of subsequent observations to be better optimised.

The lack of computing facilities was a serious problem in two respects: firstly, as illustrated above, the inability to analyse data on site meant that certain difficulties could not be identified until the observing program (of almost one year's duration) was completed. Secondly, considerable time was wasted since the development of analysis programs, analysis of data and interpretation of results could not commence until the author's return to Australia.

It is unlikely that a suitable computing system will be available at Mawson in the near future. However, the above problems can now be overcome by use of a recently installed satellite communication link between Mawson and Australia. It is recommended that raw data be transferred to Australia on a weekly basis for immediate analysis. This procedure would be cheap, relatively simple and would dramatically reduce the lead-time between observation and publication of results.

A further problem concerned the lack of instrument automation. During the course of these observations the instrument required constant operator attention in order to position the periscope,

initiate scanning, monitor the integrated signal, cease scanning when appropriate and record the data. In addition, the wavelength calibration source had to be inserted into the optical path and calibration scans performed at frequent intervals. During winter the instrument had the potential to operate continuously for many days (cloud permitting) but this was impossible for a single operator to achieve.

This problem has since been addressed and during 1984 the instrument control software was upgraded to permit automated operation. The present configuration permits observations over a preset cycle of periscope positions, with sky observations and wavelength calibrations alternating. Operator attention is only required every 10 hours, in order to change the data tape.

The lack of a zero-velocity reference is a minor problem and the assumptions outlined in section 6.6 are unlikely to lead to significant systematic error. The Mawson Institute, in collaboration with the Physics Department of the University of Adelaide has developed an oxygen discharge lamp which produces both the 558nm and 630nm emissions. Unfortunately, the lamp requires refilling after a few months and is not as yet suitable for service in the Antarctic.

The suitability of the instrument for daytime observations must be questioned. The author's attempts to isolate the daytime 630nm emission from the background of scattered sunlight were unsuccessful. Even after 90 minutes of signal integration, the extracted feature was extremely weak and in most cases was so distorted as to make wind and temperature analysis impossible. Work is continuing on this problem, using the Mawson instrument and a prototype of that instrument installed at Mt Torrens, near Adelaide.

Finally, the usefulness of the Fabry-Perot spectrometer would be improved by coordinating observations with the other two instruments used for atmospheric research at Mawson. The first of these is a photometer used to record fluctuations in the intensity of airglow and auroral emissions over three spaced fields of view. The instrument is essentially three independent photometers which share the same collection optics and is described by Jacob (1985). Correlation analysis of the records from the three fields yields estimates of the period and horizontal phase velocity of gravity waves at the height of emission. An identical instrument, installed at Mt Torrens, has been used to investigate the generation of gravity waves within the troposphere. The Mawson instrument was operated during 1981 but noise associated with auroral emissions made analysis of the data impossible. It is hoped that during solar minimum conditions the instrument will yield useful information concerning gravity waves in the mesosphere and thermosphere.

The second instrument is a radar used to measure horizontal wind velocities in the 60-100km region. Radio waves of frequency 1.94MHz are transmitted vertically upward and are partially reflected by irregularities in the atmospheric refractive index. The reflected waves form a diffraction pattern which moves across the ground at twice the velocity of the irregularities. This pattern is sampled by three spaced antennas whose outputs are analysed to obtain the horizontal wind velocity as a function of height. The instrument is described in detail by Macleod (1986).

Clearly, coordination of all three instruments is desirable, especially in regard to the questions raised in section 7.6. Furthermore, it is proposed that a LIDAR system be installed at Mawson

within the next few years (Jacka, 1987). This instrument will provide wind and temperature information over the altitude range 5–70km (Jacka and Argall, 1987). The combination of all of these instruments with conventional meteorological techniques would constitute an extremely powerful tool for probing the Antarctic atmosphere from the ground to 300km altitude.

REFERENCES

Akasofu, S-I. (1977), Physics of Magnetospheric Substorms, *Astrophysics and Space Science Library*, Vol. 47, D. Reidel.

Amayenc, P. (1974), Tidal oscillations of the meridional neutral wind at midlatitudes, *Radio Sci.*, 9, 281.

Armstrong, E.B. (1969), Doppler shifts in the wavelength of the OI λ6300Å line in the night airglow, *Planet. Space Sci.*, 17, 957.

Ballik, E.A. (1966), The response of scanning Fabry-Perot interferometers to atomic transition profiles, *Appl. Opt.*, 5, 170.

Barmore, F.E. (1972), A high resolution study of the 6300Å oxygen line in the day airglow, *Ph.D. Thesis*, University of Wisconsin.

Barmore, F.E. (1975), The filling in of Fraunhofer lines in the day sky, *J. Atmos. Sci.*, 32, 1489.

Bens, A.R., L.L. Cogger and G.G. Shepherd (1965), Upper atmospheric temperatures from Doppler line widths: 3. Observation of the OI dayglow emission at 6300Å, *Planet. Space Sci.*, 13, 551.

Bevington, P.R. (1969), Data Reduction and Error Analysis for the Physical Sciences, McGraw-Hill.

Born, M., and E. Wolf (1970), Principles of Optics, 3rd Ed., Pergamon.

Buisson, H., and C. Fabry (1912), Width of spectral lines, *J. Phys.*, 11, 442.

Burke, W.J., M.C. Kelley, R.C. Sagalyn, M. Smiddy and S.T. Lai (1979), Polar cap electric field structures with a northward interplanetary magnetic field, *Geophys. Res. Lett.*, 6, 21.

Chabbal, R. (1953), *J. Rech. Cent. Natl. Rech. Sci. Lab. Bellevue (Paris)*, 5, 138. English translation: Research on the best conditions for using a Fabry-Perot photoelectric spectrometer, A.E.R.E. Lab./Trans. 778, Harwell, U,K.

Chabbal, R. (1958), Recherches expérimentales et théoretiques sur la généralisation de l'emploi du spectromètre Fabry-Perot aux divers domaines de la spectroscopie, *Rev. Opt.*, 37, 49.

Chapman, S. (1931), The absorption and dissociative or ionising effect of monochromatic radiation in an atmosphere on a rotating earth, *Proc. phys. Soc.*, 43, 26.

Ching, B.K. and Y.T. Chiu (1973), A phenomenological model of global ionospheric electron density in the E, F1 and F2 regions, *J. Atmos. Terr. Phys.*, 35, 1615.

CIRA (1965), International Council of Scientific Unions, Committee on Space Research, COSPAR International Reference Atmosphere, North Holland, Amsterdam.

Cocks, T.D. (1977), High spectral resolution studies of the atomic oxygen λ630nm dayglow, *Ph.D. Thesis*, University of Adelaide, South Australia.

Cocks, T.D. and F. Jacka (1979), Daytime thermospheric temperatures, wind velocities and emission intensities derived from ground-based observations of the OI λ630nm airglow line profile, *J. Atmos. Terr. Phys.*, 41, 409.

Cocks, T.D., D.F. Creighton and F. Jacka (1980), Application of a dual Fabry-Perot spectrometer for daytime airglow studies, *J. Atmos. Terr. Phys.*, 42, 499.

Cole, K.D. (1962), Joule heating of the upper atmosphere, *Aust. J. Phys.*, 15, 223.

Cole, K.D. (1971), Electrodynamic heating and movement of the thermosphere, *Planet. Space Sci.*, 19, 59.

Daehler, M. and F.L. Roesler (1968), High contrast in a polyetalon Fabry-Perot spectrometer, *Appl. Opt.*, 7, 1240.

Delbouille, L., L. Neven and G. Roland (1973), Photometric atlas of the solar spectrum from λ3000Å to λ10000Å, Institut d'Astrophysique de l'Université de Liege, Cointe-Ougrée.

Dickinson, R.E. (1975), Meteorology of the upper atmosphere, *Rev. Geophys. Space Phys.*, 13, 771.

Dickinson, R.E. and H. Rishbeth (1973), Planetary scale motions at F-layer heights, *Space Res.*, 13, 413.

Dickinson, R.E., E.C. Ridley and R.G. Roble (1975), Meridional circulation in the thermosphere, I. Equinox condtions, *J. Atmos. Sci.*, 32, 1737.

Dickinson, R.E., E.C. Ridley and R.G. Roble (1977), Meridional circulation in the thermosphere, II. Solstice condtions, *J. Atmos. Sci.*, 34, 178.

Dickinson, R.E., E.C. Ridley and R.G. Roble (1981), A three-dimensional general circulation model of the thermosphere, *J. Geophys. Res.*, 86, 1499.

Dungey, J.W. (1961), Interplanetary magnetic field and the auroral zones, *Phys. Rev. Lett.*, 6, 47.

Dungey, J.W. (1963), The structure of the exosphere, or adventures in velocity space, in 'Geophysics', DeWitt et al. (eds.), Gordon and Breach.

Fedder, J.A. and P.M. Banks (1972), Convection electric fields and polar thermospheric winds, *J. Geophys. Res.*, 77, 2328.

Francis, S.H. (1975), Global propagation of atmospheric gravity waves : A review, *J. Atmos. Terr. Phys.*, 37, 1011.

Fuller-Rowell, T.J. and D. Rees (1980), A three-dimensional, time-dependent, global model of the thermosphere, *J. Atmos. Sci.*, 37, 2545.

Fuller-Rowell, T.J. and D. Rees (1981), A three-dimensional, time-dependent simulation of the global dynamical response of the thermosphere to a geomagnetic substorm, *J. Atmos. Terr. Phys.*, 43, 701.

Geisler, J.E. (1967), A numerical study of the wind system in the middle thermosphere, *J. Atmos. Terr. Phys.*, 29, 1469.

Grainger, J.F. and J. Ring (1962), Anomalous Fraunhofer line profiles, *Nature*, 193, 762.

Hays, P.B. and R.G. Roble (1971), Direct observations of thermospheric winds during geomagnetic storms, *J. Geophys. Res.*, 76, 5316.

Hays, P.B., D.W. Rusch, R.G. Roble and J.C.G. Walker (1978), The OI (6300Å) airglow, *Rev. Geophys. Space Phys.*, 16, 225.

Hays, P.B., J.W. Meriwether and R.G. Róble (1979), Nighttime thermospheric winds at high latitudes, *J. Geophys. Res.*, 84, 1905.

Hays, P.B., T.L. Killeen and B.C. Kennedy (1981), The Fabry-Perot interferometer on Dynamics Explorer, Space Sci. Instrum., 5, 395.

Hays, P.B., T.L. Killeen, N.W. Spencer, L.E. Wharton, R.G. Roble, B.A. Emery, T.J. Fuller-Rowell, D. Rees, L.A. Frank and J.D. Craven (1984), Observations of the dynamics of the polar thermosphere, *J. Geophys. Res.*, 89, 5597.

Heaps, M.G. and L.R. Megill (1975), Circulation in the high-latitude thermosphere due to electric fields and Joule heating, *J. Geophys. Res.*, 80, 1829.

Hedin, A.E., H.G. Mayr, C.A. Reber, N.W. Spencer and G.R. Carignan (1974), Empirical model of global thermospheric temperature and composition based on data from the OGO-6 quadrupole mass spectrometer, *J. Geophys. Res.*, 79, 215.

Heelis, R.A., J.K. Lowell and R.W. Spiro (1982), A model of the high-latitude ionospheric convection pattern, *J. Geophys. Res.*, 87, 6339.

Heppner, J.P. (1972), Polar cap electric field distributions related to the interplanetary magnetic field direction, *J. Geophys. Res.*, 77, 4877.

Heppner, J.P. (1977), Empirical models of high-latitude electric fields, *J. Geophys. Res.*, 82, 1115.

Heppner, J.P. and M.L. Miller (1982), Thermospheric winds at high latitudes from chemical release observations, *J. Geophys. Res.*, 87, 1633.

Heppner, J.P. and N.C. Maynard (1983), High-latitude electric field models, Paper presented at the Chapman Conference on Magnetospheric Currents, AGU, Irvington, Va., April 5-8, 1983.

Heppner, J.P. and N.C. Maynard (1986), Empirical, high-latitude electric field models, (submitted to *J. Geophys. Res.*).

Hernandez, G. (1966), Analytical description of a Fabry-Perot spectrometer, *Appl. Opt.*, 5,1745.

Hernandez, G. (1970), Analytical description of a Fabry-Perot photoelectric spectrometer. 2: Numerical results, *Appl. Opt.*, 7, 1591.

Hernandez, G. (1978), Analytical description of a Fabry-Perot spectrometer. 4: Signal noise limitations in data retrieval; winds, temperatures, and emission rates., *Appl. Opt.*, 17, 2967.

Hernandez, G. (1982), Vertical motions of the neutral thermosphere at midlatitude, *Geophys. Res. Lett.*, 9, 555.

Hernadez, G., T.E. Van Zandt, V.L. Peterson and J.P. Turtle (1975), Comparison of optical and incoherent scatter measurements of exospheric temperature at the magnetic equator, *J. Geophys. Res.*, 80, 3271.

Hernandez, G. and R.G. Roble (1976), Direct measurements of nighttime thermospheric winds and temperatures, 1. Seasonal variations during geomagnetic quiet periods, *J. Geophys. Res.*, 81, 2065.

Hernandez, G. and R.G. Roble (1976), Direct measurements of nighttime thermospheric winds and temperatures, 2. Geomagnetic storms, *J. Geophys. Res.*, 81, 5173.

Hernandez, G. and R.G. Roble (1977), Direct measurements of nighttime thermospheric winds and temperatures, 3. Monthly variations during solar minimum, *J. Geophys. Res.*, 82, 5505.

Hernandez, G. and R.G. Roble (1978), Observations of large-scale thermospheric gravity waves during geomagnetic storms, *J. Geophys. Res.*, 83, 5531.

Hernandez, G., O.A. Mills and J.A. Smith (1981), TESS: A high-luminosity high resolution twin-etalon scanning spectrometer, *Appl. Opt.*, 20, 3687.

Herrero, F.A., H.G. Mayr, I. Harris amd F. Varosi (1984), Thermospheric gravity waves near the source: Comparison of variations in neutral temperature and vertical velocity at Sondre Stromfjord, *Geophys. Res. Lett.*, 11, 939.

Hill, R.M. (1963), Some fringe-broadening defects in a Fabry-Perot etalon, *Opt. Acta*, 10, 141.

Hines, C.O. (1960), Internal atmospheric gravity waves at ionospheric heights, *Can. J. Phys.*, 38, 1441.

Hines, C.O. (1972), Momentum deposition by atmospheric waves and its effect on thermospheric circulation, *Space Research*, 12, 1157.

Hinteregger, H.E. (1970), The extreme ultraviolet solar spectrum and its variation during a solar cycle, *Ann. Géophys.*, 26, 547.

Hinteregger, H.E. (1976), EUV fluxes in the solar spectrum below 2000Å, *J. Atmos. Terr. Phys.*, 38, 791.

Hoffman, R.A. and E.R. Schmerling (1981), Dynamics Explorer program: An overview, *Space Sci. Instrum.*, 5, 345.

Jacchia, L.G. (1965), Static diffusion models of the upper atmosphere with empirical temperature profiles, *Smithson. Contrib. Astrophys.*, 8, 215.

Jacchia, L.G. (1971), Revised static models of the thermosphere and exosphere with empirical temperature profiles, *Spec. Rep. 332*, Smithson. Astrophys. Observ., Cambridge, Mass.

Jacka, F., A.R.D. Bower, D.F. Creighton and P.A. Wilsch (1980), A large-aperture, high-resolution Fabry-Perot spectrometer for airglow studies, *J. Phys. E: Sci. Instrum.*, 13, 562.

Jacka, F. (1987), A proposal for study of the dynamics, energetics and chemistry of the stratosphere over Mawson, Antarctica, in 'Australian Upper Atmospheric and Space Physics Research in Antarctica, 1987', G.B. Burns and M. Craven (eds.), ANARE Research Notes, Vol. 48, 1987.

Jacka, F. and P.S. Argall (1987), A LIDAR system for stratospheric studies - performance simulation, in 'Australian Upper Atmospheric and Space Physics Research in Antarctica, 1987', G.B. Burns and M. Craven (eds.), ANARE Research Notes, Vol. 48, 1987.

Jacob, P.G. (1985), Manifestations of atmospheric gravity waves in the airglow at 95km, *Ph.D. Thesis*, University of Adelaide, South Australia.

Jacquinot, P. (1954), The luminosity of spectrometers with prisms, gratings or Fabry-Perot etalons, *J. Opt. Sci. Am.*, 44, 761.

Jacquinot, P. (1960), New developments in interference spectroscopy, *Rep. Prog. Phys.*, 23, 267.

Jenkins, F.A. and H.A. White (1981), Fundamentals of Optics, 4th Ed., McGraw-Hill.

Kattawar G.W., A.T. Young and T.J. Humphreys (1981), The Ring effect without aerosols, *Astrophys. J.*, 243, 1049.

Kent, G.S. (1970), Measurement of ionospheric movements, *Rev. Geophys. Space Phys.*, 8, 229.

Killeen, T.L., P.B. Hays, N.W. Spencer and L.E. Wharton (1982), Neutral winds in the polar thermosphere as measured from Dynamics Explorer, *Geophys. Res. Lett.*, 9, 957.

Killeen, T.L., P.B. Hays, N.W. Spencer and L.E. Wharton (1983), Neutral winds in the polar thermosphere as measured from Dynamics Explorer, *Adv. Space. Res.*, 2, 133.

Killeen, T.L., R.W. Smith, P.B. Hays, N.W. Spencer, L.E. Wharton and F.G. McCormac (1984), Neutral winds in the high latitude winter F-region: Coordinated observations from ground and space, *Geophys. Res. Lett.*, 11, 311.

Kohl, H. and J.W. King (1967), Atmospheric winds between 100 and 700km and their effects on the ionosphere, *J. Atmos. Terr. Phys.*, 29, 1045.

Mack, J.E., D.F. McNutt, F.L. Roesler and R. Chabbal (1963), The PEPSIOS purely interferometric high-resolution scanning spectrometer. I. The pilot model, *Appl. Opt.*, 2, 873.

Macleod, R.I. (1986), Dynamics of the antarctic mesopause, *Ph.D. Thesis*, University of Adelaide, South Australia.

Maynard, N.C. (1974), Electric field measurements across the Harang discontinuity, *J. Geophys. Res.*, 79, 4620.

Mayr, H.G. and H. Volland (1971), Semiannual variations in the neutral composition, *Ann. Géophys.*, 27, 513.

Mayr, H.G. and H. Volland (1972), Theoretical model for the latitude dependence of the annual and semiannual variations, *J. Geophys. Res.*, 77, 6774.

McCormac, F.G. and R.W. Smith (1984), The influence of the interplanetary magnetic field Y component on ion and neutral motions in the polar thermosphere, *Geophys. Res. Lett.*, 11, 935.

McCormac, F.G., T.L. Killeen, E. Gombosi, P.B. Hays and N.W. Spencer (1985), Configuration of the high-latitude thermosphere neutral circulation for IMF B_y negative and positive, *Geophys. Res.* Lett., 12, 155.

McNutt, D.P (1965), PEPSIOS purely interferometric high-resolution scanning spectrometer. II. Theory of spacer ratios, *J. Opt. Soc. Am.*, 55, 288.

Meriwether, J.W., J.P. Heppner, J.D. Stolarik and E.M. Wescott (1973), Neutral winds above 200km at high latitudes, *J. Geophys. Res.*, 78, 6643.

Miller, R.E. and W.G. Fastie (1972), Skylight intensity, polarisation and airglow measurements during the total solar eclipse of 30 May, 1965, *J. Atmos. Terr. Phys.*, 34, 1541.

Murayama, T. (1974), Origin of the semiannual variation of geomagnetic K_p indices, *J. Geophys. Res.*, 79, 2997.

Nagy, A.F., R.J. Cicerone, P.B. Hays, K.D. McWatters, J.W. Meriwether, A.E. Belon and C.L. Rino (1974), Simultaneous measurement of ion and neutral motions by radar and optical techniques, *Radio Sci.*, 9, 315.

Noxon, J.F. and R.M. Goody (1962), Observation of day airglow emission, *J. Atmos. Sci.*, 19, 342.

Noxon, J.F. (1964), A study of the 6300Å oxygen line in the day airglow, *J. Geophys. Res.*, 69, 3245.

Potemra, T.A., L.J. Zanetti, P.F. Bythrow, A.T.Y. Lui and T. Iijima (1984), B_y-dependent convection patterns during northward interplanetary magnetic field, *J. Geophys. Res.*, 89, 9753.

Ramsay, J.V. (1962), A rapid-scanning Fabry-Perot interferometer with automatic parallelism control, *Appl. Opt.*, 1, 411.

Ratcliffe, J.A. (1972), An Introduction to the Ionosphere and Magnetosphere, Cambridge University Press.

Rees, D. (1971), Ionospheric winds in the auroral zone, *J. Brit. Interplan. Soc.*, 24, 233.

Rees, D. (1973), Neutral wind structure in the thermosphere during quiet abd disturbed geomagnetic periods, in 'Physics and Chemistry of Upper Atmospheres', ed. McCormac, B.M., D. Reidel.

Rees, D., T.J. Fuller-Rowell and R.W. Smith (1980), Measurements of high-latitude thermospheric winds by rocket and ground-based techniques and their interpretation using a three-dimensional time-dependent dynamical model, *Planet. Space Sci.*, 28, 919.

Rees, D., R.W. Smith, P.J. Charleton, F.G. McCormac, N. Lloyd and Å. Steen (1984a), The generation of vertical thermospheric winds and gravity waves at auroral latitudes - I. Observations of vertical winds, *Planet. Space Sci.*, 32, 667.

Rees, D., M.F. Smith, and R. Gordon (1984b),The generation of vertical thermospheric winds and gravity waves at auroral latitudes - II. Theory and numerical modelling of vertical winds, *Planet. Space Sci.*, 32, 685.

Rees, D., T.J. Fuller-Rowell, M.F. Smith, R. Gordon, T.L. Killeen, P.B. Hays, N.W. Spencer, L.E. Wharton, and N.C. Maynard (1985), The westward thermospheric jet stream of the evening auroral oval, *Planet. Space Sci.*, 33, 425.

Rees, D., R. Gordon, T.J. Fuller-Rowell, M.F. Smith, G.R. Carignan, T.L. Killeen, P.B. Hays and N.W. Spencer (1985), The composition, structure, temperature and dynamics of the upper thermosphere in the polar regions during October to December, 1981, *Planet. Space Sci.*, 33, 617.

Rees, D., P. Charleton, M. Carlson and P. Rounce (1985), High-latitude thermospheric circulation during the Energy Budget Campaign, *J. Atmos. Terr. Phys.*, 47, 195.

Rees, D. T.J. Fuller-Rowell, R. Gordon, M.F. Smith, N.C. Maynard, J.P. Heppner, N.W. Spencer, L. Wharton, P.B. Hays and T.L. Killeen (1986), A theoretical and empirical study of the response of the high-latitude thermosphere to the sense of the "Y" component of the interplanetary magnetic field, *Planet. Space Sci.*, 34, 1.

Rees, M.H., A.I. Stewart, W.E. Sharp, P.B. Hays, R.A. Hoffman, L.H. Brace, J.P. Doering and W.K. Peterson (1977), Coordinated rocket and satellite measurements of an auroral event : 1. Satellite observations and analysis, *J. Geophys. Res.*, 82, 2250.

Rees M.H. and R.G. Roble (1986), Excitation of $O(^1D)$ atoms in aurora and emission of the [OI] 6300Å line, (to be submitted).

Reiff, P.H. and J.L. Burch (1985), IMF B_y-dependent plasma flow and Birkeland currents in the dayside magnetosphere, 2. A global model for northward and southward IMF, *J. Geophys. Res.*, 90, 1595.

Richmond, A.D. and S. Matsushita (1975), Thermospheric response to a magnetic substorm, *J. Geophys. Res.*, 80, 2839.

Richmond, A.D. (1978), Gravity wave generation, propagation and dissipation in the thermosphere, *J. Geophys. Res.*, 83, 4131.

Richmond, A.D. (1979), Large-amplitude gravity wave energy production and dissipation in the thermosphere, *J. Geophys. Res.*, 84, 1880.

Rieger, E. (1974), Neutral air motions deduced from barium release experiments. 1. Vertical winds, , *J. Atmos. Terr. Phys.*, 36, 1377.

Rishbeth, H. (1972), Thermospheric winds and the F-region: A review, *J. Atmos. Terr. Phys.*, 34, 1.

Roble, R.G., P.B. Hays and A.F. Nagy (1968), Calculated [OI] 6300Å nightglow Doppler temperatures for solar cycle minimum, *Planet. Space Sci.*, 16, 1109.

Roble, R.G., B.A. Emery, J.E. Salah and P.B. Hays (1974), Diurnal variation of the neutral thermospheric winds determined from incoherent scatter radar data, *J. Geophys. Res.*, 79, 2868.

Roble, R.G., R.E. Dickinson and E.C. Ridley (1977), Seasonal and solar cycle variations of zonal mean ciculation in the thermosphere, *J. Geophys. Res.*, 82, 5493.

Roble, R.G., J.E. Salah and B.A. Emery (1977), The seasonalvariation of the diurnal thermosperic winds over Millstone Hill during solar cycle maximum, *J. Atmos. Terr. Phys.*, 39, 503.

Roble, R.G., R.E. Dickinson and E.C. Ridley (1982), Global circulation and temperature structure of the thermosphere with high-latitude plasma convection, *J. Geophys. Res.*, 87, 1599.

Roesler, F.L. (1968), Effects of plate defects in a polyetalon Fabry-Perot spectrometer, *Appl. Opt.*, 8, 829.

Roesler, F.L. (1974), Fabry-Perot instruments for astronomy, in 'Methods of Experimental Physics', N. Carleton (ed.), Academic Press.

Roesler, F.L. and J.E. Mack (1967), PEPSIOS purely interferometric high-resolution scanning spectrometer. IV. Performance of the PEPSIOS spectrometer, *J. Phys.*, 28, Suppl. 22, 313.

Rusch, D.W., J.C. Gerard and W.E. Sharp (1978), The reaction of $N(^2D)$ with O_2 as a source of $O(^1D)$ atoms in aurorae, *Geophys. Res. Lett.*, 5, 1043.

Russell, C.T. and R.L. McPherron (1973), Semiannual variation of geomagnetic activity, *J. Geophys. Res.*, 78, 92.

Sharp, W.E., M.H. Rees and A.I. Stewart (1979), Coordinated rocket and satellite observations of an auroral event : 2. Rocket observations and analysis, *J. Geophys. Res.*, 84, 1977.

Sharp W.E., D. Ortland and R. Cageao (1983), Concerning sources of $O(^1D)$ in aurora: electron impact and dissociative recombination, *J. Geophys. Res.*, 88, 3229.

Smith, L.B. (1968), An observation of strong thermospheric winds during a geomagnetic storm, *J. Geophys. Res.*, 73, 4959.

Spencer, N.W., R.F. Theis, L.E. Wharton and G.E. Carignan (1976), Local vertical motions and kinetic temperatures from AE-C as evidence for aurora-induced gravity waves, *Geophys. Res. Lett.*, 3, 313.

Spencer, N.W., L.E. Wharton, G.R. Carignan and J.C. Maurer (1981), The Dynamics Explorer wind and temperature spectrometer, *Space Sci. Instrum.*, 5, 417.

Spencer, N.W., L.E. Wharton, G.R. Carignan and J.C. Maurer (1982), Thermosphere zonal winds, vertical motions and temperature as measured fron Dynamics Explorer, *Geophys. Res. Lett.*, 9, 953.

Stoner, J.O. (1966), PEPSIOS purely interferometric high-resolution scanning spectrometer. III. Calculation of interferometer characteristics by means of optical transients, *J. Opt. Soc. Am.*, 56, 370.

Testud, J. (1970), Gravity waves generated during magnetic substorms, *J. Atmos. Terr. Phys.*, 32, 1793.

Torr, D.G., P.G Richards, M.R. Torr and V.J. Abreu (1981), Further quantification of the sources and sinks of thermospheric $O(^1D)$ atoms, *Planet. Space Sci.*, 29, 595.

Volland, H. (1974), A model of the magnetospheric electric convection field, *J. Geophys. Res.*, 83, 2695.

Wardill, P. and F. Jacka (1986), Vertical motions in the thermosphere over Mawson, Antarctica, *J. Atmos. Terr. Phys.*, 48, 289.

Wilksch, P.A. (1975), Measurements of thermospheric temperatures and winds using a Fabry-Perot spectrometer, Ph.D. Thesis, University of Adelaide, South Australia.

Wilksch, P.A. (1985), Instrument function of the Fabry-Perot spectrometer, *Appl. Opt.*, 24, 1502.

Addenda

The examiners of this thesis have identified a number of errors, omissions and points requiring further explanation. Minor corrections have been made in the text where possible. For the remaining items the following explanations are offered:

1. The conclusions relating to the horizontal wind field are based on averaged data. Professor McEwan makes the point that examples of raw data should be presented even if these data are not considered explicitly.

It should be noted that there are (at least) two levels of raw data. The most fundamental data object is the recorded profile $\{y_n\}$. The profiles from a given observing period are then averaged to yield estimates of wind velocity and temperature during that period. The wind and temperature measurements may also be regarded as 'raw data' for averaging purposes.

An example of a typical night's wind and temperature data is presented in Fig. 7.1. There is, however, no discussion of results on a night-by-night basis except for the 6 nights of vertical wind measurements presented in section 7.8. No examples of the recorded profiles $\{y_n\}$ are provided.

Professor McEwan's point is well taken and it is acknowledged that further discussion is required concerning the selection and rejection of recorded profiles. Specific criticisms are addressed in 2(a) through 2(c) below.

2.(a) The signal to noise ratio of the recorded profiles is calculated by the analysis procedure but is not used explicitly in the analysis. Emphasis is instead given to the statistical uncertainties in the derived parameters of the source profile; i.e. profile width, peak position and total counts. The corresponding uncertainties in the temperature and in the components of the wind velocity were typically within the ranges 40-60K and 10-25ms^{-1} respectively.

(b) For observations other than those described in section 7.5, signal integration continued until a total of ~50,000 counts was accumulated. This empirical figure was suggested by Wilksch (1975) who had found it to produce acceptable results at Mt Torrens. The discussion in section 8.2 describes how this figure should be reduced by a factor of two or more.

(c) The analysis routine calculates the χ^2 parameter which describes the goodness of fit of a Gaussian curve to the source profiles. Profiles with $\chi^2>5$ were rejected from the analysis. Such profiles represented less than 1% of the total. Typical values of χ^2 were in the range 0.5 to 2.5.

3. (a) The plate separation was changed several times within the course of the year. This was necessary for measurements of finesse and for maintenance reasons. All of the observations were made with the separation in the range 3.0-3.3mm. This is in accordance with the requirements of section 4.3.5.

(b) Reflective finesse was measured using the method described by Jacka (1984).

(c) The basis for assuming a temperature of 300K for the Hg^{198} source is described by Wilksch (1975) and references therein.

4. The large horizontal divergence described in section 7.6 has been ascribed to the effects of momentum deposition from dissipating gravity waves.

Professor McEwan has correctly pointed out that the apparent divergence may be removed by relaxing the assumption of a zero mean vertical wind (section 6.6). Indeed, the detection of large vertical winds during disturbed periods is described in section 7.5 and so this assumption must be questioned.

Unfortunately, the available data do not permit us to settle this question and we are obliged to make the most reasonable assumption under the circumstances. In order to remove the apparent divergence it would be necessary to assume a vertical wind of the order of $100ms^{-1}$ which must persist throughout the period of observation. It is difficult to understand how such a motion could be maintained.

It is certainly acknowledged that this matter warrants further investigation and this is discussed further in section 8.2.

Reference

Jacka, F. (1984), Application of Fabry-Perot spectrometers for measurement of upper atmospheric temperatures and winds, In : Vincent, R.A. (ed.), Handbook for MAP, 13, 19.